DISSERTATION

WAVE PROPAGATION:
LASER PROPAGATION AND QUANTUM TRANSPORT

Submitted by

Sophia Potoczak Bragdon

Department of Mathematics

In partial fulfillment of the requirements

For the Degree of Doctor of Philosophy

Colorado State University

Fort Collins, Colorado

Spring 2021

Doctoral Committee:

Advisor: Olivier Pinaud

Wolfgang Bangerth
Margaret Cheney
Martin Gelfand

ABSTRACT

WAVE PROPAGATION:
LASER PROPAGATION AND QUANTUM TRANSPORT

This dissertation consists of two independent projects, where wave propagation is the common theme. The first project considers modeling the propagation of laser light through the atmosphere using an approximation procedure we call the variational scaling law (VSL). We begin by introducing the Helmholtz equation and the paraxial approximation to the Helmholtz equation, which is the starting point of the VSL. The approximation method is derived by pairing the variational formulation of the paraxial Helmholtz equation with a generalized Gaussian ansatz which depends on the laser beam parameters. The VSL is a system of stochastic ODEs that describe the evolution of the Gaussian beam parameters. We will conclude with a numerical comparison between the variational scaling law and the paraxial Helmholtz equation. Through exploring numerical examples for increasing strengths of atmospheric turbulence, we show the VSL provides, at least, an order-one approximation to the paraxial Helmholtz equation.

The second project focuses on quantum transport by numerically studying the quantum Liouville equation (QLE) equipped with the BGK-collision operator. The collision operator is a relaxation-type operator which locally relaxes the solution towards a local quantum equilibrium. This equilibrium operator is nonlinear and is obtained by solving a moment problem under a local density constraint using the quantum entropy minimization principle introduced by Degond and Ringhofer in [1]. A Strang splitting scheme is defined for the QLE in which the collision and transport of particles is treated separately. It is proved that the numerical scheme is well-defined and convergent in-time. The splitting scheme for the QLE is applied in a numerical study of electron transport in different collision regimes by comparing the QLE with the ballistic Liouville equation and the quantum drift-diffusion model. The quantum drift-diffusion model is an example

of a quantum diffusion model which is derived from the QLE through a diffusive limit. Finally, it is numerically verified that the QLE converges to the solution to the quantum drift-diffusion equation in the long-time limit.

ACKNOWLEDGEMENTS

First, I would like to thank my parents and sisters for their constant support in my education. My mom and dad have been my biggest supporters and without them I would not have had the courage to pursue mathematics. My sisters have always believed in me and encouraged me, especially in the moments when the stress felt like it was too much to bear on my own. Thank you to my Nana for constantly being my cheerleader in life.

I would also like to thank the many teachers and professors that believed in me and encouraged me to pursue mathematics. Particularly, my high school math teacher, Eric Bruns, my undergraduate advisor, Dr. Darren Mason, and my masters advisor, Dr. Bob Franzosa.

I would like to thank my advisor, Dr. Olivier Pinaud, for introducing me to an interesting project and for all of the support you have offered me over the years. I would also like to thank my committee member, Dr. Wolfgang Bangerth, for your mentoring, advice, and welcoming me into your research group which helped me grow as a scientist. I want to also thank the rest of my committee for your thoughtful feedback and time. I also had the opportunity to participate in a summer research program with the Air Force Research Lab and I want to thank my mentors Dr. Jacob Grosek and Dr. Dan Cargill for introducing me to an exciting new research area.

In my time here at CSU, I had the privilege to form some amazing life-long friendships with my fellow graduate students. We have shared many, many great times together, despite the difficulties of graduate school. I want to extend my deepest gratitude to all my friends and, in particular, Adam Afandi, Rebecca Afandi, Derek Handwerk, and Catherine Read. Your friendships helped make the stress of graduate school manageable.

Finally, I want to thank my husband Dan Bragdon. His love and support kept me afloat during this process and I would not have succeeded without him.

FUNDING ACKNOWLEDGEMENTS: This research was supported by NSF CAREER Grant DMS-1452349, AFSOR Grant-16RDCOR347, and the AFRL-USRA summer scholar program.

DEDICATION

To my parents.

TABLE OF CONTENTS

LIST OF TABLES

LIST OF FIGURES

Chapter 1

Introduction

This dissertation is comprised of two independent projects that share a common theme of wave propagation. Waves can take on many different forms depending on the physical phenomena being studied. For example, acoustic waves, seismic waves, and water waves are all examples of mechanical waves. In this dissertation, we focus on a different variety of waves: quantum mechanical and electromagnetic waves. In quantum mechanics the well-known particle-wave duality takes advantage of the fact that, in the quantum setting, particles such as electrons exhibit wave-like behavior including interference and dispersion. A wavefunction is used to describe the quantum state of the particle and the dynamics are described by the Schrödinger equation. The wavefunctions that solve the Schrödinger equation are not necessarily localized, thus, to model a localized quantum particle Gaussian wave packets are used. A wave packet can the exhibit both dispersion and interference. On the other hand, electromagnetic radiation can be treated as a wave consisting of an electric field component and a magnetic field component, which is typically described by Maxwell's equations. Electromagnetic waves describe various types of radiation such as radio waves, microwaves, infrared, visible light, ultraviolet, X-rays, and Gamma rays. In many applications, such as, modeling laser radiation, which can be infrared or visible light, it suffices to describe the propagating wave with the electromagnetic wave equation and other related approximations.

The first portion of this dissertation is focused on laser radiation propagation in the atmosphere which is an example of an electromagnetic wave. This project introduces a new approximation method for laser beam propagation in the atmosphere, which we call the *variational scaling law* and it is presented in Chapter 2. We begin with a brief derivation of the paraxial Helmholtz equation which is commonly used to describe atmospheric propagation of a laser beam. Next, we review the derivation of the variational scaling law which is based on using a variational formulation of the paraxial Helmholtz equation paired with a paremeterzied Gaussian beam ansatz. Lastly, we show

through numerical examples that the solution to the variational scaling law well-approximates the solution to the paraxial Helmhotlz equation.

The second portion of this dissertation is focused on the quantum mechanics perspective of wave propagation. Particularly, we are interested in numerically studying the quantum transport of electrons described by the *quantum Liouville equation* with collisions. The model we are using for capturing the particle collisions relies on a relaxation-type operator and this operator is defined using a quantum entropy minimization principle. In Chapter 3, we review the theory of Degond and Ringhofer, specifically the entropy minimization principle, and its relation to the macroscopic transport models derived from the quantum Liouville equation [1]. In Chapter 4, we turn our attention to the definition of a Strang splitting scheme for the quantum Liouville equation. The numerical scheme is first presented in a semi-discrete form where time is discretized, but space is continuous. In this semi-discrete setting, we prove the numerical scheme is convergent in time. Lastly, in Chapter 5, the fully discrete scheme is presented and, as an application, we numerically study the effects of collision regimes on electron transport in semiconductors.

Chapter 2

Laser Propagation

The majority of the work in this chapter comes directly from the submitted paper [2] and the conference paper [3]. This work is joint with Dr. Jacob Grosek, Kirtland Air Force Research Lab-Directed Energy Directorate, and Dr. Dan Cargill, Lockheed Martin Corporation. The project originated from my summer internship with the Air Force Research Lab Summer Scholar Program which is funded by the Universities Space Research Association. This project also received funding from the U.S. Air Force Office of Scientific Research (AFOSR) Computational Mathematics program through project number 16RDCOR347.

2.1 Background and Introduction

Laser systems have a wide-range of applications from medical to atmospheric communication to high energy laser weapons and all of these applications require propagating the laser beam through some medium [4]. In this work, we are focusing on understanding the effects of propagating a laser through the turbulent atmosphere and the application we have in mind are high energy laser weapons. To have a successful laser weapon system one must be able to know with confidence that the laser beam will reach the target with sufficient power and small beam spot-size, and in order to ensure this, the effects of atmospheric turbulence must be understood. A laser beam propagating through the atmosphere is subjected to diffraction, scattering, absorption, and turbulence [4, 5]. Diffraction is present even as a laser beam propagates through a perfect vacuum and is the result of the natural tendency of light to spread out. Diffraction causes the energy of the beam to be spread out over a larger area, which limits how small of a spot-size a laser beam can be focused to. Scattering due to the atmosphere will also cause beam widening but beam wander can also be observed. A beam wandering off its original propagation path can cause a laser weapon to miss the target, which defeats the purpose of deploying a laser weapon. Absorption is caused when certain conditions of the atmosphere, such as water vapor content, lead to absorption of a

portion of the laser beams energy into the atmosphere. This phenomena can lead to heating of the atmosphere directly surrounding the laser beam and induce the nonlinear interaction of thermal blooming which leads to power loss and widening of the beam. Lastly, atmospheric turbulence caused by microscopic fluctuations in temperature is characterized by small stochastic fluctuations in the index of refraction. Despite the small-size of the fluctuations in the index of refraction, the effects on a laser beam interacting with this random media can be quite profound. In particular, the perturbations in the index of refraction directly lead to phase perturbations in the wave, which then induce perturbations in the amplitude [4, 6–9]. This phenomena is called scintillation which is the same effect that causes one to observe the "twinkling" of stars in the night sky. The interaction of the laser beam with turbulence can cause the beam to widen and beam wander that is random. In this work, we are focusing on the effects of diffraction combined with turbulence.

Laser beams are an example of an optical wave that represents nearly monochromatic, coherent, electromagnetic radiation that propagates as a beam. The monochromatic property is due to the presence of a very small range of wavelengths which results in laser light of a single color, while ordinary sources of light, say, from a light bulb, contain many different wavelengths which causes the light to appear white. The temporal coherence of the laser light leads to the monochromatic property. On the other hand, the spatial coherency of laser light is due to the waves of the light being in phase with each other and this allows the laser light to propagate as a beam with a preferred direction.

Understanding how all of these factors affect the propagation of a laser beam is a challenging problem. Many approaches exist for simulating this optical atmospheric propagation, each of which is associated with a specific set of assumptions that tries to balance computational cost with fidelity. One such approach is the so-called *waveoptics* simulations, where the atmosphere is modeled as a random media with a chosen probability distribution and the optical propagation is modeled by a stochastic PDE. The typical choice of PDE for the waveoptics approach is the stochastic paraxial Helmholtz equation [4]. This is derived from Maxwell's equations under the assumptions of small wavelength and a high degree of coherency in the optical wave, which make

this PDE a good choice for modeling laser light. The uncertainty due to the stochastic atmospheric turbulence is typically quantified through Monte-Carlo methods, where an ensemble of wave metrics are gathered and used to calculate statistics. This approach is high-fidelity which also carries a high computational cost.

At the other end of the modeling spectrum are scaling laws, a term referring to a set of formulas derived from analysis (asymptotic or numerical) of the stochastic PDEs used in the wave optics approach. The objective in deriving these formulas is to map atmospheric statistics directly to statistics on the wave metrics without necessarily having to simulate the propagation directly. For example, the Rytov method gives a closed form representation for the first-order correction of a zeroth-order solution in the limit of small perturbations of the propagation medium [4, 8, 10]. The first-order correction takes the form of an integral over both the zeroth-order solution and the index of refraction perturbations along the propagation path. In cases where the zeroth-order solutions can be expressed in closed form, e.g. plane waves, these integrals can be well-approximated to form a mapping of atmospheric statistics to wave metrics. However, these formulations are always dependent on assumptions that limit the regime over which the resulting scaling laws are valid. For example, in the Rytov method, it is required that the atmospheric turbulence is weak or that the fluctuations in the index of refraction remain small. Despite the modeling limitations, these scaling law methods are commonly used to deliver first-order performance assessments of system design and deployment concepts in laser weapon systems [11–15].

This project introduces a new scaling law type approximation to the atmospheric propagation of laser (optical) beams based on a variational reformulation of the scalar stochastic paraxial Helmholtz equation that is commonly used in waveoptics simulations. We call this method the *Variational Scaling Law*. Working with the variational formulation allows approximations to be made through the use of suitably chosen trial functions, an approach that is commonly described as an extension of the Rayleigh-Ritz optimization procedure [16].We begin by outlining the derivation of the paraxial Helmholtz equation from the wave equation in Section 2.2.1. Next, we review vacuum propagation of a Gaussian beam in Section 2.2.2, which is used as the inspiration for our

choice of a generalized Gaussian trail solution. In Section 2.3, we review the variational formulation of the paraxial Helmholtz equation and the subsequent derivation of the Variational Scaling Law. Finally, in Section 2.4 we present a numerical comparison between waveoptics simulations and the variational scaling law.

2.2 Wave Equation and Paraxial Approximation

A propagating optical wave is described by Maxwell's equations. Since air (the atmosphere) has virtually no magnetic susceptibility, one can capture the traveling wave by only tracking the electric field of the light. After a few manipulations of Maxwell's equations, one arrives at a modified wave equation for the electric field:

$$\boldsymbol{\Delta}\mathbf{E} - \nabla\left(\nabla\cdot\mathbf{E}\right) - \frac{1}{c^2}\frac{\partial^2\mathbf{E}}{\partial t^2} = \mu_0\frac{\partial^2\mathbf{P}}{\partial t^2}, \tag{2.1}$$

where $\mathbf{E}$ is the electric field associated with angular frequency (ω) of the propagating wave, c is the speed of causality, and μ_0 represents the vacuum magnetic permeability. All interactions between the light and its medium (air) are captured by the electric polarization term $\mathbf{P} = \mathbf{P}(\mathbf{E})$. The relevant interactions for atmospheric propagation through turbulence includes only the real-valued background mean index of refraction of the air (n_0), a stochastic perturbation to this refractive index (δn_{turb}), and a constant linear loss caused by absorption and/or scattering in the atmosphere (α_{loss}). Loss is usually treated as a negative gain in the medium, and is derived as an imaginary perturbation to the refractive index [17]. Mathematically, the electric polarization can be expressed as, [18]:

$$\begin{aligned}
\mathbf{P}(\mathbf{E}) &\approx \mathbf{P}_{\text{background}}(\mathbf{E}) + \mathbf{P}_{\text{turb}}(\mathbf{E}) + \mathbf{P}_{\text{loss}}(\mathbf{E})\,,\\
\mathbf{P}_{\text{background}}(\mathbf{E}) &\approx \varepsilon_0\Big(\left[n_0^2 - 1\right]\mathbf{E}\Big),\\
\mathbf{P}_{\text{turb}}(\mathbf{E}) &\approx \varepsilon_0(2n_0\delta n_{\text{turb}} + \delta n_{\text{turb}}^2)\mathbf{E}\\
\mathbf{P}_{\text{loss}}(\mathbf{E}) &\approx \frac{i\alpha_{\text{loss}}\varepsilon_0 c n_0}{\omega}\mathbf{E}.
\end{aligned}$$

The vacuum electric permittivity is denoted as ε_0, and $\varepsilon_0\mu_0 = c^{-2}$. In this model, the light propagates in +z-direction, $\mathbf{E} = \mathbf{E}(\mathbf{r}, t)$, $\mathbf{r} = (x, y, z)$, and $\mathbf{E} = [E_x\ E_y\ E_z]^{\mathrm{T}}$.

We assume that the light wavefront can be propagated to its endpoint (target) in virtually static turbulence, since the turbulence changes over a much larger time scale than the travel time scale. As a consequence, we treat the index of refraction independent of time. With the electric polarization model and treating the turbulence as static yields the following model for the index of refraction

$$n(\mathbf{r}) = n_0 + \delta n_{\text{turb}}(\mathbf{r}).$$

We assume δn_{turb} is described by a random process that is stationary and isotropic in the transverse plane and satisfies a white-noise assumption in the propagation direction [4]. For the purposes of the numerical simulations presented in Section 2.4, we assume that in the transverse plane δn_{turb} is describe by the Kolmogorov statistical model for the atmosphere. The details of the statistical model used in the numerical simulations are given in Section 2.4.1. Note that other statistical models can be used in the transverse plane, provided they satisfy the stationary and isotropic assumption.

Neglecting the small perturbation to the index of refraction, δn_{turb}, the propagation medium is nearly homogeneous, which means Gauss's Law is applicable to this problem, [4, 18]:

$$\nabla \cdot \mathbf{E} \approx 0.$$

Using the above polarization model and Gauss's Law, the modified wave equation (2.1) reduces to the following:

$$\Delta\mathbf{E} - \mu_0\varepsilon_0(n_0 + \delta n_{\text{turb}})^2\frac{\partial^2\mathbf{E}}{\partial t^2} + \frac{i\alpha_{\text{loss}}\varepsilon_0\mu_0}{\omega}\frac{\partial^2\mathbf{E}}{\partial t^2} = 0. \tag{2.2}$$

In the next section we discuss the paraxial approximation to the wave equation, which is a common approximation made for waves propagating with a preferred direction and is the starting point for the derivation of the variational scaling law.

2.2.1 Paraxial Helmholtz Equation

The paraxial approximation to the wave equation utilizes physical properties of the laser light to simplify the governing equation. In particular, if we call the z-axis the optical axis, then the paraxial approximation implies that the light propagating maintains a small angle with the optical axis. Since the propagating light is assumed to be from a laser source, we can assume that it is highly coherent and propagates with a preferred direction. Here, we take the $+z$-direction to the propagation direction, which makes the x, y- directions transverse and is denoted by the symbol $\perp$. Temporal coherence indicates that the light is near-monochromatic; other than the optical oscillation at the frequency ω, the only other two relevant timescales are that of the light travel time from the laser source to the target and that of the turbulence. Furthermore, it is assumed that the laser light is robustly linearly polarized in the x-direction, meaning E_y and E_z are negligibly small when compared to E_x. Thanks to the temporal coherence of the electric field, the component E_x can be approximated as

$$E_x(t, x, y, z) = 2\,\mathrm{Re}\big\{A(x, y, z)e^{-i\omega t}\big\}$$

where $A(x, y, z)$ is the complex amplitude. This substitution yields the *stochastic Helmholtz equation*:

$$\Delta A + k_0^2(n + \delta n_{\text{turb}})^2 A + \frac{i\alpha_{\text{loss}} k_0^2}{\omega} A = 0. \tag{2.3}$$

Above, we take $k_0 = \frac{\omega}{c}$. The Helmholtz equation, which is time independent, is commonly used to model the propagation of laser light because we assume the timescale of the propagating wave is much faster than the other relevant time scales and we treat the laser light as reaching the target instantaneously.

We now will scale (nondimensionalize) the Helmholtz equation and in the process, we recover the proper scalings for the paraxial and white noise approximation regimes [19, 20]. We proceed

by assuming the amplitude, A, satisfies the following slowly varying envelope ansatz

$$A(x, y, z) = U(x, y, z)e^{ikz}, \tag{2.4}$$

where $k = n_0 k_0 = n_0\omega/c$ is the wave number. This ansatz is substituted into the Helmholtz equation (2.3) to obtain

$$-k_0^2 n_0^2 U + 2ik_0 n_0 \frac{\partial U}{\partial z} + \frac{\partial^2 U}{\partial z^2} + \Delta_\perp U + k_0^2(n_0 + \delta n_{\text{turb}})^2 U + \frac{i\alpha_{\text{loss}} k_0^2}{\omega} U = 0, \tag{2.5}$$

where $\Delta_\perp = \partial_x^2 + \partial_y^2$ is the transverse Laplacian operator, and $k_0 = \omega/c$.

When (2.5) is paired with the proper scaling of the dimensional constants it yields the paraxial approximation of the PDE. When modeling laser propagation in the atmosphere, it is common to also make the white noise approximation, which assumes δn_{turb} can be approximated by white noise in the z-variable [4]. Meaning, we can interpret δn_{turb} as δ-correlated in the z variable and this is also called the Markov approximation. We will use the Kolmogorov model in the transverse plane for the atmospheric statistics and this is presented in Section 2.4.1. For the formulation of the variational scaling law we will simultaneously utilize both the paraxial and white noise approximations. The proof of convergence of the wave equation to the solution of the white noise paraxial Helmholtz equation in stratified weakly fluctuating media can be found in [19]. The regime studied in [19] is called the high frequency weak fluctuation regime and it has been studied heavily, for example see [18, 20–23].

Next, we nondimensionalize (2.5) and through the particular scaling choice we will obtain the paraxial Helmholtz equation. First consider putting a "hat" $[\hat{\cdot}]$ over each parameter/variable in (2.5) in order to indicate that it has a dimension/unit. Next, make the following transformations: $\hat{x} = \widehat{l_0}x$, $\hat{y} = \widehat{l_0}y$, $\hat{z} = \widehat{L_0}z$, $\widehat{U} = \widehat{U_0}u$, $\widehat{\delta n_{\text{turb}}} = \sigma\delta n_{\text{turb}}$, $\varepsilon = \widehat{l_0}/\widehat{L_0}$, $\xi = \widehat{l_0}^2\widehat{k_0}/\widehat{L_0}$, $\gamma = \widehat{l_0}\widehat{k_0}\sigma$, $\nu = \widehat{l_0}\widehat{k_0}\sigma^2$, and $\zeta = \widehat{l_0}^2\widehat{k_0}\widehat{\alpha_{\text{loss}}}$, where the unitless parameters/variables do not have "hats" over them. Note that σ represents the strength of the atmospheric turbulence, and the stochastic perturbation to the refractive index ($\widehat{\delta n_{\text{turb}}}$) is actually unitless, but still uses a "hat" in order to distinguish it from its

rescaling by σ. Substituting this scaling into (2.5) yields

$$2i\xi n_0 \frac{\partial u}{\partial z} + \varepsilon^2 \frac{\partial^2 u}{\partial z^2} + \Delta_\perp u + 2\gamma^2 n_0 \delta n_{\text{turb}} u + \nu^2 \delta n_{\text{turb}}^2 u + i n_0 \zeta u = 0. \tag{2.6}$$

Where we assume $0 < \widehat{l_0} \ll \widehat{L_0}$ and we take the length scales to be given by the inner and outer scales of the atmospheric turbulence.

Typically the wavelength of laser light is chosen so that it transmits well through the atmosphere with low loss. The value of α_{loss} can be estimated using measured transmissions through the atmosphere [24]. Since the loss is a linear effect that occurs over the distance traveled, it has negligible transverse effects on the traveling wave and its phase, unlike the turbulence. This means it is reasonable to treat the loss separately from the turbulence in modeling atmospheric propagation of a laser beam. This can be accomplished by breaking (2.6) into two equations as follows:

$$2i\xi n_0 \frac{\partial u}{\partial z} = -i n_0 \zeta u \tag{2.7}$$

$$2i\xi n_0 \frac{\partial u}{\partial z} = -\varepsilon^2 \frac{\partial^2 u}{\partial z^2} - \Delta_\perp u - 2\gamma^2 n_0 \delta n_{\text{turb}} u \tag{2.8}$$

The characteristic values for the dimensional constants in the scaling are in Table 2.1 and the corresponding characteristic values for the nondimensional constants ε, ξ, γ, and ν are in Table 2.2. Based off of the characteristic values for the constants in 2.2, we see that $\varepsilon^2, \nu^2 \ll 1$ and $\xi \approx \gamma$ is the dominant scaling. With this observation, we can neglect the terms $\varepsilon^2 \frac{\partial^2 u}{\partial z^2}$ and $\nu^2 \delta n_{\text{turb}}^2 u$ in (2.6), which yields the nondimensional paraxial Helmholtz equation paired with the loss equation,

$$\frac{\partial u}{\partial z} = -\frac{\alpha}{2} u \tag{2.9}$$

$$\frac{\partial u}{\partial z} = \frac{i}{2n_0 \xi} \Delta_\perp u + \frac{i\gamma^2}{\xi} \delta n_{\text{turb}} u. \tag{2.10}$$

Above $\alpha = \zeta/\xi = \widehat{L_0}\widehat{\alpha_{\text{loss}}}$. The particular scaling we used to obtain (2.10) coincides with the scaling in [19, 20] for the high frequency white noise regime.

Table 2.1: Characteristic values for the dimensional constants in the paraxial scaling.

Physical Constant	Symbol	Characteristic Value
Kolmogorov Inner Scale	$\widehat{l_0}$	$10^{-3} - 10^{-2}$ m, [4]
Kolmogorov Outer Scale	$\widehat{L_0}$	$10 - 10^{3}$ m, [4]
Index Variance	σ^2	$10^{-18} - 10^{-10}$, [4]
Wavelength	$\widehat{\lambda}$	1×10^{-6} m
Wavenumber	$\widehat{k_0}$	$2\pi \times 10^{6}$ m^{-1}
Propagation Distance	$\widehat{L}$	$10^{2} - 10^{4}$ m, [20]
Aperture Diameter	$\widehat{D}$	$10^{-2} - 1$ m
atmospheric loss	$\widehat{\alpha_{\text{loss}}}$	$10^{-5} - 10^{-3}$ m^{-1} [24, 25]

Note that the loss equation, (2.9), can be solved analytically given initial condition $u(x, y, 0) = u_0\phi(x, y)$, where $u_0 \in \mathbb{C}$ and $\phi(x, y)$ is the initial, real-valued transverse profile of the propagating wave front. This yields $u(x, y, z) = u_0\phi(x, y)e^{-\alpha z/2}$. On the other hand, the stochastic paraxial Helmholtz equation (2.10) conserves the power in the wavefront as the light propagates. For the initial condition $|u_0|^2$ is related to the power within the beam and this quantity is conserved under (2.10). The exponential factor in the loss equation solution, $e^{-\alpha z}$, attenuates the power as the light propagates. Since the loss-less paraxial Helmholtz equation (2.10) conserves power, if we attenuate the solution by the exponential factor, we capture the effect of atmospheric loss. The variational scaling law focuses approximating the stochastic paraxial Helmholtz equation without loss. For the remainder of this chapter we will focus on the approximation to (2.10), and, if desired, loss can be included in the model using the procedure described above.

The paraxial Helmholtz equation, (2.10), is the starting point for variational scaling law, which is the topic of the next chapter. However, before developing the variational scaling law, we review the derivation of a focusing Gaussian beam in vacuum propagation. The focusing Gaussian beam solution provides inspiration for the Gaussian beam ansatz introduced in Section 2.3.2.

2.2.2 Vacuum Gaussian Beam

Although, the variational scaling law is an approximation method for the *stochastic* paraxial Helmholtz equation, we gain insight into the generalized Gaussian ansatz used in the derivation of

Table 2.2: Characteristic values for the nondimensional constants in the paraxial scaling.

Symbol	Value	Characteristic Value
ε	$\widehat{l_0}/\widehat{L_0}$	$10^{-6} - 10^{-4}$
ξ	$\widehat{l_0}^2\widehat{k_0}/\widehat{L_0}$	$10^{-3} - 10$
γ	$\widehat{l_0}\widehat{k_0}\sqrt{\sigma}$	$10^{-1.5} - 1$
ν	$\sigma\gamma$	$10^{-12} - 10^{-5}$
ζ	$\widehat{l_0}^2\widehat{k_0}\widehat{\alpha_{\text{loss}}}$	$10^{-5} - 10^{-1}$

the LSL by considering the deterministic Gaussian beam. In this section we set $\delta n_{\text{turb}} = 0$ in the paraxial Helmholtz equation and seek exact solutions in the form of a Gaussian. The form of the exact Gaussian beam solution inspires the choice of the generalized Gaussian ansatz used in the LSL derivation. The basic Gaussian beam model is useful because it allows for the incorporation of focusing/diverging characteristics of the beam. Other simplified laser beam models include the plane wave and spherical wave models but these models are unable to capture any focusing characteristics which is an important property to understand in the application of laser weapons, for example. The focusing properties of the Gaussian beam solution will help us choose initial conditions with focusing for the LSL, this will be discussed later in Section 2.4. We are following the derivation of the vacuum Gaussian beam presented in [4].

We begin with the unperturbed (free) paraxial Helmholtz equation,

$$2n_0 i\xi\frac{\partial u}{\partial z} + \Delta_\perp u = 0, \tag{2.11}$$

and seek solutions of the form

$$u(\mathbf{r}, z) = \exp\left(-i\left(\frac{n_0\xi r^2}{2q(z)} + p(z)\right)\right), \tag{2.12}$$

where $r = \sqrt{x^2 + y^2}$, and $q(z)$ and $p(z)$ are to be found. We readily find by substituting (2.12) into (2.11) that p and q must satisfy the equations

$$\begin{aligned} q(z) &= iq_0 - (z - z_w), \quad q(z_w) = iq_0,\ q_0 \in \mathbb{R}, \\ p(z) &= -i \ln\left(1 + i\left(\frac{z - z_w}{q_0}\right)\right), \end{aligned}$$

where z_w is some position along the propagation length. To obtain our final Gaussian beam solution, we make the following simplifications:

$$\exp(-ip(z)) = \frac{1}{1 + i(\frac{z-z_w}{q_0})} = \left(1 + \left(\frac{z - z_w}{q_0}\right)^2\right)^{-\frac{1}{2}} \exp\left(-i \arctan\left(\frac{z - z_w}{q_0}\right)\right),$$

and

$$\begin{aligned} \exp\left(\frac{-in_0\xi r^2}{2q(z)}\right) &= \exp\left(\frac{-in_0\xi r^2(z - z_w + iq_0)}{2((z - z_w)^2 + q_0^2)}\right) \\ &= \exp\left(\frac{in_0\xi r^2}{2(z - z_w)(1 + (\frac{q_0}{z-z_w})^2)}\right) \exp\left(-\left(\frac{n_0\xi r^2}{2q_0(1 + (\frac{z-z_w}{q_0})^2)}\right)\right) \end{aligned}$$

Next we substitute the above relationships for $\exp(-ip(z))$ and $\exp\left(\frac{-in_0\xi r^2}{2q(z)}\right)$ into the Gaussian beam ansatz (2.12), set $\sqrt{q_0} = w_0$, and normalize, we find,

$$u(\mathbf{r}, z) = \sqrt{\frac{1}{\pi}} W(z) \exp\left(-W^2(z)|\mathbf{r}|^2 - i\left(F(z)|\mathbf{r}|^2 + P(z)\right)\right) \tag{2.13}$$

The functions $W(z)$ and $F(z)$ are given by

$$W(z) = \sqrt{n_0\xi} \frac{w_0}{\sqrt{w_0^4 + (z - z_w)^2}}, \tag{2.14}$$

$$F(z) = \frac{-n_0\xi}{2} \frac{z - z_w}{(z - z_w)^2 + w_0^4} \tag{2.15}$$

$$P(z) = \arctan\left(\frac{z - z_w}{w_0^2}\right) \tag{2.16}$$

The function $W(z)$ represents the beam width or spot size, note that the physical width of the beam is the given by $1/W(z)$. The function $F(z)$ describes the focusing/diverging of the beam and it is related to the reciprocal of the radius of curvature. The value $\arctan((z - z_w)/w_0^2)$ is called the piston phase. The value w_0 is the beam waist (the smallest spot size) which occurs at $z = z_w$. Note that at the location of the beam waist, we have $W(z_w) = \frac{1}{w_0}$ and $F(z_w) = 0$. Clearly, the beam is the smallest when $F(z) = 0$, on the other hand, it is convergent when $F(z) < 0$ and it is divergent when $F(z) > 0$. The function $P(z)$ in (2.16) corresponds to the piston phase which can be thought of as the mean value of the phase over the wave front.

From the Gaussian beam calculations we can identify some important physical properties we would like to model with the variational scaling law set-up. Clearly our generalized Gaussian ansatz should include a term to account for the piston phase and because we account for focusing we must also have a term to account for the beam spot size changing. Focusing/defocusing is just one example of an optical aberration that can be observed in a laser propagating in the atmosphere. Another common optical aberration observed in laser systems is tilt of beam within the transverse plane. In the next chapter, we formulate the variational scaling law utilizing the variational formulation paired with a generalized Gaussian ansatz that accounts for various physical beam characteristics.

In this section, we introduced the modeling assumptions that lead to the paraxial Helmholtz equation in the white-noise regime from the scalar wave equation. The section concluded with a presentation of the homogeneous Gaussian beam solution. In the next section, we develop the variational scaling law and utilize the homogeneous Gaussian beam solution as inspiration for the parameterized Gaussian ansatz that is key to the derivation of the variational scaling law.

2.3 Derivation of Variational Scaling Law

In this section, we develop the variational scaling law as an approximation method for the paraxial Helmholtz equation (2.10). The derivation requires the development of a variational formulation of the paraxial Helmholtz equation and we reduce the system with a parameterized ansatz

inspired by the Gaussian beam solution. The theoretical framework for the variational scaling law is inspired by D. Anderson's work in [26–29], where Anderson uses a so-called "variational approximation" to simplify the partial differential equation system into a lower-dimensional system. The approximation arises from defining a parameterized ansatz for the solution to the PDE and using the Euler-Lagrange equations to obtain a lower dimensional system on the ansatz parameters, as was done in [26] for the nonlinear Schrödinger equation. This variational approximation method can be used on the homogeneous paraxial Helmholtz equation along the Gaussian beam ansatz and through this we can recover the Gaussian beam relationships presented in Section 2.2.2. In our case, the variational approximation relies on Hamilton's principle, and ultimately needs the governing dynamical system to have a conserved quantity, which is why we work with the lossless paraxial Helmholtz equation (2.10) because it conserves power. Recall, that if one wants to incorporate atmospheric loss into the model the obtained approximate solution to the paraxial Helmholtz equation can be attenuated according to the solution to the loss equation (2.9).

In order to derive a lower-dimensional model for the paraxial Helmholtz equation, we must first specify the variational formulation of the PDE, second define the generalized Gaussian beam ansatz, and lastly, derive a set of governing equations using the Euler-Lagrange equation paired with the particular ansatz choice.

2.3.1 Variational Formulation of Paraxial Helmholtz Equation

To begin, we recast the paraxial Helmholtz equation as a functional defined in terms of the Lagrangian density for the system,

$$\mathcal{J}(u, \nabla u) = \int_0^L \int \int \mathcal{L}_D(u, \nabla u) dx dy dz, \tag{2.17}$$

where $\mathcal{L}_D$ is the Lagrangian density. For the lossless paraxial stochastic Helmholtz equation it is given by

$$\mathcal{L}_{\mathrm{D}}\left(u, \nabla u\right) = -2in\xi \,\mathrm{Im}\left(\bar{u}\frac{\partial u}{\partial z}\right) - \left|\nabla_{\perp} u\right|^2 + 2n\gamma^2 \delta n_{\text{turb}} |u|^2. \tag{2.18}$$

Using the definition of the Gâteaux derivative, we can show that the critical points of the functional (2.17) are also solutions to the paraxial Helmholtz equation. Calculating the critical points of (2.17) yields the corresponding Euler-Lagrange equation:

$$\frac{\partial \mathcal{L}_D}{\partial u} - \sum_{i=1}^{3} \frac{\partial}{\partial r_i} \left(\frac{\partial \mathcal{L}_D}{\partial(\partial_{r_i}(u))} \right) = 0, \tag{2.19}$$

where $r_i \in \{x, y, z\}$ for $i = 1, 2, 3$, respectively. The paraxial Helmholtz equation can be recovered from the variational formulation by substituting the Lagrangian density (2.18) into the Euler-Lagrange equation (2.19), as desired. Next it is necessary to define the generalized Gaussian ansatz in order to obtain the lower-dimensional governing system for laser propagation in weak turbulence.

2.3.2 Generalized Gaussian Ansatz

Next we define a parameterized Gaussian ansatz that will enable us to reduce the PDE to a lower-dimensional system via the variational formulation. The key idea behind the ansatz is to assume the initial condition is Gaussian and the wave front remains approximately Gaussian with varying beam parameters throughout propagation. The beam parameters must depend on the propagation direction since we want to allow them to evolve over the propagation path. Thus, we propose a solution ansatz that is a Gaussian with the beam characteristics parameterized by z. This idea will effectively define the solution's dependence on a subset of the independent variables (x and y) and as a result parameterize the solution's dependence in the remaining variable, z.

In the spirit of the homogeneous Gaussian beam solution presented in the previous section, we define a generalized Gaussian beam ansatz with beam parameters representing the width of the beam, focusing of the beam, among additional possible phase abberations. We assume the solution is well represented in the transverse direction (with respect to propagation), i.e. the variables x and y, by a Gaussian profile

$$u\big(\mathbf{r}_\perp, \mathbf{p}(z)\big) = I\big(\mathbf{p}(z)\big) e^{-\left(\Theta\left(\mathbf{r}_\perp, \mathbf{p}(z)\right) + i\Phi\left(\mathbf{r}_\perp, \mathbf{p}(z)\right)\right)}, \tag{2.20}$$

where $\mathbf{p}(z) = \big[C(z),\ W_x(z),\ W_y(z),\ T_x(z),\ T_y(z),\ X(z),\ Y(z), F_x(z),\ F_y(z),\ P(z)\big]^{\mathrm{T}}$ and

$$
\begin{aligned}
I\big(\mathbf{p}(z)\big) &= \frac{C(z)\sqrt{W_x(z)W_y(z)}}{\sqrt{\pi}}, \\
\Theta\big(\mathbf{r}_\perp, \mathbf{p}(z)\big) &= \frac{1}{2}\left(W_x^2(z)\big(x - X(z)\big)^2 + W_y^2(z)\big(y - Y(z)\big)^2\right), \\
\Phi\big(\mathbf{r}_\perp, \mathbf{p}(z)\big) &= P(z) + T_x(z)\big(x - X(z)\big) + T_y(z)\big(y - Y(z)\big) + \\
&\qquad F_x(z)\big(x - X(z)\big)^2 + F_y(z)\big(y - Y(z)\big)^2.
\end{aligned}
$$

In (2.20) the dependence in the transverse plane is completely determined while the dependence in the propagation direction z lies in the set of real valued parameters, $\mathbf{p}(z)$, which represent the physical properties of the beam. For example, $I\left(\mathbf{p}(z)\right)$ represents the peak of the beam amplitude and depends on the parameters $W_x(z)$, $W_y(z)$ representing the beam width in the x and y directions, respectively, and the parameter $C(z)$, associated with the total beam energy/power, i.e. $\iint_{\mathbb{R}^2} |u\big(\mathbf{r}_\perp, \mathbf{p}(z)\big)|^2\, dxdy = C^2(z)$. Likewise, $\Theta\big(\mathbf{r}_\perp, \mathbf{p}(z)\big)$ controls the beam profile through the width parameters previous discussed and parameters $X(z)$, $Y(z)$ representing the (transverse) profile center. Finally, $\Phi\big(\mathbf{r}_\perp, \mathbf{p}(z)\big)$ is the beam phase term, dependent on parameters for the piston $P(z)$, tip/tilt $T_x(z)$, $T_y(z)$ and focusing $F_x(z)$, $F_y(z)$.

Because the ansatz is explicitly defined in transverse plane, the evolution of the system is now determined through the evolution parameters of the ansatz in the propagation direction. If additional parameters are added to the ansatz we could capture more of the dynamics of the true solution, but at the cost of increasing the degrees of freedom and complexity of the reduced system. As a result, the parameters included in the ansatz are carefully chosen to reflect specific quantities of interest and also matched according to knowledge of how those dynamics of the parameters are related. For example, we add parameters to account for tilt in the phase, i.e. $T_x(z)$, $T_y(z)$, which means the corresponding parameters, i.e. $X(z)$, $Y(z)$, should be included to capture shifts in the beam center transverse to propagation.

With the Gaussian ansatz as defined, we turn to defining the governing system of stochastic differential equations for the parameters of the ansatz. We do this by defining a reduced functional

by integrating out the x and y dependence in (2.17) and we obtain the system of differential equations using the Euler-Lagrange equation for the reduced Lagrange density. This process is detailed in the next section.

2.3.3 Derivation of Governing Equations

We begin by substituting the Gaussian ansatz (2.20) into the Lagrangian density (2.18) and integrate with respect to x and y to obtain the reduced Lagrangian density

$$\mathcal{F}_{\mathrm{D}}\left(\mathbf{p}, \frac{d\mathbf{p}}{dz}\right) = \int_{-\infty}^{\infty}\int_{-\infty}^{\infty} \mathcal{L}_{\mathrm{D}}\left(u(\mathbf{r}_{\perp}, \mathbf{p}(z)), \nabla u(\mathbf{r}_{\perp}, \mathbf{p}(z))\right)\, dxdy.$$

In particular, the reduced Lagrangian density takes on the form

$$\begin{aligned}\mathcal{F}_{\mathrm{D}}\left(\mathbf{p}, \frac{d\mathbf{p}}{dz}\right) = 2n\xi C^2 \left(\frac{dP}{dz} + \frac{\frac{dF_x}{dz}}{2W_x^2} + \frac{\frac{dF_y}{dz}}{2W_y^2}\right) - C^2\left(\frac{dX}{dz}T_x + \frac{dY}{dz}T_y\right) - \frac{C^2}{2}\left(W_x^2 + W_y^2\right) \\ - C^2\left(T_x^2 + T_y^2\right) - 2C^2\left(\frac{F_x^2}{W_x^2} + \frac{F_y^2}{W_y^2}\right) + 2n\gamma^2\left\langle \delta n_{\text{turb}}, I^2 e^{-2\Theta}\right\rangle,\end{aligned} \tag{2.21}$$

above $\langle\cdot,\cdot\rangle$ denotes the $L^2(\mathbb{R}^2)$-inner product. We then integrate (2.21) with respect to z to obtain the reduced functional,

$$J\left(\mathbf{p}, \frac{d\mathbf{p}}{dz}\right) = \int_0^L \mathcal{F}_{\mathrm{D}}\left(\mathbf{p}, \frac{d\mathbf{p}}{dz}\right)\, dz. \tag{2.22}$$

Now that we have the proper variational formulation for our Gaussian ansatz, we can use the Euler-Lagrange equations to equivalently describe the dynamics of the system. For the reduced system, the Euler-Lagrange equations are given by

$$\frac{\partial \mathcal{F}_{\mathrm{D}}}{\partial p_j} - \frac{d}{dz}\frac{\partial \mathcal{F}_{\mathrm{D}}}{\partial\left[\frac{dp_j}{dz}\right]} = 0 \tag{2.23}$$

for

$$p_j \in \left\{ \underbrace{C}_{j=1} \underbrace{W_x}_{j=2} \underbrace{W_y}_{j=3} \underbrace{T_x}_{j=4} \underbrace{T_y}_{j=5} \underbrace{X}_{j=6} \underbrace{Y}_{j=7} \underbrace{F_x}_{j=8} \underbrace{F_y}_{j=9} \underbrace{P}_{j=10} \right\}.$$

Finally, we can obtain the governing system of differential equations by evaluating the Euler-Lagrange equation for each $j = 1, \ldots, 10$ with the definition of the reduced Lagrangian density (2.21). This process yields:

$$C(z) = C(0), \tag{2.24}$$

$$\frac{dW_x}{dz}(z) = \frac{2}{n\xi} F_x(z) W_x(z), \tag{25a}$$

$$\frac{dW_y}{dz}(z) = \frac{2}{n\xi} F_y(z) W_y(z), \tag{25b}$$

$$\frac{dT_x}{dz}(z) = -n\gamma^2 \left\langle \delta n_{\text{turb}}(\mathbf{r}), M_{T_x}(\mathbf{r}) \right\rangle, \tag{25c}$$

$$\frac{dT_y}{dz}(z) = -n\gamma^2 \left\langle \delta n_{\text{turb}}(\mathbf{r}), M_{T_y}(\mathbf{r}) \right\rangle, \tag{25d}$$

$$\frac{dX}{dz}(z) = -2T_x(z), \tag{25e}$$

$$\frac{dY}{dz}(z) = -2T_y(z), \tag{25f}$$

$$\frac{dF_x}{dz}(z) = -\frac{W_x^4(z)}{2n\xi} + \frac{2F_x^2(z)}{n\xi} + \frac{\gamma^2}{\xi} \left\langle \delta n_{\text{turb}}(\mathbf{r}), M_{F_x}(\mathbf{r}) \right\rangle, \tag{25g}$$

$$\frac{dF_y}{dz}(z) = -\frac{W_y^4(z)}{2n\xi} + \frac{2F_y^2(z)}{n\xi} + \frac{\gamma^2}{\xi} \left\langle \delta n_{\text{turb}}(\mathbf{r}), M_{F_y}(\mathbf{r}) \right\rangle, \tag{25h}$$

$$\frac{dP}{dz}(z) = \frac{\left(W_x^2(z) + W_y^2(z)\right)}{2n\xi} - \frac{\gamma^2}{\xi} \left\langle \delta n_{\text{turb}}(\mathbf{r}), M_P(\mathbf{r}) \right\rangle, \tag{25i}$$

where

$$
\begin{aligned}
M_{T_x}(\mathbf{r}) &:= \frac{2}{C^2(z)} \frac{\partial \left| u\big(\mathbf{r}_\perp, \mathbf{p}(z)\big) \right|^2}{\partial X} = 4W_x^2 \left(x - X\right) \frac{|u|^2}{C^2}, \\
M_{T_y}(\mathbf{r}) &:= \frac{2}{C^2(z)} \frac{\partial \left| u\big(\mathbf{r}_\perp, \mathbf{p}(z)\big) \right|^2}{\partial Y} = 4W_y^2 \left(y - Y\right) \frac{|u|^2}{C^2}, \\
M_{F_x}(\mathbf{r}) &:= \frac{W_x^3(z)}{C^2(z)} \frac{\partial \left| u\big(\mathbf{r}_\perp, \mathbf{p}(z)\big) \right|^2}{\partial W_x} = W_x^2 \left[1 - 2W_x^2 \left(x - X\right)^2\right] \frac{|u|^2}{C^2}, \\
M_{F_y}(\mathbf{r}) &:= \frac{W_y^3(z)}{C^2(z)} \frac{\partial \left| u\big(\mathbf{r}_\perp, \mathbf{p}(z)\big) \right|^2}{\partial W_y} = W_y^2 \left[1 - 2W_y^2 \left(y - Y\right)^2\right] \frac{|u|^2}{C^2}, \\
M_P(\mathbf{r}) &:= \frac{W_x(z)}{2C^2(z)} \frac{\partial \left| u\big(\mathbf{r}_\perp, \mathbf{p}(z)\big) \right|^2}{\partial W_x} + \frac{W_y(z)}{2C^2(z)} \frac{\partial \left| u\big(\mathbf{r}_\perp, \mathbf{p}(z)\big) \right|^2}{\partial W_y} + \quad \frac{1}{2C(z)} \frac{\partial \left| u\big(\mathbf{r}_\perp, \mathbf{p}(z)\big) \right|^2}{\partial C} \\
&= \left[2 - W_x^2 \left(x - X\right)^2 - W_y^2 \left(y - Y\right)^2\right] \frac{|u|^2}{C^2}
\end{aligned}
$$

The above system of 9 stochastic differential equations forms the variational scaling law. We derived this reduced system by using the variational formulating the paraxial Helmholtz equation along with the Gaussian ansatz. The variational scaling law has a computational advantage over the paraxial Helmholtz equation because the reduced model requires tracking only the nine beam parameters for the duration of the propagation, while the PDE model requires tracking the entire field across the transverse plane for the duration of propagation. In the next section, we present numerical results comparing the performance of the variational scaling law to the paraxial Helmholtz equation.

2.4 Numerical Model Results

To illustrate that the variational scaling law (VSL) well-approximates the solution to the paraxial stochastic Helmholtz equation, the statistics, especially the average, of an ensemble of the beam propagation realizations from the solution to the Helmholtz equation is compared to the average result from the VSL approach. Note that the ensemble statistics for the VSL converge with fewer realizations compared to the waveoptics approach. However, in the results presented below, the ensemble statistics are computed for 400 realizations of both models. For these comparisons, the

VSL and the paraxial Helmholtz equation are supplied with the same initial conditions, and the perturbation to the index of refraction are randomly sampled using the same statistical characteristics. The realizations of the index of refraction at any given discrete longitudinal point are generated using the *circulant embedding* method outlined in [30].

The stochastic paraxial Helmholtz equation (the waveoptics approach) is solved via a Strang-splitting (split-step) scheme in which the stochastic term is treated separately from the diffusive term. A Strang-splitting scheme is a standard numerical method for solving partial differential equations, including the paraxial Helmholtz equation [31, 32]. In this model, the transverse plane is equipped with periodic boundary conditions; however, the transverse domain is always chosen large enough that the beam does not substantially encounter these periodic boundaries. The diffusive term is treated with the fast Fourier transform (FFT) algorithm, and the stochastic term is viewed as a phase contribution for each particular realization of the refractive index (δn_{turb}). For simplicity, the governing set of stochastic ODEs corresponding to the VSL is solved via the backwards Euler implicit method.

2.4.1 Atmospheric Turbulence in Model

In this section we specify the statistical model used in the simulations for the turbulent perturbations to the index of refraction. Recall, we assume δn_{turb} is described by a random process which is stationary and isotropic in the transverse plane [4]. When a random process is stationary it is convenient to work with the structure function instead of the correlation function. In general, the structure function for the index of refraction $\delta n_{\text{turb}}(\mathbf{r}_\perp)$ is denoted

$$\mathbb{E}\left[(\delta n_{\text{turb}}(\mathbf{r}_{\mathbf{1},\perp}) - \delta n_{\text{turb}}(\mathbf{r}_{\mathbf{2},\perp}))^2\right],$$

where $\mathbb{E}$ denotes the expectation and $\mathbf{r}_\perp = (x, y)$. Since we assume the random process is stationary and isotropic, this means the structure function only depends on $\|\mathbf{r}_{\mathbf{1},\perp} - \mathbf{r}_{\mathbf{2},\perp}\|$.

Commonly, the optical turbulence is represented through the Kolmogorov model [4] in which the stochastic variations of the index of refraction in the transverse plane are described by the

structure function:

$$\mathbb{E}\left[(\delta n(\boldsymbol{r}_{1,\perp}) - \delta n(\boldsymbol{r}_{2,\perp}))^2\right] = 2\left(1 - \operatorname{cor}(\delta n(\boldsymbol{r}_1), n(\boldsymbol{r}_2))\right)$$
$$= \frac{\widehat{C_n}^2 \widehat{l_0}^{\frac{2}{3}}}{\sigma_n^2} \begin{cases} |\boldsymbol{r}_{1,\perp} - \boldsymbol{r}_{2,\perp}|^2, & \text{for } 0 < |\boldsymbol{r}_{1,\perp} - \boldsymbol{r}_{2,\perp}| \leq 1 \\ |\boldsymbol{r}_{1,\perp} - \boldsymbol{r}_{2,\perp}|^{\frac{2}{3}}, & \text{for } 1 < |\boldsymbol{r}_{1,\perp} - \boldsymbol{r}_{2,\perp}| \leq \frac{1}{\varepsilon} \end{cases},$$

where $\varepsilon = \widehat{l_0}/\widehat{L_0}$, and $\widehat{l_0}$ and $\widehat{L_0}$ are the characteristic length scales used to nondimensionalize the transverse and propagation directions, respectively. We call the constants $\widehat{l_0}$ and $\widehat{L_0}$ the inner scale and the outer scale of the atmospheric turbulence, respectively. Thus, the correlation function is represented as

$$\operatorname{cor}(\delta n_1, \delta n_2) = 1 -$$
$$\frac{\widehat{C_n}^2 \widehat{l_0}^{\frac{2}{3}}}{2\sigma_n^2} \begin{cases} |\boldsymbol{r}_{1,\perp} - \boldsymbol{r}_{2,\perp}|^2, & \text{for } 0 < |\boldsymbol{r}_{1,\perp} - \boldsymbol{r}_{2,\perp}| \leq 1 \\ |\boldsymbol{r}_{1,\perp} - \boldsymbol{r}_{2,\perp}|^{\frac{2}{3}}, & \text{for } 1 < |\boldsymbol{r}_{1,\perp} - \boldsymbol{r}_{2,\perp}| \leq \frac{1}{\varepsilon} \end{cases}.$$

If we assume that $|\operatorname{cor}(\delta n_1, \delta n_2)| \approx 0$ for $|\boldsymbol{r}_{1,\perp} - \boldsymbol{r}_{2,\perp}| \approx 1/\varepsilon$, then the variance of the index of refraction can be approximated as

$$\sigma_n^2 \approx \frac{\widehat{C_n}^2 \widehat{L_0}^{2/3}}{2} \text{ and}$$
$$\operatorname{cor}(n_1, n_2) = 1 - \begin{cases} |\boldsymbol{r}_1 - \boldsymbol{r}_2|^2, & \text{for } 0 < |\boldsymbol{r}_1 - \boldsymbol{r}_2| \leq 1 \\ |\boldsymbol{r}_1 - \boldsymbol{r}_2|^{2/3}, & \text{for } 1 \leq |\boldsymbol{r}_1 - \boldsymbol{r}_2| \leq 1/\varepsilon \end{cases}.$$

Note that $\sigma_n \equiv \sigma$ from the nondimensional parameters.

Recall, in our derivation of the paraxial Helmholtz equation we chose a dominant scaling for the Helmholtz equation that resulted in both the paraxial and white noise approximations. This allows us to treat δn_{turb} as delta-correlated in the z-direction and we can use the correlation function in the

transverse plane, cor, to obtain the correlation function for $\mathbb{R}^3$, i.e.

$$\widetilde{\text{cor}}(\delta n_{\text{turb}}(\mathbf{r_1}, z_1), \delta n_{\text{turb}}(\mathbf{r_1}, z_2)) = \text{cor}(\delta n_{\text{turb}}(x_1, y_1), \delta n_{\text{turb}}(x_2, y_2))\delta_D(z_1 - z_2),$$

where δ_D represents the Dirac-delta function. We note that other statistical models could be used for index of refraction perturbations, but we chose the Kolmogorov model due to its simplicity and presence in the literature.

In the numerical implementations for both the VSL and the waveoptics model, the atmospheric turbulence is being represented by a layered-atmosphere model [33, 34]. In this approach, we begin with a continuous, constant index structure profile, $\widehat{C_n}^2(\widehat{z}) = C_0$, and use this to compute an *effective index structure constant*, $\widehat{C_{n,i}}^2$ for each numerical propagation step. The effective index structure constant is selected such that many of the low-order moments of the continuous model are equal to the layered model:

$$\int_0^{\widehat{L}} \widehat{C_n}^2(\widehat{z'})(\widehat{z'})^m d\widehat{z'} = \sum_{i=1}^{N_z} \widehat{C_{n,i}}^2 \widehat{z_i}^m \Delta\widehat{z}, \quad 0 \leq m \leq 7 \tag{2.26}$$

where N_z is the number of propagation steps in the z-direction, $\widehat{L}$ is the propagation distance, and $\Delta\widehat{z} = \widehat{L}/N_z$ is the z-step size. To measure the strength of the turbulence, the Fried parameter, $\widehat{r_0}(\widehat{z})$, and the log-amplitude variance, $\sigma_\chi^2(\widehat{z})$, is calculated with the effective index structure constant [34]. Note that, when $\sigma_\chi^2(\widehat{z}) < 0.25$, the model conditions represent weak turbulence, and when $\sigma_\chi^2(\widehat{z}) \gg 0.25$, the model conditions represent strong turbulence [4, 34]. For the numerical results in the following, we use three turbulence strengths to assess the VSL, $\widehat{C_n}^2(\widehat{z}) = 1 \cdot 10^{-16}$, $4 \cdot 10^{-16}$, and $9 \cdot 10^{-16}$ $m^{-2/3}$. The corresponding Fried parameters and log-amplitude variances, for $\widehat{z} = 6000$ m, are presented in Table 2.3.

These turbulence statistical properties paired with the effective index structure constant are used in the numerical results presented hereafter for both the VSL and the waveoptics model.

Table 2.3: The Fried parameters and log-amplitude variances at 6000 m.

$\widehat{C_n}^2$	$\widehat{r_0}$	σ_χ^2	turbulence strength
$1 \cdot 10^{-16}$	0.18	0.046	weak
$4 \cdot 10^{-16}$	0.10	0.18	medium
$9 \cdot 10^{-16}$	0.06	0.41	strong

2.4.2 Model Parameters

For the numerical comparison the VSL and the waveoptics model (scalar paraxial stochastic Helmholtz equation) are initialized as follows. First, the dimensional constants and characteristic scales are defined, and then the nondimensional counterparts are calculated. When computing the model parameters that depend on the index structure constant, $\widehat{C_n}^2$, we instead utilize the set of effective index structure constants, $\{\widehat{C_{n,i}}^2\}_{i=1,\dots,N_Z}$, to compute effective model parameters [34]. Particularly, a set of effective index structure variance parameters, σ_i^2, is computed using

$$\sigma_{n,i}^2 = \frac{\widehat{C_{n,i}}^2 \widehat{L_0}^{2/3}}{2}, \quad i = 1, \dots N. \tag{2.27}$$

The effective variance parameter is then used to compute the effective scaled turbulence strength, $\gamma_i^2 = (\widehat{l_0}\widehat{k_0})^2 \sigma_{n,i}$, to be used in the numerical simulations for both models. The values of the physical constants used for the proceeding numerical results are given in Table 2.4, and their corresponding scaled quantities are presented in Table 2.5. The effective parameters, $\widehat{C_{ni}}^2$, γ_i, and σ_i^2 are no longer constant over the propagation distance, so their values are not reported in Table 2.4 and Table 2.5. Since loss is not being considered: $\zeta = 0$.

2.4.3 Initial Conditions

The initial condition for both the VSL and the waveoptics model will be given by the Gaussian ansatz (2.20), using the ten parameters that describe the Gaussian. We will consider two initial conditions, both of which are inspired by the deterministic Gaussian beam profile as described in Section 2.2.2. Specifically, for the turbulence strength analysis, we use the following initial parameters for a symmetrical focusing Gaussian beam, centered on the origin, without any tip/tilt:

Table 2.4: The values of the physical constants and characteristic scales that describe the propagating laser field.

physical quantity	symbol	value
wavelength	$\widehat{\lambda}$	10^{-6} m^{-1}
inner-scale	$\widehat{l_0}$	10^{-3} m
outer-scale	$\widehat{L_0}$	10^{2} m
aperture diameter	$\widehat{D}$	$2 \cdot 10^{-2}$ m
propagation distance	$\widehat{L_z}$	6000 m
focusing distance	$\widehat{z_w}$	5000 m
background index	$\hat{n}$	$1 + 10^{-6}$
transverse length x	$\widehat{L_x}$	1.25 m
transverse length y	$\widehat{L_y}$	1.25 m

Table 2.5: A listing of some scaled quantities and their corresponding values based on the given parameters of Table 2.4.

computational quantity	symbol	value
transverse length x	$L_x = \widehat{L_x}/\widehat{l_0}$	625
transverse length y	$L_y = \widehat{L_y}/\widehat{l_0}$	625
propagation distance	$L_z = \widehat{L_z}/\widehat{L_0}$	60
scaled aperture	$D = \widehat{D}/\widehat{l_0}$	20
wavenumber strength	$\xi = \widehat{l_0}^2 \widehat{k_0^\ell}/\widehat{L_0}$	0.0623
loss strength	$\zeta = \widehat{l_0}^2 \widehat{k_0^\ell} \widehat{\alpha_{\text{loss}}^\ell}$	0

$$
\begin{aligned}
C(0) &= 100 = C \\
W_x(0) = W_y(0) &= \frac{w_0\sqrt{n\xi}}{\sqrt{w_0^4 + (0 - z_w)^2}} \\
T_x(0) = T_y(0) &= 0 \\
X(0) = Y(0) &= 0 \\
F_x(0) = F_y(0) &= \frac{-0.5n\xi(0 - z_w)}{w_0^4 + (0 - z_w)^2} \\
P(0) &= -\arctan\left(\frac{z_w}{w_0^2}\right)
\end{aligned}
\quad , \tag{2.28}
$$

where z_w is a specified scaled location and w_0 is the initial beam waist size. The location is prescribed to be $z_w = 50$, equivalently $\widehat{z_w} = 5000$ meters, and the initial beam waist size is taken

to be one quarter the diameter of the computational domain diameter: $w_0 = D/4 = 5$. In vacuum propagation, following the solution in Section 2.2.2, the above initial condition corresponds to a Gaussian beam that focuses over the propagation length until a minimum beam width is attained at $\widehat{z} = \widehat{z_w} = 5000$ m and the beam remains perfectly symmetrical and centered at $x = 0$ and $y = 0$ for all time. The second initial condition is a modification of the first one to incorporate asymmetry and tip/tilt into the model. The initial parameters that have changed from the first initial condition, (2.28), to the second initial condition are: $W_x(0) = 4W_y(0)$, $T_x(0) = 0.25$, $T_y(0) = -0.5$, $X(0) = 250$, and $Y(0) = -250$. In vacuum propagation, the second initial condition represents a beam whose center travels from the bottom right to the top middle in the transverse plane.

Note that the beam width parameters in the VSL are proportional to the inverse of the physical width of the beam. With this initial condition, any tilt in the system is strictly introduced through the interaction of the beam with the turbulent atmosphere. In vacuum, i.e. $\delta n_{\text{turb}} = 0$, this initial condition choice allows us to know apriori the beam waist size and location. This is helpful for the case of weak atmospheric turbulence because we can expect that the beam waist size and location will be a perturbation away from the prescribed location in the initial condition. The initial irradiance for the symmetrical initial condition is in Fig. 2.1 and the asymmetrical initial condition is in Fig. 2.2. Note that the figures are presented in dimensional units.

From the derivation of the models, it is expected that the total beam power is conserved throughout the propagation distance for both VSL and waveoptics. Thus, it is important to ensure the selected numerical methods for both models still conserve the total beam power. This can be easily checked by simply computing

$$C(z) \approx \left(\int_{-L}^{L} \int_{-L}^{L} |a|^2 dx dy \right)^{1/2}$$

at each propagation step and we expect this to remain equal to the initial power of the beam. Fig. 2.3 shows the conservation of beam power over the propagation length for both models. The waveoptics approach shows a slight decrease in power, but it is equivalent a 0.0048% difference from the initial power of 100.

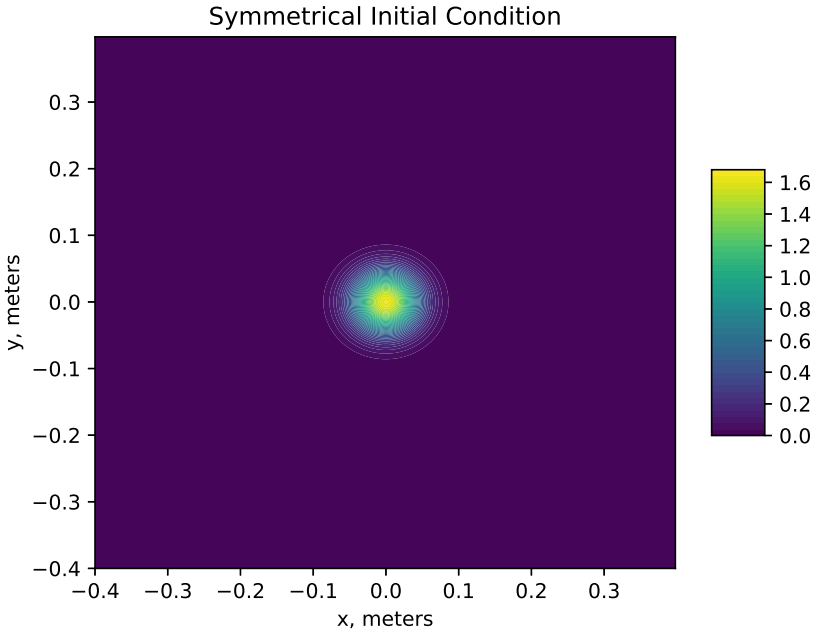

Figure 2.1: The symmetrical initial condition irradiance.

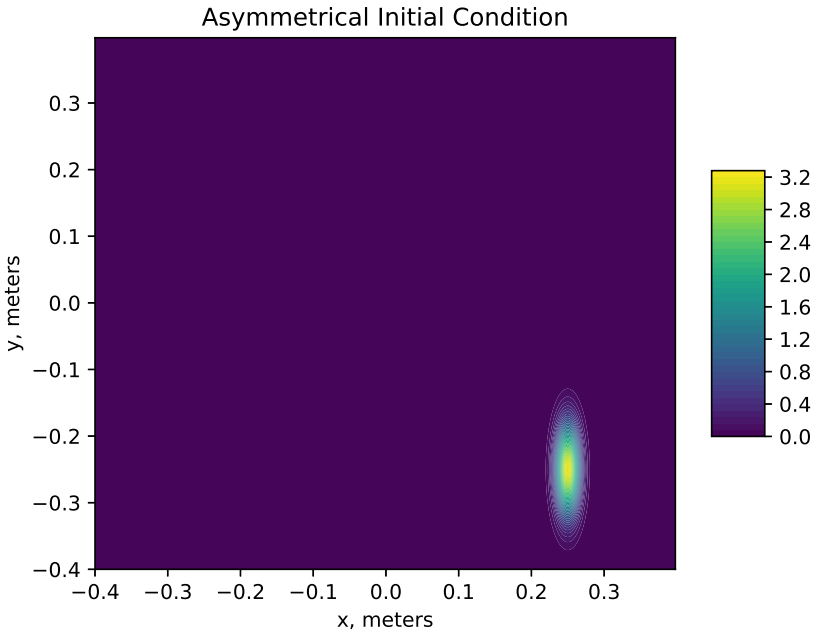

Figure 2.2: The asymmetrical initial condition irradiance.

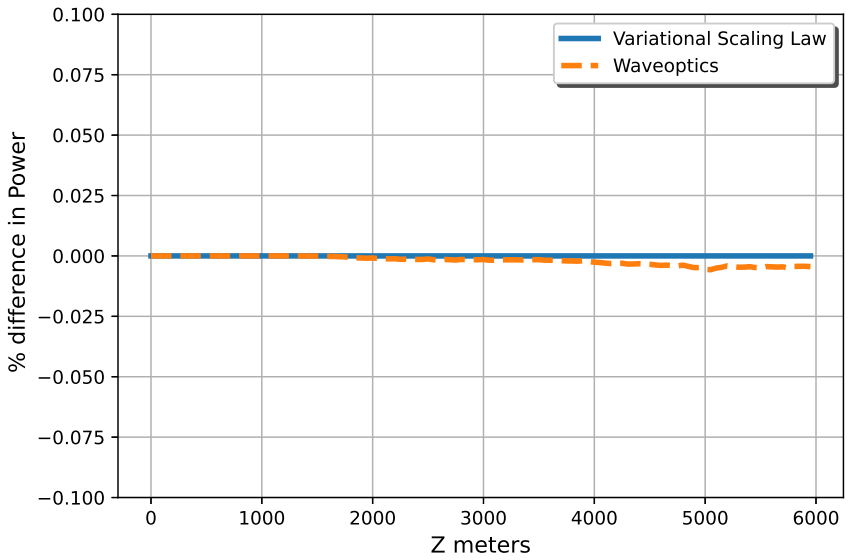

Figure 2.3: The beam power is conserved for both VSL and waveoptics, $C(\widehat{Z}) \approx C(0) = 100$ for all $\widehat{z}$.

2.4.4 Symmetrical Initial Condition Comparison to Waveoptics

To assess the accuracy of the VSL in comparison to the waveoptics approach, an ensemble of 400 independent runs/realizations is conducted, and the average irradiance from both models are compared using the turbulence strengths in Table 2.3 for the symmetrical initial condition. In this section and the next, the figures show results for the medium turbulence strength, and note that the colorbar scale may differ from figure to figure.

To compare the difference in the value of the average peak irradiance from the two models we look at one-dimensional slices through the irradiance profile in both the x- and y-directions. Recall, the irradiance is found as the magnitude squared of the electric field. The errors are computed with the discrete 2-norm as relative errors such that the waveoptics solution is considered to be trusted. For notational convenience, let $I_p^L(x, y)$ be the peak irradiance from the VSL solution and $I_p^H(x, y)$ be the peak irradiance from the waveoptics solution. If we let $I(x, y)$ represent one of the above irradiances, then an x-slice through the irradiance is defined to be $I_x(y) = I(0, y)$ and a y-slice is defined to be $I_y(x) = I(x, 0)$. The average peak irradiance profile, $I_y(x)$, for medium turbulence, is shown in Fig. 2.4. The relative error between the irradiance profiles is reported in Table 2.6.

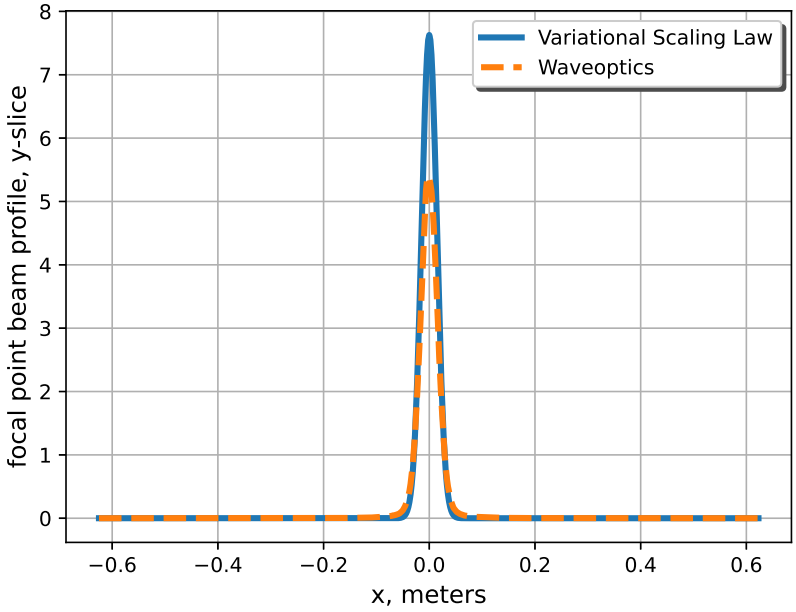

Figure 2.4: A comparison of a slice through the average irradiance along the line $x = 0$ at $\widehat{z} = 5000$ m ($\sigma_\chi^2 = 0.18$) for the symmetrical initial condition.

Another measure for the accuracy is given by tracking the value of the peak irradiance. For the VSL solution, this is simply given by the irradiance at the center of the Gaussian, which is at the mesh coordinates nearest to the $X = X(z)$ and $Y = Y(z)$ variables. In the case of waveoptics, the location of the center irradiance is approximated numerically from the average of the ensemble. The center irradiance of the VSL solution will be denoted by $I^L_{\text{center}}(z)$, and the average center irradiance of the waveoptics solution will be denoted by $I^H_{\text{center}}(z)$. The center irradiance is recorded for each propagation step, and again the relative error between the two models is measured in the 2-norm. The relative error for the peak irradiance along the propagation path is shown in Table 2.7, and illustrated in Fig. 2.5.

Table 2.6: The relative error of the average the irradiance x- and y-axis profiles for the symmetrical initial condition.

σ_χ^2	x-slice error	y-slice error
0.046	$2.30 \cdot 10^{-1}$	$2.41 \cdot 10^{-1}$
0.18	$3.62 \cdot 10^{-1}$	$3.41 \cdot 10^{-1}$
0.41	$7.52 \cdot 10^{-1}$	$8.13 \cdot 10^{-1}$

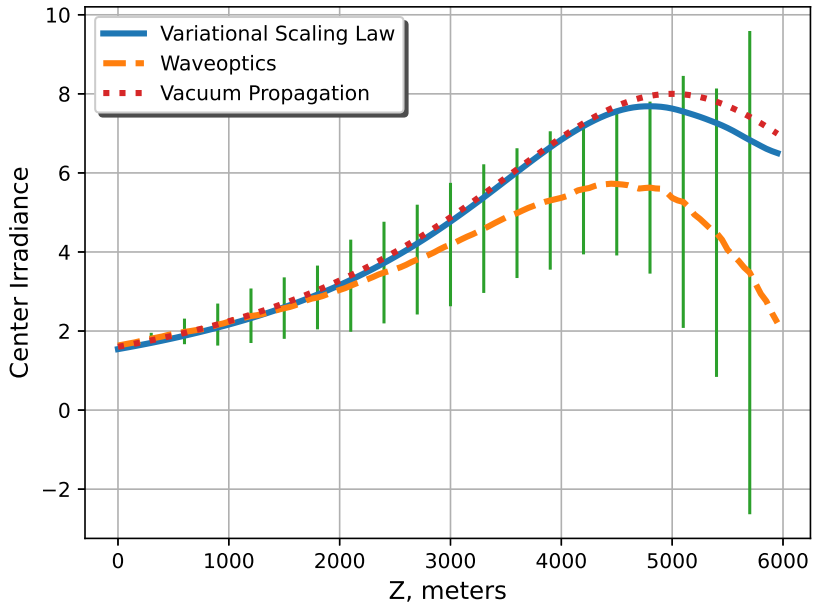

Figure 2.5: A comparison of the average center irradiance as a function of propagation distance ($\sigma_\chi^2 = 0.18$) for the symmetrical initial condition. The green bars represent the variance of the waveoptics solution over the 400 runs.

Another metric of comparison is found in the width of the beam. This width evolves as the light propagates, and the absolute peak irradiance over the propagation distance ought to correspond to the minimum beam width (the focal point). As a standard convention, the overall beam width for a given 1D slice through the Gaussian irradiance is bounded by the locations were the irradiance diminishes by a factor of $1/e^2$ from its peak. Again, only two slices centered on the x- and y-axes will be used for this calculation, producing a width value for each slice. Over the propagation distance, the relative error, measured in 2-norm, of the beam width, calculated separately for the x- and y-slices through the irradiance profile, are given in Table 2.8.

Table 2.7: The relative error of the average center irradiance for the symmetrical initial condition.

σ_χ^2	center irradiance error
0.046	$9.6 \cdot 10^{-2}$
0.18	$3.68 \cdot 10^{-1}$
0.41	$6.73 \cdot 10^{-1}$

Table 2.8: The relative error of the beam width, calculated for x- and y-slices through the irradiance profile for the symmetrical initial condition.

σ_χ^2	x beam width error	y beam width error
0.046	$2.3 \cdot 10^{-2}$	$2.3 \cdot 10^{-2}$
0.18	$7.46 \cdot 10^{-2}$	$7.16 \cdot 10^{-2}$
0.41	$1.83 \cdot 10^{-1}$	$1.72 \cdot 10^{-1}$

The evolution of this beam width for the y-slice is depicted in Fig. 2.6 when $\sigma_\chi^2 = 0.18$. Lastly, we consider the relative error in focal point/beam waist location in propagation, $\widehat{z_w}$. In vacuum propagation, the beam waist location of the symmetric focusing Gaussian beam initial condition is at $\widehat{z_w} = 5000$ m. In the presence of turbulence the location of the beam waist fluctuates and, on-average, it occurs slightly before the vacuum propagation beam waist location. The relative error in the beam waist location in propagation is given in Table 2.9.

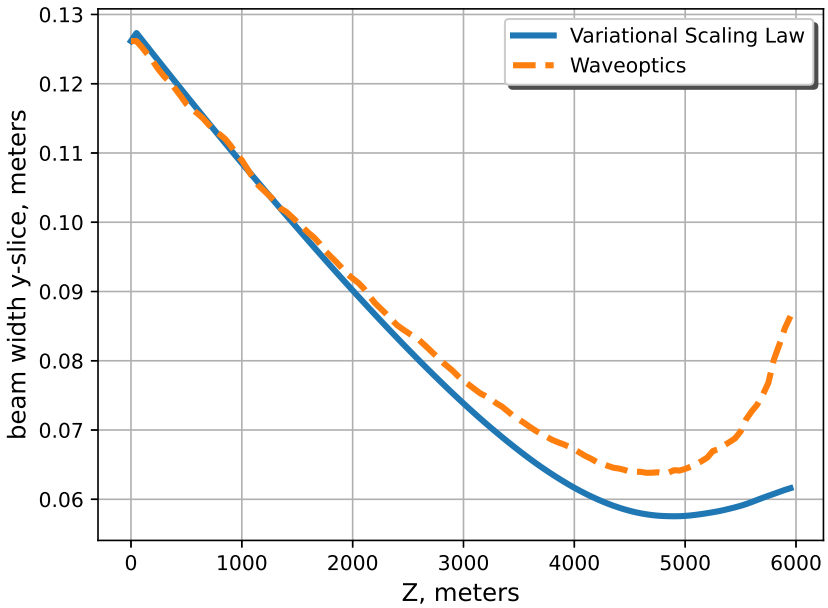

Figure 2.6: A comparison of the beam width as a function of propagation distance calculated from the centered y-slice through the irradiance profile ($\sigma_\chi^2 = 0.18$) for the symmetrical initial condition.

As shown by this example, the VSL well-approximates the solution to the waveoptics approach in the presence of weak turbulence, $\sigma_\chi^2 < 0.25$. The approximation the VSL provides deteriorates

Table 2.9: The relative error of the propagation location of the focal point or beam waist for the symmetrical initial condition.

σ_χ^2	relative error in $\widehat{z_w}$
0.046	$3.12 \cdot 10^{-2}$
0.18	$8.11 \cdot 10^{-2}$
0.41	$9.35 \cdot 10^{-2}$

as the turbulence strengthens, which is expected since the VSL was derived under the assumption of weak turbulence. However, in presence of strong turbulence, the VSL still well-approximates the beam width and location of the focal point, despite the poor approximation in the average center irradiance value.

2.4.5 Asymmetrical Initial Condition Comparison to Waveoptics

In this section, we compare the VSL to waveoptics simulations with an initial condition of nonzero tip/tilt. The asymmetrical initial irradiance for this initial condition is shown in Fig. 2.2. From vacuum propagation with the asymmetric initial condition, we expect the beam center to move from the bottom right corner to the top middle of the transverse plane.

The irradiance for each model at propagation distances $\widehat{z} = 3000$ m and $\widehat{z} = 6000$ m are shown in Figs. 2.7 and 2.8, respectively. Qualitatively, we can see that the waveoptics irradiance is roughly the equal to the VSL irradiance.

Particularly, the y-coordinate of the beam center increases from -0.25 to approximately 0.2 and the x-coordinate of the beam decreases from 0.25 to approximately 0. This is confirmed by comparing the average value of the beam's center coordinates for both models over the ensemble average, see Fig. 2.9. The average value of the center coordinates for the VSL is computed as the ensemble average of the beam parameters $X(z)$ and $Y(z)$, and for the waveoptics simulations the center coordinates are approximated from the average irradiance. The relative error, computed over the propagation distance, is in the average beam center coordinates is shown in Table 2.10.

Lastly, we compare the value of the average center irradiance for the asymmetric initial condition. Fig. 2.10 shows the center irradiance value over the propagation distance for the VSL, the

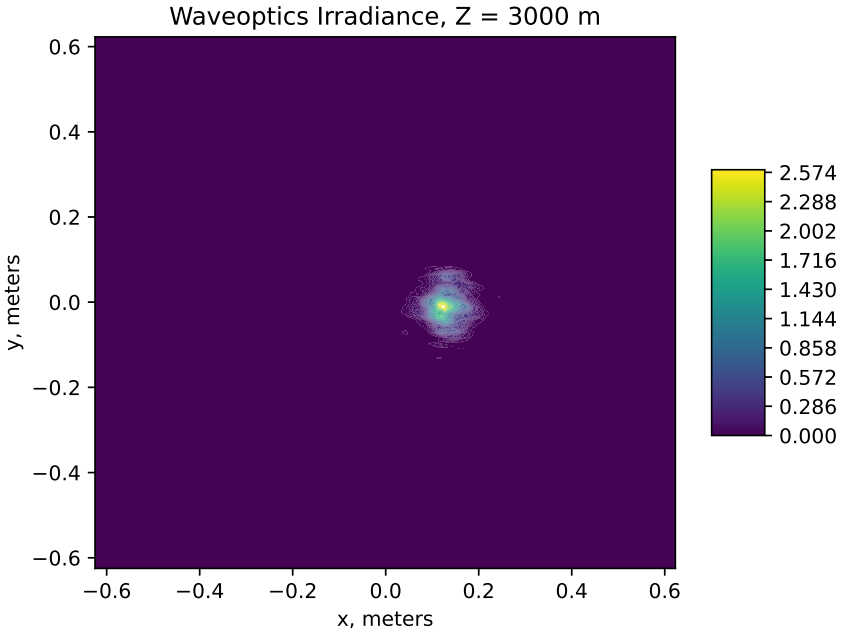

(a) Waveoptics Irradiance, $\widehat{z} = 3000$ m

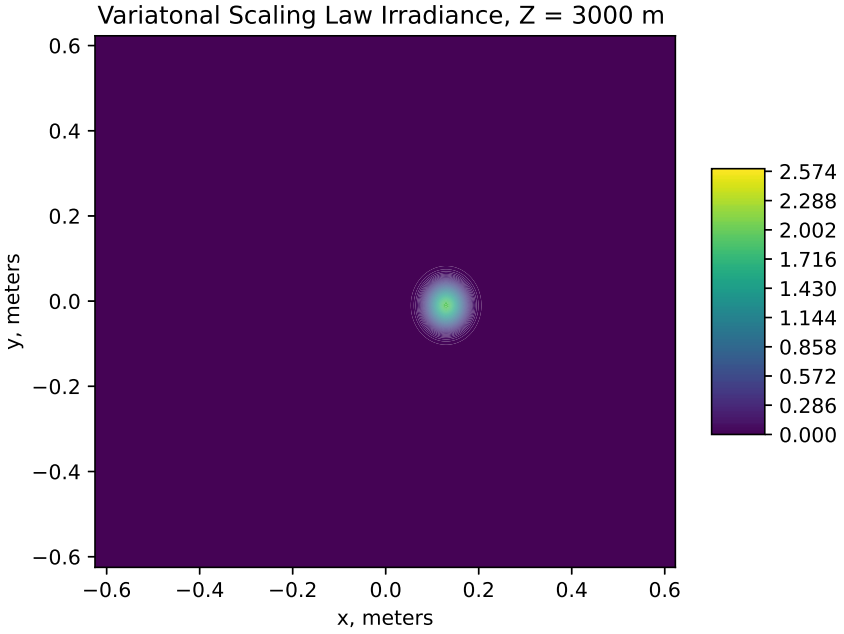

(b) VSL Irradiance, $\widehat{z} = 3000$ m.

Figure 2.7: A comparison irradiance at $\widehat{z} = 3000$ m computed with *one* ensemble run of each model for the asymmetrical initial condition and $\sigma_\chi^2(3000) = 0.108$.

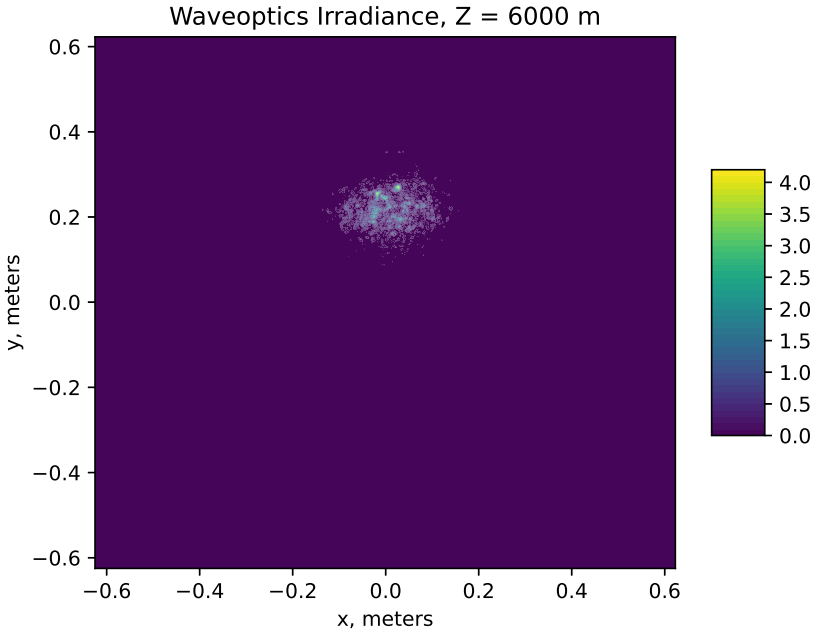

(a) Waveoptics Irradiance, $\widehat{z} = 6000$ m

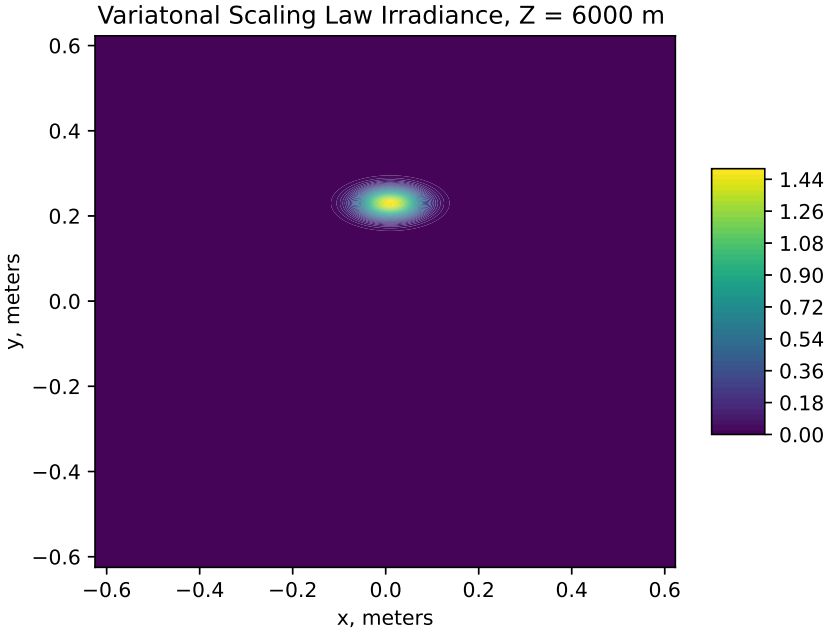

(b) VSL Irradiance, $\widehat{z} = 6000$ m.

Figure 2.8: A comparison irradiance at $\widehat{z} = 6000$ m computed with *one* ensemble run of each model for the asymmetrical initial condition and $\sigma_\chi^2(6000) = 0.18$.

Table 2.10: The relative error of the beam center coordinates and the center irradiance for the asymmetrical initial condition.

σ_χ^2	x-coord.	y-coord.	center irradiance
0.046	$8.66 \cdot 10^{-3}$	$2.08 \cdot 10^{-2}$	$3.41 \cdot 10^{-2}$
0.18	$1.93 \cdot 10^{-2}$	$4.24 \cdot 10^{-2}$	$1.57 \cdot 10^{-1}$
0.41	$2.82 \cdot 10^{-2}$	$7.15 \cdot 10^{-2}$	$2.83 \cdot 10^{-1}$

waveoptics model, and vacuum propagation, and the corresponding relative error can be found in Table 2.10. For the considered levels of turbulence, we feel that these errors between the VSL and the waveoptics model are quite reasonable.

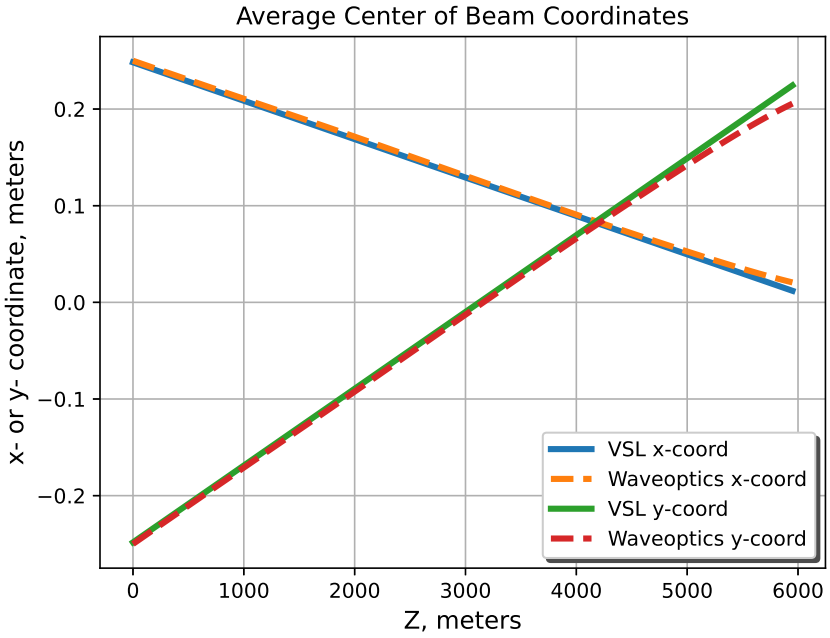

Figure 2.9: The ensemble average of the center coordinates of the beam for the asymmetrical initial condition when $\sigma_\chi^2 = 0.18$.

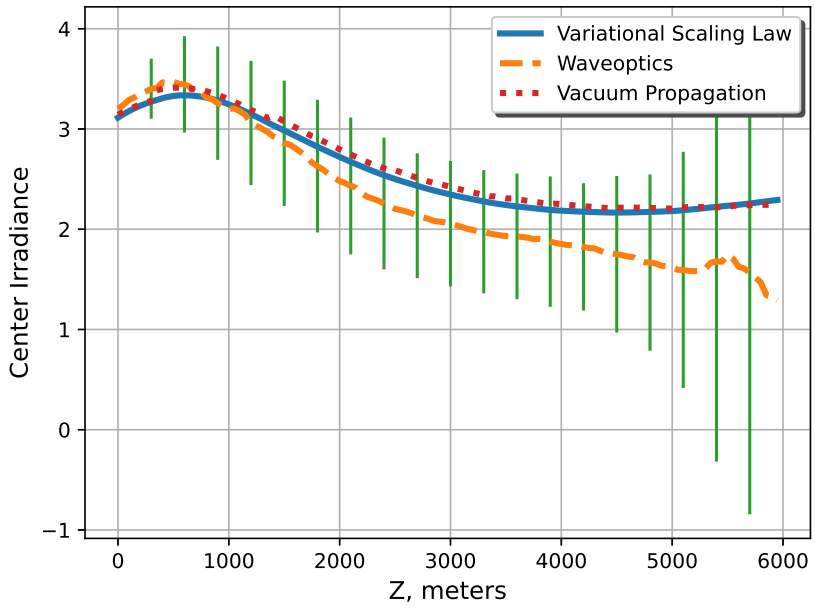

Figure 2.10: The ensemble average of the center irradiance value for both models with the asymmetrical initial condition when $\sigma_\chi^2 = 0.18$. The green bars represent the variance of the waveoptics solution over the 400 runs.

2.5 Conclusions

This project introduced a new approximation method for atmospheric propagation of a Gaussian laser beam based on a variational approach, which we call the variational scaling law. The derivation of the VSL is based on pairing a variational formulation of the stochastic paraxial Helmholtz equation with a parameterized Gaussian beam ansatz. Because the Gaussian ansatz is determined in the transverse plane and the beam parameters are parameterized in the propagation direction, we can reduce the variational formulation using the Euler-Lagrange equations to a set of stochastic differential equations that describe the dynamics of the nine beam parameters. Through the numerical comparisons presented in Section 2.4, we have shown that the VSL is a reasonable approximation to the paraxial Helmholtz equation. In the presented examples, the VSL approximation is at least order-one compared to the waveoptics simulations. The VSL consistently over-estimated the value of the irradiance compared to the waveoptics approach and this is likely due to the fact the beam profile remains Gaussian for the propagation duration, unlike

the in the waveoptics approach. Compared to the irradiance overestimation observation, the VSL more accurately predicts the location of the focal point in the propagation distance and the width of the beam when compared to the waveoptics simulations. Another notable feature of the VSL is the reduction in memory requirements compared to the waveoptics approach because we are only required to track the nine beam parameters and we can recover the corresponding electric field using the Gaussian ansatz, while the waveoptics approach requires tracking the electric field at each propagation step. The memory advantage of the VSL is clearly dependent on the discretization parameters chosen for the waveoptics approach. A future direction of the VSL would be to incorporate thermal blooming by coupling the model to the heat equation. We believe the heat profile of the atmosphere surrounding the Gaussian beam can also be described by a Gaussian ansatz which can lead to a parameterized representation of the heat-profile. On the propagating laser beam the effects of thermal blooming result in even further dispersion of the beam than what is observed with optical turbulence. Another future direction would be to formulate the VSL for non-Gaussian trial solutions using, for example, the Zernike polynomial expansion for the beam profile.

We now turn our attention to the quantum transport perspective of wave propagation. We begin by introducing the mathematical models used for quantum transport and, specifically, focus on the quantum Liouville-BGK equation. The remainder of the dissertation focuses on the definition, analysis, and implementation of a numerical scheme for the quantum Liouville equation.

Chapter 3

The Quantum Transport Model

Electron transport in semiconductors has been widely studied since the introduction of diodes and transistors in the 1940s. The classical description of electron transport is based on the Boltzmann equation. However, as technology has advanced, these semiconductor devices have been reduced to nanometer scale and the quantum effects in the electron transport must be taken into account. One such device is a Resonant Tunneling Diode (RTD) which is a layered semiconductor structure which was introduced in 1974 [35]. These devices are commonly created with layers of semiconductors such as Gallium Arsenide and Aluminum Gallium Arsenide where the layers are only a few nanometers thick. The layered structure of the RTD can be reduced to a simplified one-dimensional model where the main axis is orthogonal to the layers and translational symmetry is assumed in the directions parallel to the layers [36]. The one-dimensional model is characterized by a potential profile that contains at least two potential barriers that sandwich a potential well. At this spatial-scale the classical description is no longer sufficient as the RTD relies on quantum tunneling of electrons through the potential barriers [36]. Thus a quantum model is required for an accurate description of these nanometer-scale devices. From the quantum perspective, one can study electron transport on a microscopic scale with the Schrödinger equation, a mesoscopic scale using quantum statistical physics, and on a macroscopic scale using quantum fluid models [36]. In the mesoscopic case we use the quantum Liouville equation, which is given by:

$$i\hbar\partial_t \varrho = [\mathcal{H}, \varrho] + i\hbar\mathcal{Q}(\varrho), \tag{3.1}$$

where $\hbar$ is the reduced Planck's constant and i is the imaginary unit. Above, ϱ is a density operator (matrix) which represents a statistical mixture of quantum states, $\mathcal{H}$ is a Hamiltonian operator, $\mathcal{Q}$ is a collision operator, and the brackets represent the commutator between two operators, i.e.

$[A, B] = AB - BA$. A density operator is a positive, self-adjoint, trace class operator that satisfies $\mathrm{Tr}(\varrho) = 1$.

To simplify the description of the these quantum systems, macroscopic models are derived from the quantum Liouville equation. These quantum macroscopic models are also called quantum fluid or hydrodynamic models and they describe the dynamics of the moments of the density operator [1, 37–40]. As in the kinetic case, the quantum fluid models that are derived from a hierarchy of moment equations require some extra work to be written in a closed form because the higher order moments do not only depend on the lower order moments. In the kinetic case, Levermore in [41] proposed a moment closure procedure based on an entropy minimization principle. To solve this moment closure problem in the quantum setting, Degond and Ringofer in [1] transposed Levermore's work to the quantum setting. The theory of Degond and Ringhofer introduces a *local quantum equilibrium* operator whose moments are known because the operator is obtained by minimizing the entropy under relevant local moment constraints. This quantum equilibrium operator is the key ingredient in closing the moment equations to derive any given quantum fluid model.

Since the quantum Liouville equation (QLE) (3.1) is the so-called "mother" of all quantum hydrodynamic models, it is important to have a good understanding of this equation. In this work, we focus on the numerical resolution of the QLE and where the collision operator in (3.1) is taken to be a relaxation-type collision operator,

$$\mathcal{Q}(\varrho) = \frac{1}{\tau}(\varrho_{\mathrm{e}}[\varrho] - \varrho). \tag{3.2}$$

Here τ is the relaxation time and $\varrho_{\mathrm{e}}[\varrho]$ is the local quantum equilibrium obtained by minimizing the free energy (i.e. relative entropy). This operator is also called the Bhatnagar–Gross–Krook (BGK) collision operator [42]. To appropriately define the quantum equilibrium operator in (3.2) we will first review the quantum moment closure procedure of Degond and Ringhofer, as it is the basis for the definition of the equilibrium operator. The main goals of this project are to define a numerical scheme for the QLE and perform both theoretical and numerical convergence analysis of

the numerical scheme. As an application of the numerical scheme, I will numerically investigate the effects of different collision regimes on the transport of electrons. The quantum Liouville equation equipped with the BGK-collision operator represents a regime in which both ballistic transport and electron collisions are taken into account. For a collisionless model, we use the ballistic quantum Liouville equation,

$$i\hbar\partial_t \varrho = [\mathcal{H}, \varrho], \tag{3.3}$$

which is simply the QLE without scattering. On the other end of the spectrum, the collision-dominated model is given by the quantum drift-diffusion model (QDD) which can be derived from the QLE via a diffusive limit or the quantum entropy minimization principle [43,44]. The quantum drift-diffusion model,

$$\partial_t n + \nabla \cdot (n \nabla \mathcal{A}) = 0, \tag{3.4}$$

is an example a macroscopic model for electron transport and it describes the dynamics of the local particle density n, which is the first moment of ϱ that solves the QLE. For the QDD model, the local density n is obtained from the spectral elements of the Hamiltonian $\mathcal{H}[\mathcal{A}] = \mathcal{H}_0 + \mathcal{A}$ where $\mathcal{A}$ is the chemical potential and $\mathcal{H}_0$ is the free Hamiltonian.

In the remainder of this chapter, we begin by introducing the mathematical framework for the QLE in Section 3.1. Afterwards, in Section 3.2 we review the theory of Degond and Ringhofer and the entropy minimization principle which gives rise to the definition of the local quantum equilibrium operator in the BGK-collision operator. Lastly, in Section 3.3, we use the entropy minimization principle of Degond and Ringhofer's theory to appropriately define the BGK-collision operator. In Chapter 4, a semi-discrete in time Strang splitting scheme for the quantum Liouville equation is introduced and we show that the scheme is convergent in time. Lastly, in Chapter 5 the fully-discrete scheme is defined and numerical results comparing collision regimes are presented.

This project was supported by NSF CAREER Grant DMS-1452349. A portion of this work comes directly from the submitted paper [45].

3.1 Mathematical Framework

Before the introduction of the entropy minimization principle, we must introduce the mathematical framework used in studying the QLE. For our purposes we use a one-dimensional spatial domain, $[0, L]$. Recall, the quantum Liouville equation is given by

$$i\hbar\partial_t\varrho = [\mathcal{H}, \varrho] + i\hbar\mathcal{Q}(\varrho),$$

where the solution ϱ is a density operator, which is defined to be a positive, self-adjoint, trace class operator satisfying $\mathrm{Tr}(\varrho) = 1$. This means that we can represent ϱ in terms of its spectral elements:

$$\varrho = \sum_{p\in\mathbb{N}} \rho_p \left|\psi_p\right\rangle \left\langle\psi_p\right|,$$

where we used the Dirac bra-ket notation and $\{\rho_p, \psi_p\}$ are the p^{th} eigenvalue and eigenfunction pair of ϱ. The eigenvalues $\{\rho_p\}_{p\in\mathbb{N}}$ of ϱ are such that they form a positive sequence that decreases towards zero which sums to one. The eigenfunctions $\{\psi_p(x)\}_{p\in\mathbb{N}}$ of ϱ form an orthonormal basis for $L^2[0, L]$. If you interpret the eigenfunction ψ_p as a wavefunction representing a pure state, then ϱ represents a mixed state in which ϱ has the probability $0 < \rho_p < 1$ that it is in the state ψ_p. The local particle density n_ϱ or $n[\varrho]$ associated with ϱ is defined by

$$n_\varrho(x) = n[\varrho](x) := \sum_{p\in\mathbb{N}} \rho_p|\psi_p(x)|^2.$$

Note that we interchange the use of the local density notation between $n[\varrho]$ or n_ϱ depending on notational convenience. The local density can also be defined via duality in terms of the trace of ϱ:

$$(n_\varrho, \varphi) := \int_{[0,L]} n_\varrho\varphi dx = \mathrm{Tr}(\varrho\varphi), \tag{3.5}$$

for all smooth functions φ.

In the QLE, (3.1), we take the Hamiltonian operator $\mathcal{H}$ to be defined as

$$\mathcal{H} = \mathcal{H}_0 - e\mathcal{V}^{\text{ext}} - e\mathcal{V}, \text{ with } \mathcal{H}_0 = -\frac{\hbar^2}{2m^*}\Delta, \tag{3.6}$$

where $\Delta = \frac{d^2}{dx^2}$, m^* is the effective mass of the electron which is assumed to be constant here, and $-e$ is the electron charge. In $\mathcal{H}$ the term $\mathcal{V}^{\text{ext}} \in L^\infty(0, L)$ is an externally applied potential, and $\mathcal{V}$ is the electrostatic potential. We also call $\mathcal{V}$ the Poisson potential because it is the solution of the Poisson equation:

$$\epsilon_0 \Delta \mathcal{V} = n_\varrho, \quad \mathcal{V}(0) = \mathcal{V}(L) = 0. \tag{3.7}$$

The constant ϵ_0 is the permittivity of the material. We equip the Hamiltonians with Neumann boundary conditions and define the operators on the following domain

$$D(\mathcal{H}) = D(\mathcal{H}_0) = \left\{ \phi \in H^2(0, L) : \frac{d}{dx}\phi(0) = \frac{d}{dx}\phi(L) = 0 \right\}. \tag{3.8}$$

Then, for example, if $\varphi(x) \in L^2(0, L)$ the modified Hamiltonian $\mathcal{H}_0 + \varphi$ is bounded from below and has compact resolvent [46]. The space $H^2(0, L)$ is the Sobolev space given by $\psi(x) \in L^2(0, L)$ whose weak derivatives up to the second order are also functions in $L^2(0, L)$. The Neumann boundary conditions fix the total number of particles in the domain, and ensures there is no particle current present at the boundary. We model the inflow of particles using an initial condition formed by superposition of wave packets located away from the boundary. A more physically realistic way of modeling the inflow of particles is through the use of transparent or open boundary conditions [47, 48]. However, the choice of Neumann boundary conditions ensures that the density n_ϱ is strictly positive over the domain, which is a crucial assumption in the established theory for this problem [46, 49, 50].

Lastly, we introduce some additional functional spaces that will be useful for the convergence analysis of the semi-discrete splitting scheme for QLE in Section 4.2. Let $A \in \mathcal{L}(L^2)$ and let

$\{\varphi_n\}_{n=1}^{\infty}$ be an orthonormal basis of L^2. Then the trace of A is defined as

$$\mathrm{Tr}(A) = \sum_{n=1}^{\infty} (\varphi_n, A\varphi_n),$$

where the quantity $\mathrm{Tr}(A)$ is independent of the chosen orthonormal basis. We say a bounded operator A is trace class if and only if $\mathrm{Tr}\,|A| < \infty$ where $|A| = \sqrt{A^*A}$ and A^* is the adjoint operator [51]. The space of all trace class operators on $L^2(0, L)$ is denoted by $\mathcal{J}_1$ and the norm is given by

$$\|A\|_{\mathcal{J}_1} = \mathrm{Tr}\,|A|, \text{ with } |A| = \sqrt{A^*A}. \tag{3.9}$$

Related, the space $\mathcal{J}_2$ is the space of Hilbert-Schmidt operators on $L^2(0, L)$ with the norm

$$\|A\|_{\mathcal{J}_2} = \left(\mathrm{Tr}(A^*A)\right)^{1/2}. \tag{3.10}$$

The space $\mathcal{H}$ is defined as a subspace of trace-class operators:

$$\mathcal{H} = \left\{ \varrho \in \mathcal{J}_1, \text{ such that } \overline{\mathcal{H}_0|\varrho|\mathcal{H}_0} \in \mathcal{J}_1 \right\}, \tag{3.11}$$

where $\overline{\mathcal{H}_0|\varrho|\mathcal{H}_0}$ denotes the extension of $\mathcal{H}_0|\varrho|\mathcal{H}_0$ to $L^2(0, L)$ whose norm is given by

$$\|\varrho\|_{\mathcal{H}} = \mathrm{Tr}\,|\varrho| + \mathrm{Tr}\left(\overline{\mathcal{H}_0|\varrho|\mathcal{H}_0}\right). \tag{3.12}$$

Lastly, we introduce the space $\mathcal{E}$

$$\mathcal{E} = \left\{ \varrho \in \mathcal{J}_1, \text{ such that } \overline{\sqrt{\mathcal{H}_0}|\varrho|\sqrt{\mathcal{H}_0}} \in \mathcal{J}_1 \right\}, \tag{3.13}$$

with the norm

$$\|\varrho\|_{\mathcal{E}} = \mathrm{Tr}\,|\varrho| + \mathrm{Tr}\left(\overline{\sqrt{\mathcal{H}_0}|\varrho|\sqrt{\mathcal{H}_0}}\right). \tag{3.14}$$

For convenience we will drop the bar denoting the operator extension. The space $\mathcal{E}_+$ is the space of positive operators in $\mathcal{E}$.

Note that one-dimensional models are relevant in the study of quantum heterostructures, such as RTDs. Here, we are assuming that the different semiconductor materials are stacked in layers in the x-direction. The electrons in the conduction band see changes in the potential along x, while the variations are small in the transverse plane. One could then compute the transport properties in the bulk of the material by imposing periodic boundary conditions in the transverse plane.

Next, we turn our attention to a review of the moment closure procedure via entropy minimization and its use in the derivation of quantum hydrodynamic models.

3.2 A Review of Quantum Hydrodynamics and the Entropy Principle

In this section, we present a review of Degond and Ringhofer's theory on the entropy principle and its use in closing quantum moment systems of equations. The key feature in the closure of the quantum moment systems is the definition of a local quantum equilibrium operator and we illustrate this by an example with the quantum hydrodynamic moments. In Section 3.3.1, we take the collision operator in the QLE to be of BGK-type which involves a quantum equilibrium operator. Understanding the quantum entropy principle is essential for the definition of the collision operator as the equilibrium operator that appears in the operator is defined via a moment problem.

For this presentation of the entropy principle, we will take the Hamiltonian operator to simply be $\mathcal{H} = -\mathcal{H}_0 + V(t,x)$, where V is a bounded potential which could be the externally applied potential in (3.6), but, for now, we will ignore the effects of the Poisson potential to simplify the discussion. We will also take $x \in \mathbb{R}^d$ for the purposes of reviewing the derivation of quantum hydrodynamic models via the moment closure procedure. The material in this section is a review of the *theory of Degond and Ringhofer*, which can be found in the articles [1, 40, 43, 52].

We begin by defining what it means to be a (local) moment of ϱ and, to do so, it is convenient to work with the Wigner transform, $f_w(x,p,t)$, of ϱ. The function f_w is called the Wigner function.

As in the kinetic case, the first moment of f_w yields the local particle density, the second moment is the current density, and so on. Working with the Wigner function not only allows us to define the local moments of ϱ, but we can parallel the classical development of the moment closure procedure in [41]. In the classical setting, Levermore uses a nonperturbative approach to derive fluid macroscopic models from the kinetic model given by the Boltzmann equation. In particular, the hierarchy of moment equations is closed by defining a local equilibrium distribution function obtained from minimizing the systems entropy under moment constraints. Degond and Ringhofer transposed this approach to the quantum setting to derive quantum fluid models.

For the review of the the entropy principle we take the collision operator in (3.1) to be a general collision operator, and we need the operator to satisfy only a couple of properties. First, the first few local moments of ϱ are conserved by the collision operator, and second, the collision operator must dissipate the quantum entropy. These collision operator properties are discussed in more detail in Section 3.2.1.

The Wigner transform of ϱ is given by:

$$f_w(x,p,t) = W[\varrho](x,p,t) = \int \rho\left(x - \frac{\eta}{2}, x + \frac{\eta}{2}\right) e^{\frac{i\eta\dot{p}}{\hbar}} d\eta, \tag{3.15}$$

which is function of position and momentum and one can compare this to the distribution function that solves the collisional Boltzmann equation in the classical case. We say that f_w is the symbol of ϱ. In (3.15) the function $\rho(x,y)$ is the integral kernel of ϱ, i.e. for $\phi \in L^2(0,L)$,

$$\varrho\phi = \int \rho(x,x')\phi(x')dx',$$

which can also be used to define the local particle density as $n[\varrho](x) = \rho(x,x)$. The inverse Wigner transformation is given by the Weyl quantization/transform:

$$W^{-1}(f)\phi = Op(f)\phi = \frac{1}{(2\pi)^d} \int f\left(\frac{x+y}{2}, \hbar k\right) \phi(y) e^{ik(x-y)} dk dy, \tag{3.16}$$

which defines an operator from the real-valued symbol $f(x,p)$ which acts on $\phi \in L^2$. It is known that the Wigner and Weyl transforms, W and W^{-1}, form an isometry between the space of Hilbert-Schmidt operators $\mathcal{J}^2$ and $L^2(\mathbb{R}^d)$, meaning,

$$\mathrm{Tr}(\varrho\sigma^*) = \frac{1}{(2\pi\hbar)^d}\int W[\varrho](x,p)\overline{W[\sigma]}(x,p)dxdp. \tag{3.17}$$

Using this, we find that

$$\mathrm{Tr}(\varrho\, Op(a)) = \frac{1}{(2\pi\hbar)^d}\int a(x,p)f_w(x,p)dxdp, \tag{3.18}$$

which will be useful when we use the density operator formulation of the entropy minimization problem in Section 3.2.1. The Wigner function (3.15) solves the collisional Wigner-Boltzmann equation

$$\partial_t f_w + \nabla_x \cdot \left(\frac{1}{m^*} p f_w\right) - \Theta[V]f_w = Q_w(f_w). \tag{3.19}$$

The operator $\Theta[V]$ acts on the symbol f_w and is related to the potential V in the following way:

$$\Theta[V]f_w = \frac{-i}{(2\pi)^d\hbar}\int\left(V\left(x+\frac{\hbar\eta}{2}\right) - V\left(x-\frac{\hbar\eta}{2}\right)\right) f_w(x,p)e^{i\eta\dot{(}p-q)}dqd\eta.$$

Using the Wigner function formulation (3.15), we can define the moments of ϱ in terms of f_w analogously to the classical case. Let $\kappa(p) = \{\kappa_j(p)\}_{j=0,\dots,M}$ be a vector of monomials in p with $\kappa_0(p) = 1$ to enforce the normalization of ϱ. The (local) quantum moments of ϱ are defined as:

$$m_j[\varrho](x) = \frac{1}{(2\pi\hbar)^d}\int \kappa_j(p)f_w(x,p,t)dpdt, \quad j = 0,1,\dots,M, \tag{3.20}$$

and we write the collection of moments as $m[\varrho] = (m_j[\varrho])_{i=0}^M$. This definition of the quantum moments can be viewed as a sort-of duality relationship between the moments of ϱ and the moments of the Wigner distribution function f_w. For example, if we only consider the first moment with $\kappa_0(p) = 1$, then $m_0[\varrho] = n(x)$, which is the local density of ϱ. The local moments (3.20) can be

written in terms of the trace of ϱ using (3.18),

$$m_j[\varrho](x) = \mathrm{Tr}\big\{\varrho W^{-1}(\kappa_j(p)\delta(y-x))\big\}.$$

A set of equations for the moments of ϱ can be derived by taking the moments of the Wigner-Boltzmann equation (3.19):

$$\frac{\partial m_i}{\partial t} + \int \kappa_i(p)\left\{\nabla_x \cdot (\frac{1}{m^*}pf_w) - \Theta(V)f_w\right\}dp = \int \kappa(p)\mathcal{Q}_w(f_w)dp. \tag{3.21}$$

If the collision operator conserves the moments being considered, then the right-hand-side of (3.21) will be zero, but in general, it can be non-zero. However, for our purposes, we will assume $\mathcal{Q}(\varrho)$ conserves the moments defined by $\kappa(p)$. We can obtain a density operator formulation of the moment equations by taking the moments of the QLE (3.1). Let $\lambda(x) \in \mathbb{R}^{M+1}$ be a vector-valued test function. Then the density operator formulation of (3.21) is given by:

$$\frac{\partial}{\partial t}\int m[\varrho(t)](x)\cdot\lambda(x)dx = \mathrm{Tr}\left[\left(\left[-\frac{i}{\hbar}\mathcal{H},\varrho\right] + \mathcal{Q}(\varrho)\right)Op(\kappa(p)\cdot\lambda(x))\right], \tag{3.22}$$

which can be thought of as a weak formulation of the moment equations.

In general, it is difficult to close any given set of the quantum moment equations due to the fact the higher-order moments do not only depend on the lower order moments. This is the same issue faced by the moment equations in the classical case. The difficulty resides in the integral terms in (3.21) or, equivalently, the right-hand side of (3.22). To illustrate this moment closure problem, consider the following example where we look at the moment equations for the hydrodynamic moments of ϱ: local density, momentum, and energy.

Example 1 (Closure Problem)**.** *For this example, we take $V = 0$, so $\mathcal{H} = \mathcal{H}_0 = -\frac{1}{2m^*}\Delta$.*

The hydrodynamic moments of ϱ correspond with the momentum monomials:

$$\kappa(p) = \left\{1, p, \frac{|p|^2}{2m^*}\right\}$$

where $p \in \mathbb{R}^d$. *Then* $m[\varrho(t)] = \{n, nu, W\}$, *where* n *is the local density,* nu *is the momentum density, and* W *is the energy density. Using the definition of quantum moments* (3.21) *we have:*

$$\begin{pmatrix} n \\ nu \\ W \end{pmatrix} = \frac{1}{(2\pi\hbar)^2} \int f_w \begin{pmatrix} 1 \\ p \\ \frac{|p|^2}{2m^*} \end{pmatrix} dp.$$

These moments satisfy the moment equations (3.21)*, using the fact that the collision operator conserves the hydrodynamic moments, we find the following moment equations:*

$$\partial_t n + \nabla \cdot (nu) = 0, \tag{3.23}$$

$$\partial_t (nu) + \nabla \cdot \Pi = 0, \tag{3.24}$$

$$\partial_t W + \nabla \cdot \Phi = 0. \tag{3.25}$$

Above, Π *is the pressure tensor and* Φ *is the energy flux, and they are given by:*

$$\Pi = \frac{1}{(2\pi\hbar)^d} \int f_w (p \otimes p)\, dp, \text{ and} \tag{3.26}$$

$$\Phi = \frac{1}{(2\pi\hbar)^d} \int f_w \frac{|p|^2}{2(m^*)^2} p\, dp. \tag{3.27}$$

Note that the local density moment equation (3.23) *is already written in a closed form. However, the issue lies in the pressure tensor and energy flux which cannot be represented in terms of* n*,* nu*, and* W *without any further work. This means that the quantum hydrodynamic moment system consisting of* (3.23)*,* (3.24)*, and* (3.25) *is not closed.*

As shown by the example, we see that without any additional work the evolution equations for the hydrodynamic moments of ϱ are not written in a closed form. To remedy this moment closure problem, Degond and Ringhofer define a local quantum equilibrium operator that is obtained from the quantum entropy minimization principle which is introduced next. This quantum equilibrium

operator is then used to close the integral terms, i.e. the pressure tensor and energy flux in the example.

3.2.1 Quantum Entropy Minimization Principle

In this section, the quantum entropy minimization principle is introduced, which is the key ingredient to the quantum moment closure procedure. Recall, we are taking the quantum Liouville equation to have a general collision operator, $\mathcal{Q}(\varrho)$, such that $\mathcal{Q}$ conserves local moments and dissipates quantum entropy. Mathematically these two properties are stated as follows:

1. *Conservation of local moments.* Let $\kappa(p)$ be a list of momentum monomials, then

$$\int \mathcal{Q}_w(f_w)(x,p)\kappa_i(p)dp = 0, \text{ for } i = 0, 1, \cdots M, \forall x, \tag{3.28}$$

   where $\mathcal{Q}_w(f_w)$ is the Wigner transform of $\mathcal{Q}(\varrho)$;

2. *Entropy dissipation.* Let $g(x) = x(\log(x) - 1)$, then the *quantum Boltzmann entropy*, $G[\varrho]$, is given by

$$G[\varrho] = \mathrm{Tr}(g(\varrho)) = \mathrm{Tr}(\varrho(\log(\varrho) - 1)) = \sum_{p\in\mathbb{N}} \rho_p(\log(\rho_p) - 1), \tag{3.29}$$

   where $(\rho_p)_{p=1}^{\infty}$ are the eigenvalues of ϱ.

   The collision operator $\mathcal{Q}$ dissipates the quantum entropy, i.e.,

$$\mathrm{Tr}(\mathcal{Q}(\varrho)g'(\varrho)) = \mathrm{Tr}(\mathcal{Q}(\varrho)\log(\varrho)) \leq 0. \tag{3.30}$$

Note that in the definition of the quantum Boltzmann entropy, we take the mathematical sign convention to represent the entropy as a convex function, as opposed to the physical convention which utilizes the concave representation of entropy. Thus, we consider a minimization of the convex entropy which is completely equivalent to the physical interpretation of maximizing the

concave entropy. After defining the equilibrium density operator in the BGK-collision operator, we will confirm that (3.2) satisfies properties (3.28) and (3.30) in Section 3.3.1.

We now discuss the entropy minimization principle and how it leads to closure in the moment equations. The *entropy minimization principle* is stated as: given a set of moments $m = (m_j(x))_{j=0}^M$, *minimize the entropy* $G[\varrho]$ subject to the constraint that

$$m[\varrho] = \frac{1}{(2\pi\hbar)^d} \int f_w(x,p)\kappa(p)dp = m(x) \quad \text{for all } x \in \mathbb{R}. \tag{3.31}$$

In other words, the minimizer of the entropy will have its first $M+1$ moments given by $m(x)$. Note that the local moments of ϱ are most naturally defined in terms of the Wigner function, $f_w = W[\varrho]$, and, on the other hand, the quantum entropy is naturally represented in terms of density operator ϱ. To make sense of this discrepancy in the entropy minimization principle, we will naturally take advantage of the Wigner and Weyl (or inverse Wigner) transforms. These transformations are nonlocal transformations, so the entropy minimization problem must be treated globally (in space). This is the non-local nature in the quantum setting is another key difference between the quantum and classical cases. We will see that the solution to the constrained entropy minimization problem gives rise to the quantum equilibrium operator which is the tool that allows us to close the moment equations.

To proceed, we will dualize the moment constraint (3.31) by representing it in terms of the trace and the density operator. To begin, take a test function $\lambda(x) = (\lambda_j(x))_{j=0}^M$, multiply (3.31) on the right by $\lambda(x)$ and integrate both sides. This yields

$$\frac{1}{(2\pi\hbar)^d} \int f_w(x,p)\kappa_p \cdot \lambda(x)dxdp = \int m(x) \cdot \lambda(x)dx,$$

and use (3.18) to represent this in terms of the trace:

$$\mathrm{Tr}\left(\varrho\, \mathrm{Op}[\kappa(p) \cdot \lambda(x)]\right) = \int m(x) \cdot \lambda dx. \tag{3.32}$$

For simplicity, let $K_\lambda(\varrho) = \mathrm{Tr}\left(\varrho\, \mathrm{Op}[\kappa(p)\cdot\lambda(x)]\right)$. Using the dualized representation of the moment constraints, we can re-state the entropy minimization principle as follows: Given a set of moments $m(x) = (m_j(x))_{j=0}^M$, solve

$$\min\left\{G[\varrho] = \mathrm{Tr}(\varrho(\log\varrho - 1)) \mid K_\lambda(\varrho) = \int m(x)\cdot\lambda dx, \quad \forall\lambda(x) = (\lambda_j(x))_{j=0}^M\right\} \tag{3.33}$$

where $K_\lambda(\varrho)$ is the dualized moment definition of ϱ in (3.32).

To solve the minimization problem and to confirm that $G[\varrho]$ is indeed convex we need the first and second Gâteaux derivatives of the entropy. The following two Lemmas give the required derivatives of entropy.

Lemma 3.1 (Lemma 3.3 in [1])**.** *Suppose that $G[\varrho] = \mathrm{Tr}(\varrho\log\varrho - \varrho)$ is defined on the space of trace class positive self-adjoint operators ϱ. Then G is Gâteaux differentiable and its Gâteaux derivative $\delta G/\delta\varrho$ is given by*

$$\frac{\delta G}{\delta\varrho}\delta\varrho = \sum_{p=1}^{\infty}\log(\rho_p)\delta\varrho_{pp} = \mathrm{Tr}(\log(\varrho)\delta\varrho), \tag{3.34}$$

where ρ_p are the eigenvalues of ϱ, and $\delta\varrho_{pp}$ are the diagonal values of the perturbation operator $\delta\varrho$ in the basis of the eigenfunctions ψ_p of ϱ.

Lemma 3.2 (Lemma 3.4 in [1])**.** *$G[\varrho]$ is strictly convex and is twice Gâteaux differentiable,*

$$\frac{\delta^2 G}{\delta\varrho^2}(\delta\varrho,\delta\varrho) = \sum_{p,q}\frac{\log(\rho_p)-\log(\rho_q)}{\rho_p-\rho_q}|\delta\varrho_{pq}|^2. \tag{3.35}$$

When $\rho_p = \rho_q$, the quotient is taken to be $\frac{1}{\rho_p}$ by L'Hôpital's rule. The perturbation operator $\delta\varrho$ is assumed to be Hermitian.

The constrained minimization problem in (3.33) can be re-cast as an unconstrained minimization problem using standard Lagrange Multiplier theory. In this case, the Lagrangian is given by

$$\mathcal{L}_m(\varrho, \lambda) = G[\varrho] - \left(K_\lambda(\varrho) - \int m(x) \cdot \lambda(x) dx \right),$$

where the test function λ plays the roll of the Lagrange multiplier. If we denote the minimizer of (3.33) by ϱ_{eq}^{λ}, then we have

$$G[\varrho_{eq}^{\lambda}] = \min_{\varrho} \max_{\lambda} \mathcal{L}_m(\varrho, \lambda) = \max_{\lambda} \min_{\varrho} \mathcal{L}_m(\varrho, \lambda). \tag{3.36}$$

Standard optimization theory tells us that at the minimum, ϱ_{eq}^{λ} the Gâteaux derivative $\delta\mathcal{L}_m/\delta\varrho$ should vanish. The definition of the Gâteaux derivative of the entropy in (3.34) allows us to compute where $\delta\mathcal{L}_m/\delta\varrho$ vanishes. This gives us the following condition:

$$\mathrm{Tr}(\log(\varrho)\delta\varrho) = \mathrm{Tr}(\delta\varrho \, \mathrm{Op}[\kappa(p) \cdot \lambda(x)]), \tag{3.37}$$

which is equivalent to

$$\log(\varrho) = \mathrm{Op}[\kappa(p) \cdot \lambda(x)].$$

The form of the minimizer, ϱ_{eq}^{λ}, can be deduced from this relationship and it is given in the following lemma.

Lemma 3.3 (Lemma 3.5 in [1], [53])**.** *The necessary condition for extremality for the unconstrained minimization problem $\mathcal{L}_m(\varrho_{eq}^{\lambda}) = min_{\varrho}\mathcal{L}_m(\varrho, \lambda)$ implies the minimizer must have the following form:*

$$\varrho_{eq}^{\lambda} = \exp\left(Op(\lambda \cdot \kappa)\right). \tag{3.38}$$

The minimizer, ϱ_{eq}^{λ}, is called the quantum equilibrium density operator associated with Lagrange multiplier $\lambda(x)$ or, simply, a quantum Maxwellian. Since we now know the minimizer must take on the form of a quantum Maxwellian, the entropy minimization problem (3.36) can be

reduced to simply a maximization over λ:

$$G(\varrho_{eq}^{\mu_m}) = \mathcal{L}_m(\varrho_{eq}^{\mu_m}, \mu_m) = \max_\lambda \mathcal{L}_m(\varrho_{eq}^{\lambda}, \lambda), \tag{3.39}$$

where $\mu_m(x)$ denotes the particular set of Lagrange multipliers that solves the above maximization problem. Note that the identification of ϱ_{eq}^{λ} as the candidate equilibrium operator, we are effectively now optimizing the fluid entropy which is defined in terms of the moments:

$$\begin{aligned} S(m) = G[\varrho_{eq}^{\lambda}] &= \mathrm{Tr}(\exp(\mathbf{Op}(\lambda \cdot \kappa))\,(\mathbf{Op}(\lambda \cdot \kappa) - 1)) \\ &= \frac{1}{(2\pi\hbar)^d} \int W[\exp(\mathbf{Op}(\lambda \cdot \kappa))](\lambda \cdot \kappa - 1) dx dp. \end{aligned}$$

The appropriate choice for λ is found by the optimization problem in (3.39). The moments of ϱ_{eq}^{λ} are known and can be expressed as

$$m[\lambda] := \frac{1}{(2\pi\hbar)^d} \int W[\exp(\mathbf{Op}(\lambda \cdot \kappa))] \kappa dp = m.$$

Now the fluid entropy can be written explicitly as a function of the moments m:

$$S(m) = \int \lambda \cdot m \; dx - \Sigma(\lambda),$$

where

$$\Sigma(\lambda) = \frac{1}{(2\pi\hbar)^d} \int W[\exp(\mathbf{Op}(\lambda \cdot \kappa))] dp dx.$$

In [43], the following inversion formula for the mapping $\lambda \mapsto m$ is proved:

$$\frac{\delta S}{\delta m} = \lambda, \quad \frac{\delta \Sigma}{\delta \lambda} = m.$$

The above derivatives are Gâteaux derivatives. Then we find λ from the following optimization problem:

$$\max_\lambda \left\{ S(m) = \int \lambda \cdot m \, dx - \Sigma(\lambda) \right\} = \min_\lambda \left\{ -S(m) = \Sigma(\lambda) - \int \lambda \cdot m \, dx \right\}$$

The function $\Sigma(\lambda)$ is proved to be convex in [1], and so we use the minimization convention above to take advantage of the convexity.

In this section we have reviewed the quantum entropy minimization principle and how the minimization problem gives rise to the quantum equilibrium density operator or quantum Maxwellian. In the next section we will use this quantum Maxwellian to achieve closure in the moment equations.

3.2.2 Moment Equation Closure

We return to the moment equation closure problem and show that the quantum Maxwellian (3.38) is the essential ingredient in the closure process. For simplicity, we drop the superscript λ in the quantum Maxwellian notation and simply write ϱ_{eq} to denote the equilibrium density operator. We can now close the moment equation (3.21) and (3.22) by replacing ϱ with ϱ_{eq}. To work with the Wigner function definition of moments, we take the Wigner transformation of ϱ_{eq} and denote it by $f_w^e = W[\varrho_{eq}]$. Then the moment equations are closed (3.21) as follows:

$$\frac{\partial m_i}{\partial t} + \int \kappa_i(p) \left\{ \nabla_x \cdot \left(\frac{1}{m^*} p f_w^e \right) - \Theta[V] f_w^e \right\} dp = 0, \tag{3.40}$$

where we have used (3.28), the fact that $\mathcal{Q}$ conserves the moments defined by $\kappa(p)$. Recall that $(m_j[\varrho_{eq}])_{j=0}^M = (m_j(x))_{j=0}^M$, so the first term above is unchanged compared to (3.21). The replacement of f_w by f_w^e allows us to close the integral terms in (3.21) since f_w^e is known. The density operator formulation of the moment equations, (3.22), are closed in the same way:

$$\frac{\partial}{\partial t} \int m[\varrho_e(t)](x) \cdot \lambda(x) dx = \mathrm{Tr} \left[\left(\left[-\frac{i}{\hbar} \mathcal{H}, \varrho \right] \right) Op(\kappa(p) \cdot \lambda(x)) \right]. \tag{3.41}$$

The two forms of the closed moment equations are called the strong and weak formulations, respectively, of the Quantum Moment Models. For a given set of moment equations, the entropy minimization principle gives us a non-local mapping between the “conservative" variables (the moments m) and the “entropic" variables (the Lagrange multiplier λ). This is a key element of the derivation of quantum moment models via the entropy principle.

We now return to the example of the quantum Hydrodynamic moment equations.

Example 2 (Closing Quantum Moment Equations [1, 40])**.** *In the previous example, we found the following set of unclosed moment equations for the hydrodynamic moments,* (3.23)*,* (3.24)*,* (3.25)*:*

$$\partial_t n + \nabla \cdot (nu) = 0,$$
$$\partial_t (nu) + \nabla \cdot \Pi = 0,$$
$$\partial_t W + \nabla \cdot \Phi = 0.$$

Recall that the pressure tensor Π *and the energy flux* Φ *need to be written in terms of the moments,* n*,* nu*, and* W*, in order to be represented in a closed form. For this example, we take* $\lambda(x) = \left\{ \frac{A(x)}{C(x)}, \frac{B(x)}{C(x)}, -\frac{1}{C(x)} \right\}$ *where* $A(x)$ *and* $C(x)$ *are scalar-valued functions and* $B(x)$ *is a vector-valued function.* $A(x)$ *is the generalized chemical potential,* $B(x)$ *is the generalized mean velocity, and* $C(x)$ *is the generalized temperature. The equilibrium density operator,* ϱ_{eq}*, found through the constrained minimization of the free energy has the form [1]:*

$$\varrho_{eq} = \exp\left(W^{-1}(\kappa(p) \cdot \lambda)\right) = \exp\left(W^{-1}\left(\frac{1}{C(x)}\left(A(x) + B(x) \cdot p - \frac{|p|^2}{2m^*}\right)\right)\right)$$
$$= \exp(-H(A, B, C)) := \varrho_{eq}^{(n,nu,W)},$$

where $H(A, B, C)$ *is a modified Hamiltonian that depends on the Lagrange parameters:*

$$H(A,B,C) = W^{-1}\left(\frac{1}{C(x)}\left(A(x) + B(x)\cdot p - \frac{|p|^2}{2m^*}\right)\right)$$
$$= \frac{\hbar^2}{2m}\nabla\cdot\left(\frac{1}{C}\nabla\right) - \frac{i\hbar}{2}\left(\nabla\cdot\frac{B}{C} + \frac{B}{C}\cdot\nabla\right) + \left(\frac{A}{C} + \frac{1}{4}\frac{\hbar^2}{2m^*}\Delta\frac{1}{C}\right)$$

Note, the equilibrium operator ϱ_{eq} cannot be explicitly represented with respect to the hydrodynamic moments, but instead the thermodynamic variables (A,B,C) are used. The non-local mapping between the variables (A,B,C) and the moment variables lies in the moment equation of the equilibrium operator:

$$\begin{pmatrix} n \\ nu \\ W \end{pmatrix} = \frac{1}{(2\pi\hbar)^d}\int f_w^e \begin{pmatrix} 1 \\ p \\ \frac{|p|^2}{2m^*} \end{pmatrix} dp,$$

where $f_w^e = W[\varrho_{eq}^{(n,nu,W)}]$. This provides the non-local mapping because (A,B,C) are such that the first three moments of $\varrho_{eq}^{(n,nu,W)} = \exp(-H(A,B,C))$ are equal to n, nu, and W.

Finally, the moment equations can be closed using the Wigner transform of the equilibrium operator, f_w^e, in place of f_w in the pressure tensor (3.26) *and energy flux* (3.27)*. Which yields:*

$$\Pi = \frac{1}{(2\pi\hbar)^d}\int f_w^e (p\otimes p)\, dp, \text{ and}$$
$$\Phi = \frac{1}{(2\pi\hbar)^d}\int f_w^e \frac{|p|^2}{2(m^*)^2} p\, dp.$$

This substitution closes the pressure tensor and energy flux expressions because $f_w^e = W[\varrho_e^{(n,nu,W)}]$ implicitly depends on the moments (n,nu,W). Replacing Π and Ψ in the moment equations with the closed versions yields the Quantum Hydrodynamic Model.

In this section, we have introduced Degond and Ringhofer's quantum moment equation closure procedure based on the entropy minimization principle. We have seen in this example for the quantum hydrodynamic moment equations that the quantum equilibrium density operator allows us to close these moment equations. Having the ability to close a set of quantum moment equations

gives rise to a hierarchy of Quantum Moment Models, one of which is the quantum hydrodynamic model reviewed here. A class of quantum diffusion models can also be derived from the entropy minimization principle, only you start with the assumption that the temperature of the system is fixed and so the energy is no longer conserved. One of these models, the quantum drift diffusion model, will be discussed later as it will be used in the numerical comparisons presented at the end of the chapter. We now turn our attention back to the quantum Liouville equation equipped with the BGK-collision operator and define this operator using the entropy minimization principle.

3.3 Definitions for the Quantum Liouville-BGK Equation

We now turn our attention to the quantum Liouville equation equipped with the BGK-collision operator. In the review of Degond and Ringhofer's theory in the previous section we worked with a general collision operator that satisfied two conditions: the conservation of moments and dissipation of quantum entropy. However, now that the entropy principle has been introduced we now have the ability to appropriately define the BGK-collision operator that we use in the QLE. Recall the QLE is given by,

$$i\hbar\partial_t \varrho = [\mathcal{H}, \varrho] + i\hbar\mathcal{Q}(\varrho),$$

and we take the collision operator, $\mathcal{Q}(\varrho)$, to be of BGK-type [42], i.e.

$$\mathcal{Q}(\varrho) = \frac{1}{\tau}(\varrho_{\mathrm{e}}[\varrho] - \varrho). \tag{3.42}$$

Above τ is a given relaxation time and $\varrho_e[\varrho]$ is a quantum statistical equilibrium operator found via an entropy minimization principle. As in the previous section, this equilibrium operator is also called a quantum Maxwellian. We now assume that the temperature of the system T_0 is held constant which requires a slight modification in statement of the entropy minimization principle used to find the equilibrium operator. In this setting, rather than working with entropy, we want to minimize the free energy (entropy + kinetic energy) of the system, which is actually a relative entropy. Next, we consider the entropy (free energy) minimization principle that allows us to define

the BGK-collision operator. After we have properly defined the equilibrium operator for quantum Liovuille-BGK equation, we will re-scale the QLE for development of the numerical scheme in Chapter 4.

3.3.1 Local Equilibrium Density Operator, $\varrho_e[\varrho]$

In the previous sections, we followed Degond and Ringhofer's construction of the quantum moment closure procedure. In that process we were able to define the local quantum equilibrium operator ϱ_e as the minimizer of an appropriate functional. In this setting, the equilibrium operator, $\varrho_e[\varrho]$, is defined by minimizing the quantum free energy of the system, which is given by,

$$\mathcal{F}(\varrho) = k_B T_0 \operatorname{Tr}\left(\varrho\left(\log\varrho - 1 + \frac{\mathcal{H}}{T_0 k_B}\right)\right). \tag{3.43}$$

Here the Hamiltonian is defined as $\mathcal{H} = -\frac{\hbar}{2m^*}\Delta + \mathcal{V}(x) = Op\left(\frac{|p|^2}{2m^*} + V\right)$.

In particular, the local equilibrium operator is obtained from minimizing the quantum free energy, (3.43), under the constraint that the local density of $\varrho_e[\varrho](t,x)$ is given by the local density of the solution $\varrho(t,x)$. Let $n(x)$ represent the local density of particles associated with ϱ, i.e. $n(x) = n[\varrho]$. Then in the moment problem, the vector of momentum monomials is reduced to simply $\kappa(p) = \kappa_0(p) = 1$ and the list of corresponding moments is simply $m(x) = m_0(x) = n(x)$. Using Lagrange multipliers, we find $\varrho_e[\varrho]$ is the minimizer of the following optimization problem

$$\mathcal{F}(\varrho_e) = \min_{\varrho}\max_{\lambda}\mathcal{L}_m(\varrho,\lambda) = \max_{\lambda}\mathcal{L}_m(\varrho_e^{\lambda},\lambda) = \max_{\lambda}\Big(\mathcal{F}(\varrho_e^{\lambda}) - \int \lambda n[\varrho_e]dx + \int n(x)\lambda dx\Big).$$

As before, the minimizer of the free energy, the equilibrium operator, has the form of a quantum Maxwellian, [40]:

$$\varrho_e^{\lambda} = \exp(-\mathcal{H}/k_B T_0 + \lambda).$$

We utilize the definition of this quantum Maxwellian to reduce the optimization problem to simply a maximization over λ:

$$\mathcal{F}(\varrho_e) = \max_\lambda \left(-k_B T_0 Tr(e^{-\mathcal{H}/k_B T_0 + \lambda(x)}) - \int n(x)\lambda(x) \right)$$

The corresponding Lagrange multiplier is $\lambda = -\mathcal{A}/k_B T_0$, where $\mathcal{A}[\varrho]$ is the quantum chemical potential associated with ϱ, inspired by the classical case. The negative is for notational convenience. With this identification, we can rewrite the maximization of $\mathcal{L}_m$ over λ as a minimization of $-\mathcal{L}_m$ over A, i.e.

$$\mathcal{F}(\varrho_e[\varrho]) = \min_A \Big(T_0 k_B \operatorname{Tr}\big(e^{-(\mathcal{H}+A)/k_B T_0}\big) + \int n(x) A dx \Big), \tag{3.44}$$

where $n(x) = n[\varrho]$. Denote the minimizer of (3.44) by $\mathcal{A}[\varrho]$ and this chemical potential is such that the local density constraint is satisfied. Thus, the equilibrium density operator in the BGK-type collision operator is given by the following *quantum Maxwellian*:

$$\begin{aligned} &\varrho_e[\varrho] = \exp(-(\mathcal{H} + \mathcal{A}[\varrho])/k_B T_0) \\ &\text{where } \mathcal{A}[\varrho] = \min_A \mathcal{J}(A), \end{aligned} \tag{3.45}$$

and we set

$$\mathcal{J}(A) = k_B T_0 \operatorname{Tr}\left(e^{-(\mathcal{H}+A)/k_B T_0}\right) + \int n(x) A dx. \tag{3.46}$$

The fact the equilibrium operator takes on the form of a quantum Maxwellian in this setting is rigorously proved in [49]. By computing the gradient of $\mathcal{J}(A)$,

$$\nabla_A \mathcal{J}(A) = n(x) - n[e^{-(\mathcal{H}_0 + A)}], \tag{3.47}$$

we can immediately see that the original local density constraint, $n[e^{-(\mathcal{H}_0+A)}] = n[\varrho]$, is recovered when $\nabla_A \mathcal{J}(A) = 0$. As with the density operators, we can represent the quantum Maxwellian in

terms of the spectral elements $(\lambda_p[\mathcal{A}], \phi_p[\mathcal{A}])_{p\in\mathbb{N}}$ of the Hamiltonian $\mathcal{H}_\mathcal{A} = \mathcal{H} + \mathcal{A}[\varrho]$, so we have

$$\varrho_{\mathrm{e}}[\varrho] = \sum_{p\in\mathbb{N}} e^{-\lambda_p[\mathcal{A}]/k_B T_0} \left|\phi_p[\mathcal{A}]\right\rangle \left\langle\phi_p[\mathcal{A}]\right| .$$

Now that all terms of the BGK-collision operator are understood, we can check the two properties that we assume the collision operators will have. The first item to check is whether or not $\mathcal{Q}(\varrho)$ conserves the local particle density. This is an easy property to check given our understanding of the equilibrium density operator, $\varrho_e[\varrho]$, which is constructed such that the local density of $\varrho_e[\varrho]$ is equivalent to the local density of ϱ, i.e.

$$n[\varrho] = n(x) = n[\varrho_e[\varrho]].$$

We can then see that $n[\mathcal{Q}[\varrho]] = \frac{1}{\tau}\left(n[\varrho_e[\varrho]] - n[\varrho]\right) = 0$, meaning, the collision operator conserves the local density. The second condition, which requires the collision operator to dissipate the free energy is proved in [53].

Here we have applied the entropy minimization principle presented in Section 3.2.1 to define the equilibrium operator that is involved in the definition of the BGK-collision operator. Next, we will nondimensionalize the quantum Liouville equation equipped with the BGK-collision operator in preparation for development of the numerical scheme.

3.3.2 Scaling the Quantum Liouville Equation

Now that the quantum Liouville-BGK equation has been fully defined, we turn our attention to re-scaling the model. In Chapter 4, a Strang splitting scheme is developed for the scaled QLE model. Following the scaling used in [44], we nondimensionalize the quantum Liouville equation in a manner that incorporates the relevant physical constants. The characteristic length will be determined by the size of the device, $\bar{x} = L$, the reference time is given by $\bar{t} = \frac{L^2 e}{\mu k_B T_0}$ where μ is the mobility of the material, and voltages are scaled with respect to the thermal potential $\bar{V} = \frac{k_B T_0}{e}$. Using these reference values, we can now define the following dimensionless quantities:

$$x' = \frac{x}{\bar{x}}, \quad n' = \frac{n}{\bar{n}}, \quad t' = \frac{t}{\bar{t}}, \quad \mathcal{V}' = \frac{\mathcal{V}}{\bar{V}}, \quad \mathcal{A}' = \frac{\mathcal{A}}{\bar{V}}, \tag{3.48}$$

to obtain the scaled QLE coupled with the Poisson equation (omitting the primes):

$$\begin{aligned} i\varepsilon\partial_t \varrho &= \frac{1}{\sqrt{2}\beta}[\mathcal{H}, \varrho] + \frac{i}{\varepsilon}(\varrho_{\mathrm{e}}[\varrho] - \varrho), \quad x \in [0,1] \\ \alpha^2 \Delta \mathcal{V} &= n_\varrho, \quad \mathcal{V}(0) = \mathcal{V}(1) = 0. \end{aligned} \tag{3.49}$$

Above, the Hamiltonian is given by

$$\mathcal{H} = -\beta^2\Delta - \mathcal{V} - \mathcal{V}^{\text{ext}} = \mathcal{H}_0 - \mathcal{V} - \mathcal{V}^{\text{ext}},$$

where $\mathcal{H}_0 = -\beta^2\Delta$ is the free Hamiltonian. The scaled equilibrium operator, ϱ_e, is given by

$$\varrho_{\mathrm{e}}[\varrho] = e^{-(\mathcal{H}_0 + \mathcal{A}[\varrho])} = \sum_{p\in\mathbb{N}} e^{-\lambda_p[\mathcal{A}]} \left|\varphi_p[\mathcal{A}]\right\rangle \left\langle\varphi_p[\mathcal{A}]\right|,$$

where $(\lambda_p[\mathcal{A}], \varphi_p[\mathcal{A}])$ are the spectral elements of the Hamiltonian $\mathcal{H}[\mathcal{A}] = \mathcal{H}_0 + \mathcal{A}[\varrho]$. The chemical potential $\mathcal{A}[\varrho]$ is found by minimizing the functional

$$\mathcal{J}(A) = \mathrm{Tr}\left(e^{-(\mathcal{H}+A)}\right) + \int n(x)A dx,$$

which is equivalent to minimizing the free energy of the system under a local density constraint. The dimensionless constants in the scaled QLE-Poisson system are given by

$$\alpha = \sqrt{\frac{\epsilon_0 k_B T_0}{e^2 L^2 \bar{n}}} = \frac{\lambda_{\mathrm{d}}}{L}, \quad \beta = \sqrt{\frac{\hbar^2}{2m^* L^2 k_B T_0}} = \frac{\lambda_{\mathrm{dB}}}{L}, \quad \varepsilon = \sqrt{\frac{k_B T_0 \tau^2}{m^* L^2}} = \frac{\lambda_{\mathrm{mfp}}}{L}, \tag{3.50}$$

where λ_{d} is the Debye length, λ_{dB} is the de Broglie length, and λ_{mfp} is the mean free path. For example, if we take temperature $T_0 = 300$ K, characteristic length $L = 100$ nm, mobility $\mu = 0.85\ \mathrm{m^2 V s^{-1}}$, permittivity $\epsilon_0 = 11.44 * (8.854\,187 \times 10^{-12})$ F/m, and effective mass $m^* = 0.067m$

where m is the mass of an electron in kg. Then, the dimensionless constants take on the values $\alpha = 0.825$, $\beta = 0.0313$, and $\varepsilon = 0.5623$.

In this chapter, we began with a formal introduction to the quantum Liouville equation and the relevant mathematical framework with which we are working. To fully understand the collision operator we are using, it was necessary to review Degond and Ringhofer's theory on the quantum entropy minimization principle and the closure of quantum moment equations. This theory introduced the concept of a quantum equilibrium operator which is the minimizer of the entropy (or free energy) under a moment constraint. We then utilized the entropy minimization principle to define the BGK-collision operator which we are using to model particle collisions in the numerical scheme. Finally, we concluded with the nondimensionalization of the quantum Liouville-BGK equation in preparation for the development of a numerical scheme. We now turn our attention to the semi-discrete in time numerical scheme defined for the scaled quantum Liouville-BGK equation.

Chapter 4

Semi-Discrete Numerical Scheme for Quantum Liouville-BGK Equation

This chapter focuses on the properties of a Strang splitting scheme for the scaled quantum Liouville equation. In defining a numerical scheme for the QLE, the nonlinear collision operator causes the most difficulty. However, the issue with the nonlinearity is circumvented by using a splitting scheme to essentially separate the two physical phenomena of transport and collision. We will see that the resolution of the collision-portion of the QLE relies heavily on the minimization of the quantum free energy under a local density constraint. We first analyze the numerical scheme as semi-discrete in time and in the next chapter the fully-discrete scheme is given with numerical results. We show that the Strang spitting scheme is convergent in-time with a sub-optimal order of convergence (less than order 2) due to the fact that the nonlinearity in the collision operator is known to only be Hölder continuous and not Lipschitz continuous. However, we show through numerical convergence analysis that the fully-discrete scheme is indeed order-two in time, despite the limitations in the theoretical results. The fully-discrete numerical scheme is given in Chapter 5 along with numerical results.

4.1 A Strang Splitting Scheme for Quantum Liouville Equation

We now develop a numerical scheme for the scaled quantum Liouville-BGK equation coupled with the Poisson equation, (3.49),

$$i\varepsilon\partial_t\varrho = \frac{1}{\sqrt{2}\beta}[\mathcal{H},\varrho] + \frac{i}{\varepsilon}(\varrho_{\mathrm{e}}[\varrho]-\varrho), \quad x\in[0,1] \tag{4.1}$$

$$\alpha^2\Delta\mathcal{V} = n_\varrho, \quad \mathcal{V}(0)=\mathcal{V}(1)=0. \tag{4.2}$$

Recall, the Hamiltonian is $\mathcal{H} = -\beta^2\Delta - \mathcal{V} - \mathcal{V}^{\text{ext}} = \mathcal{H}_0 - \mathcal{V} - \mathcal{V}^{\text{ext}}$ and both $\mathcal{H}_0$ and $\mathcal{H}$ are equipped with Neumann boundary conditions. The splitting scheme is developed on a semi-discrete version of (4.1)-(4.2) as this formulation will provide the framework for the forthcoming convergence analysis of the scheme. In the previous chapter, we found the equilibrium operator in the collision operator is defined by a quantum Maxwellian, $\varrho_{\text{e}}[\varrho] = \exp(-(\mathcal{H} + \mathcal{A}))$, where the chemical potential $\mathcal{A}$ is obtained from minimizing (3.46). In general, the numerical resolution of the quantum Liouville equation is not trivial due the nonlinearity in the collision operator, namely, the equilibrium operator depends on the solution to the QLE at any given time. The computational difficulties introduced by the nonlinear collision operator can be circumvented through the use of a Strang splitting scheme [31, 32]. In the splitting scheme, the transport term $[\mathcal{H}, \varrho]$ is treated separately from the collision term $\mathcal{Q}(\varrho)$. In treating the collision term separately from the transport term, we can utilize the fact that $\mathcal{Q}(\varrho)$ preserves the density n_ϱ which allows us to treat the collision subproblem in the splitting scheme as locally linear. To see this, the density operator $\varrho(t)$ that satisfies

$$\varepsilon\partial_t\varrho = \frac{1}{\varepsilon}\mathcal{Q}(\varrho), \quad \varrho(t_0) = \sigma$$

is such that $n_{\varrho(t)} = n_\sigma$ for all $t \geq t_0$. So in this subproblem, the collision operator takes on the form

$$\mathcal{Q}(\varrho) = \frac{1}{\varepsilon}(\varrho_{\text{e}}[\sigma] - \varrho),$$

which is now linear in ϱ. The treatment of the transport term and further details regarding the splitting scheme for the quantum Liouville equation are in the next section.

As noted, the difficulty in the resolution of QLE is the calculation of the nonlinear equilibrium operator $\varrho_e[\varrho]$ in the collision term. To see how this problem is simplified greatly by using a splitting approach, we begin by writing:

$$i\varepsilon\partial_t\varrho = \mathcal{L}(\varrho) + i\mathcal{Q}(\varrho) := \frac{1}{\sqrt{2}\beta}[\mathcal{H}, \varrho] + \frac{i}{\varepsilon}(\varrho_{\text{e}}[\varrho] - \varrho).$$

We then define two subproblems by splitting the operator on the right-hand-side into a "Hamiltonian" or transport part, $\mathcal{L}(\varrho)$, and a collision part, $\mathcal{Q}(\varrho)$. The collision subproblem by

$$i\varepsilon\partial_t\varrho_1 = \frac{i}{\varepsilon}(\varrho_e[\varrho_1] - \varrho_1) = i\mathcal{Q}(\varrho_1), \quad \varrho_1(t=0) = \varrho_1^0, \tag{4.3}$$

and the transport subproblem is given by

$$i\varepsilon\partial_t\varrho_2 = \frac{1}{\sqrt{2}\beta}[\mathcal{H}, \varrho_2] = \mathcal{L}(\varrho_2), \quad \varrho_2(t=0) = \varrho_2^0. \tag{4.4}$$

Note that both problems are nonlinear because of the Poisson potential in $\mathcal{H}$, but the latter is not difficult to handle compared to $\varrho_e[\varrho]$, and this is why it is included in the Hamiltonian part. The decomposition $\mathcal{L}(\varrho) + iQ(\varrho)$ can be seen in spirit as a decomposition into two different physical effects: transport and collision.

The solution to each subproblem can formally be represented in terms of an exponential operator

$$\varrho_1(t) = e^{t\mathcal{Q}}\varrho_1^0 =: W(t)\varrho_0^1, \quad \text{and } \varrho_2(t) = e^{t\mathcal{L}}\varrho_2^0 =: U(t)\varrho_2^0,$$

respectively. Let $t_k = kh$ for $k = 0, 1, \ldots, N_T$. For a given initial condition ϱ^0, and $t \in (0, h]$ where h is the time-step, the semi-discrete Strang solution at time $t + t_{k-1}$, denoted $\varrho_s(t + t_{k-1})$, is then obtained from the solution at t_{k-1} by

$$\varrho_s(t + t_{k-1}) = U(t/2)W(t)U(t/2)\varrho_s^{k-1}, \qquad t \in (0, h], \qquad \varrho_s^0 = \varrho^0, \tag{4.5}$$

with $\varrho_s^{k-1} = \varrho_s(t_{k-1})$ and $\varrho_s^k = \varrho_s(h + t_{k-1})$. Next we take a closer look at the properties of each subproblem that allow us to formulate the splitting scheme. We first do this in the semi-discrete setting.

4.1.1 Collision Subproblem

We now discuss the time-discrete formulation of the collision subproblem. The crucial observation here is that the collision subproblem (4.3) preserves the local density: indeed, by construction of the equilibrium $\varrho_e[\varrho_1]$, we have $n[\varrho_e] = n[\varrho_1]$, and as a consequence, by linearity of the trace,

$$i\varepsilon\partial_t n[\varrho_1] = n[i\mathcal{Q}(\varrho_1)] = \frac{i}{\varepsilon}(n[\varrho_e[\varrho_1]] - n[\varrho_1]) = 0. \tag{4.6}$$

The collision subproblem then becomes a simple linear equation,

$$i\varepsilon\partial_t\varrho = \frac{i}{\varepsilon}(\varrho_e[\varrho_1^0] - \varrho_1), \quad \varrho_1(t=0) = \varrho_1^0. \tag{4.7}$$

Suppose $\varrho(t)$ and the equilibrium operator $\varrho_{\mathrm{e}}[\varrho_1^0]$ have the following spectral representations:

$$\varrho(t) = \sum_{p=1}^{\infty} \rho_p(t) \left|\psi_p\right\rangle \left\langle\psi_p\right| \quad \text{and} \quad \varrho_{\mathrm{e}}[\varrho_1^0] = \sum_{p=1}^{\infty} e^{-\lambda_p[\mathcal{A}_0]} \left|\varphi_p[\mathcal{A}_0]\right\rangle \left\langle\varphi_p[\mathcal{A}_0]\right|,$$

where $\varrho(t=0) = \varrho_0^1$. In the equilibrium operator $\varrho_{\mathrm{e}}[\varrho_0^1]$, $(\lambda_p[\mathcal{A}_0], \varphi_p[\mathcal{A}_0])$ for $p \in \mathbb{N}$ represent the eigenvalues and eigenfunctions for the Hamiltonian $\mathcal{H}_{\mathcal{A}_0} = \mathcal{H} + \mathcal{A}_0$ where $\mathcal{A}_0$ is the chemical potential obtained from minimizing the free energy. The collision subproblem has a solution given by

$$\varrho_1(t) = e^{-t/\varepsilon^2}\varrho_1^0 + (1 - e^{-t/\varepsilon^2})\varrho_{\mathrm{e}}[\varrho_1^0].$$

Thus, we see that finding the appropriate chemical potential $\mathcal{A}_0$ is where the bulk of the work lies. For each collision step, we are given some initial operator ϱ_0^1 and we must first find the associated equilibrium operator that satisfies the local density moment constraint, which will then allow us to update $\varrho_1(t)$ using the above solution. Recall, the chemical potential $\mathcal{A}_0$ is found by solving the unconstrained minimization:

$$\min_A \mathcal{J}(A) = \min_A \left(\mathrm{Tr}\left(e^{-(\mathcal{H}+A)}\right) + \int n[\varrho_1^0] A dx \right), \tag{4.8}$$

where $n[\varrho_1^0]$ is the local density corresponding to the initial operator ϱ_1^0. We will implement the minimization of the free energy using nonlinear conjugate gradient which is detailed in Chapter 5. Next we look at the formulation of the semi-discrete transport subproblem.

4.1.2 Transport Subproblem

As with the collision subproblem, the transport subproblem, (4.4), is simplified by utilizing the spectral representation of ϱ. Recall, the transport subproblem is given by

$$i\varepsilon\partial_t\varrho_2 = \frac{1}{\sqrt{2}\beta}[\mathcal{H}, \varrho_2], \quad \varrho_2(t=0) = \varrho_2^0, \tag{4.9}$$

for $\mathcal{H} = -\beta^2\Delta - \mathcal{V}^{\text{ext}} - \mathcal{V}$ where $\mathcal{V}$ is the electrostatic potential that solves the Poisson equation (4.2). Suppose the initial operator is given by $\varrho_2^0 = \sum \gamma_p \left|v_p\right\rangle \left\langle v_p\right|$. Then the solution to (4.4) can be written as

$$\varrho_2(t) = \sum_{p=1}^{\infty} \gamma_p \left|v_p(t)\right\rangle \left\langle v_p(t)\right|.$$

Above, for each p, the eigenfunction, $v_p(t)$, satisfies the following Schrödinger equation:

$$\begin{aligned} i\varepsilon\frac{\partial v_p(t)}{\partial t} &= \frac{1}{\sqrt{2}\beta}\mathcal{H}v_p(t) \\ &= \frac{1}{\sqrt{2}\beta}(-\beta^2\Delta - \mathcal{V}^{\text{ext}})v_p(t) - \frac{1}{\sqrt{2}\beta}\mathcal{V}v_p(t). \end{aligned}$$

To solve each Schrödinger equation to update the eigenfunctions, we will implement a secondary splitting scheme to handle the nonlinearity in the Poisson potential. In this splitting scheme, the Poisson potential term is treated separately from the term with the Hamiltonian $-\beta^2\Delta + \mathcal{V}^{\text{ext}}$. The solution to the Poisson potential term can be obtained exactly using the definition of the Poisson potential, (4.2). This is detailed in Chapter 5.

We now turn our attention the the convergence analysis of the Strang splitting scheme.

4.2 Convergence Analysis of Strang Splitting

In this section, we focus on convergence analysis of the semi-discrete in time splitting scheme. To make use of some of the established theory for the quantum Liouville-BGK equation, we will prove the convergence result without any potentials, i.e. $\mathcal{V}^{\text{ext}} = 0$, and we consider QLE without the Poisson equation for the electrostatic potential. In other words, the two Hamiltonians we have are equal, $\mathcal{H} = \mathcal{H}_0$. Since we are only interested in convergence properties of the splitting scheme and not the asymptotic properties as $\varepsilon \to 0$, we set $\varepsilon = 1$ to simplify notation in the proof. Note that the constant C in the estimate of the convergence theorem would depend on ε and it grows as ε approaches 0. Again, for simplicity, we restrict the spatial domain to the unit interval $[0, 1]$.

We will use the functional spaces defined in the mathematical framework section. In particular, we will need to use the $\mathcal{J}_1$-norm on trace-class operators in (3.9) and the $\mathcal{J}_2$-norm on Hilbert-Schmidt operators in (3.10). Additionally, we will need the subspaces of trace-class operators $\mathcal{H}$ defined in (3.11) with norm (3.12) and $\mathcal{E}$ defined in (3.13) with norm (3.14).

It is well known that for linear equations, a Strang splitting scheme is convergent and second-order in time. In general for nonlinear equations a Strang splitting scheme can still attain the second-order in time property, but it is dependent on the nonlinearity being Lipshitz continuous, see for example [54, 55]. In our case, the equilibrium operator $\varrho_{\text{e}}[\varrho]$ is Hölder continous nonlinear operator and *not* Lipshitz continuous, so we cannot prove that the splitting scheme for the QLE is second-order in time. In [50], it is proved that the mapping $\varrho \mapsto \varrho_{\text{e}}[\varrho]$ is Hölder continuous, which is given by the following lemma.

Lemma 4.1 (Corollary 5.8 in [50])**.** *Let ϱ_1 and ϱ_2 be two density operators in $\mathcal{H}$. Let $M_0 \in (0, \infty)$ be such that*

$$\|\varrho_1\|_{\mathcal{H}} + \|\varrho_2\|_{\mathcal{H}} \leq M_0, \ \textit{and} \ M_0^{-1} \leq n[\varrho_i], \ \forall\, x \in [0, 1], \ i = 1, 2.$$

Then,

$$\|\varrho_e[\varrho_1] - \varrho_e[\varrho_2]\|_{\mathcal{J}_2} \leq C\|\varrho_1 - \varrho_2\|_{\mathcal{J}_2}^{1/8},$$

where C is independent of ϱ_1 and ϱ_2.

The regularity of the mapping $\varrho \mapsto \varrho_{\mathrm{e}}[\varrho]$ in Lemma 4.1 is non-optimal, but the Hölder regularity will be sufficient for the purpose of showing the splitting scheme converges. Clearly since the regularity of the nonlinearity is non-optimal (i.e. not Lipshitz continuous), the convergence result for the splitting scheme is non-optimal. Note that we are considering Hölder regularity as non-optimal since the we prove that the Strang splitting is convergent but it is not second-order in time. The problem of proving the optimal regularity for $\varrho \mapsto \varrho_{\mathrm{e}}[\varrho]$ is still an open problem.

The strategy to prove convergence of the splitting scheme is to compare (in $\mathcal{J}_2$ norm) the difference between the actual solution $\varrho(t)$ of the QLE to the splitting solution $\varrho_s(t)$. We recall the existence result for the solution of the QLE, $\varrho(t)$, proved in [50], which utilizes the free-Schrödinger operator with no potentials.

Theorem 4.2 ([50])**.** *Suppose that the initial density operator $\varrho^0 \in \mathcal{H}$ is such that $\varrho^0 = f(\mathcal{H}_0) + \delta\varrho$, $f(\mathcal{H}_0) \in \mathcal{E}_+$, $\delta\varrho$ is self-adjoint in $\mathcal{E}$, and that there exists $\underline{n} > 0$ such that*

$$n[f(\mathcal{H}_0)](x) \geq \underline{n} \text{ and } \|\delta\varrho\|_{\mathcal{E}} \leq \underline{n}/4.$$

Then, for any $T > 0$, the quantum Liouville-BGK equation admits a solution ϱ in $C^0([0,T],\mathcal{H}) \cap C^1([0,T],\mathcal{J}_1)$ satisfying the integral equation

$$\varrho(t) = e^{-t}U(t)\varrho^0 + \int_0^t e^{-(t-s)}U(t-s)\varrho_e[\varrho(s)]ds. \tag{4.10}$$

Moreover, the density verifies

$$n[\varrho(t)](x) \geq e^{-T}\underline{n}/2, \quad \forall (t,x) \in [0,T] \times [0,1].$$

Above, the evolution operator $U(t)$ gives us the solution to the free-transport (or the free-Schrödinger) part of the QLE. Note that in Theorem 4.2, the lower bounds on the densities $n[f(\mathcal{H}_0)]$ and $n[\varrho(t)]$ are crucial to ensure the existence and uniqueness of the equilibrium operator that min-

imizes the quantum free energy under local density constraint which is proved in [49]. We use the integral solution of the QLE (4.10) to compute bounds on the local error with the splitting solution. The above theorem only supplies us the *existence* of a solution to the QLE, and does not provide uniqueness. We note that, even though this existence result and the other results of [50] are stated for the free Schrödinger operator, we believe the results can be adapted to include the external and Poisson potentials, but this is out of the scope of this work. As a result, we believe the convergence result for the splitting scheme can be extended to include the potentials, provided the key results in [50] can be extended.

To compare the splitting solution, $\varrho_s(t)$, to the original solution, (4.10), we must establish an integral solution for $\varrho_s(t)$. We use the fact that the solution to the collision subproblem, (4.7), $\varrho_1(t) = W(t)\sigma$, where σ is the initial density operator for the collision part. We have the following integral solution to the collision subproblem:

$$\varrho_1(t) = W(t)\sigma = e^{-t}\sigma + \int_0^t e^{-(t-s)}\varrho_{\mathrm{e}}[\sigma]ds. \tag{4.11}$$

Given a final time T and $0 < h \leq 1$, we denote by N_T the largest integer such that $N_T h \leq T$. Further, denote by ϱ_s^k and ϱ^k the splitting solution and exact solution at time $t_k = kh$, respectively. Thus, by using (4.5) with the integral solution to the collision subproblem, we have, for $t \in [0, h]$,

$$\varrho_s(t_k + t) = U(t/2)W(t)U(t/2)\varrho_s^k = e^{-t}U(t)\varrho_s^k + \int_0^t e^{-(t-u)}U(t/2)\varrho_{\mathrm{e}}[U(t/2)\varrho_s^k]du, \tag{4.12}$$

and, for the exact solution,

$$\varrho(t_k + t) = e^{-t}U(t)\varrho^k + \int_0^t e^{-(t-s)}U(t-s)\varrho_{\mathrm{e}}[\varrho(t_k + s)]ds. \tag{4.13}$$

For $t \in [0, h]$, let the local error of the splitting solution be denoted by

$$e_k(t) := \varrho(t_k + t) - \varrho_s(t_k + t),$$

where ϱ is *any* solution to the integral equation (4.10). Also note that $e_{k+1} = e_k(h)$. The convergence result first requires that we prove uniform bounds on the splitting solution ϱ_s in the $\mathcal{H}$-norm to ensure that the splitting solution is well-defined and bounded in $\mathcal{H}$. This result is given in the following Lemma.

Lemma 4.3. *Under the assumptions of Theorem 4.2 on $\varrho^0 \in \mathcal{H}$, the splitting scheme admits a unique positive solution in $\mathcal{H}$ with the following bound*

$$\left\|\varrho_s^k\right\|_{\mathcal{H}} \leq e^{Ckh}\left\|\varrho^0\right\|_{\mathcal{H}}, \tag{4.14}$$

where C is a constant independent of k and h. Furthermore, the splitting scheme preserves the trace, i.e.

$$\left\|\varrho_s^k\right\|_{\mathcal{J}_1} = \left\|\varrho^0\right\|_{\mathcal{J}_1}, \quad \forall\, k \geq 0, \tag{4.15}$$

and the local density $n[U(\tau)\varrho_s^k]$ verifies

$$n[U(\tau)\varrho_s^k] \geq e^{-T}\underline{n}/2, \quad \forall\, \tau \geq 0. \tag{4.16}$$

In order to prove that the scheme converges, we must first prove a *local* convergence result on the local error $e_k(t)$.

Lemma 4.4. *Under the condition of Theorem 4.2, the local error e_k between a solution to* (4.10) *and the splitting solution* (4.12) *satisfies, for each k and all $t \in [0, h]$,*

$$\|e_k(t)\|_{\mathcal{J}_2} \leq \|e_k\|_{\mathcal{J}_2} + C\left(h^{\frac{1}{1-\gamma}} + h^{1+\gamma} + h^2\right),$$

where $\gamma = 1/8$ is the Hölder regularity constant of the mapping $\varrho \mapsto \varrho_e[\varrho]$ and the constant C is independent of h and k.

Lemma 4.14 is proved in Section 4.2.2 and Lemma 4.4 is proved in Section 4.2.3. Iterating the local estimate of Lemma 4.4, we arrive at the following convergence result.

Theorem 4.5. *Under the condition of Theorem 4.2 on $\varrho^0 \in \mathcal{H}$, we have, for any solution ϱ to the integral equation* (4.10)*,*

$$\left\|\varrho^{N_T} - \varrho_s^{N_T}\right\|_{\mathcal{J}_2} \leq C\left(h^{\frac{\gamma}{1-\gamma}} + h^{\gamma} + h\right), \tag{4.17}$$

where $\gamma = 1/8$, the constant C is independent of h, and ϱ_s is the splitting solution.

Indeed, according to the local error estimate in Lemma 4.4,

$$\left\|\varrho^{N_T} - \varrho_s^{N_T}\right\|_{\mathcal{J}_2} \leq \left\|e_{N_T-1}\right\|_{\mathcal{J}_2} + \widehat{C}\left(h^{\frac{1}{1-\gamma}} + h^{1+\gamma} + h^2\right),$$

and iterating yields the desired estimate

$$\left\|\varrho^{N_T} - \varrho_s^{N_T}\right\|_{\mathcal{J}_2} \leq \widetilde{C}\left(h^{\frac{1}{1-\gamma}} + h^{1+\gamma} + h^2\right) N_T \leq C\left(h^{\frac{\gamma}{1-\gamma}} + h^{\gamma} + h\right).$$

This means that the unique splitting solution is close to any solution of the QLE for small h. As noted before, the error estimate in Theorem 4.5 is not optimal. If the map $\varrho \mapsto \varrho_{\mathrm{e}}[\varrho]$ is indeed Lipschitz, then we can show that the Splitting scheme for QLE has the expected second-order global error. We believe this mapping is Lipschitz but we cannot prove this yet. Despite this, numerical results indicate the global convergence is of order 2, which is shown in Section 4.2.1.

As a consequence of Theorem 4.5, the uniqueness of solutions to the continuous QLE can be proved. Recall, the result in Theorem 4.2 only provided existence of a solution to the QLE and not uniqueness. To see how Theorem 4.5 leads to uniqueness, we fix some time $t > 0$ and $t > h > 0$, and let $t = N_t h + r_h$ with $N_t \in \mathbb{N}$ and $r_h \in [0, 1)$. Let ϱ_1 and ϱ_2 be two possible solutions to (4.10). The associated splitting solution ϱ_s is unique and according to Theorem 4.5 and Lemma 4.4, we have

$$\left\|\varrho_j(t) - \varrho_s(t)\right\|_{\mathcal{J}_2} = o(h), \quad j = 1, 2.$$

Hence, we have

$$\begin{aligned}\|\varrho_1(t) - \varrho_2(t)\|_{\mathcal{J}_2} &= \|\varrho_1(t) - \varrho_s(t) + \varrho_s(t) - \varrho_2(t)\|_{\mathcal{J}_2} \\ &\leq \|\varrho_1(t) - \varrho_s(t)\|_{\mathcal{J}_2} + \|\varrho_s(t) - \varrho_2\|_{\mathcal{J}_2} = o(h).\end{aligned}$$

In the above inequality, both t and h are arbitrary, thus, $\varrho_1 = \varrho_2$ for all t. Typically, uniqueness for nonlinear PDEs is obtained under a Lipschitz condition on the nonlinearity, which is not available here. Uniqueness in this case is a consequence of three factors: (i) the minimizer $\varrho_{\mathrm{e}}[\varrho]$ is unique for a given ϱ, yielding a unique splitting solution; (ii) the equation for the collision part of the splitting scheme becomes locally linear; and (iii) the Hölder regularity of the map $\varrho \mapsto \varrho_{\mathrm{e}}[\varrho]$.

Thus, because the exact solution is now unique, we conclude from Theorem 4.5 that the solution of the splitting scheme converges to the unique solution of (4.10). Next, we show that the numerical order of convergence for the splitting scheme is indeed second order, despite the non-optimal result in Theorem 4.5.

4.2.1 Numerical Order of Convergence

To illustrate the order of convergence in the fully discrete scheme we take an initial condition given by a Gaussian wave packet (see (5.26) in Section 5.3) centered at $x_0 = 0.5$. We set $\varepsilon = 1$, $V^{\text{ext}} = 0$, and take a final time $T = 0.1$. However, we still incorporate the effects of the Poisson potential in this example. Numerically, we find that the Strang splitting scheme for the QLE is *second order* in time, see Table 4.1. The numerical order of convergence, p_{num} is approximated by the following, [54]:

$$p_{\text{num}} = \max_{t_k \in [0,T]} \frac{1}{\ln 2} \ln \left(\frac{\left\| n_{h/2} - n_h \right\|_{L_1}}{\left\| n_{h/4} - n_{h/2} \right\|_{L_1}} \right), \tag{4.18}$$

where $t_k = hk$ and n_h indicates the local density associated with split solution ϱ_s^k computed with time-step h. As the value of ε decreases, from the theoretical convergence analysis, we expect the local error to grow. When $\varepsilon = 0.1$ we find the splitting scheme is still approximately second order in time with $p_{\text{num}} = 1.976$ with $h = 1 \times 10^{-3}$ and $p_{\text{num}} = 1.994$ with $h = 5 \times 10^{-4}$. Note that as

ε decreases we need to decrease the size of the time step, h, to maintain the accuracy attained for $\varepsilon = 1$. This is shown by the smaller values of p_{num} we found when ε is 0.1.

h	$N = 401$	$N = 201$	$N = 101$
1×10^{-3}	1.998	1.999	1.992
5×10^{-4}	2.0003	1.998	1.999

Table 4.1: Numerical order of convergence, p_{num}, for the Strang splitting scheme for the QLE, computed with $h = 1 \times 10^{-3}$ and 5×10^{-4} using (4.18) for different values of $\Delta x = 1/(N+1)$.

Another way to compute the numerical order of convergence is by computing a so-called reference solution with a very small time step. Let $h = 1 \times 10^{-3}$, then the reference solution is computed for $h_{\text{ref}} = h/32 = 3.125 \times 10^{-5}$. We approximate the splitting scheme error by computing the error between the reference solution and the numerical solutions computed a time step in $\{h, h/2, h/4, h/8, h/16\}$, which is done by

$$e_{\text{rel}} = \frac{\|n_h - n_{h_{\text{ref}}}\|_{L_1}}{\|n_{h_{\text{ref}}}\|_{L_1}}.$$

This error is computed at the final time of $T = 0.1$ and it is shown in Table 4.2. The numerical order of convergence can be approximated as the slope of the the logarithm of the error versus the logarithm of the time-steps. In this case, we find that the approximate numerical order of convergence is 2.093, see Figure 4.1.

Table 4.2: The error between the reference solution and $n[\varrho_s]$ computed at the listed time steps.

time step	e_{rel}
$h = 1 \times 10^{-3}$	5.05×10^{-5}
$h/2 = 5 \times 10^{-4}$	1.26×10^{-5}
$h/4 = 2.5 \times 10^{-4}$	3.11×10^{-6}
$h/8 = 1.25 \times 10^{-4}$	7.42×10^{-7}
$h/16 = 6.255 \times 10^{-5}$	1.4724×10^{-7}

Figure 4.1: A log-log plot of the errors and associated time steps shown in Table 4.2 where the reference solution was computed with $h_{\text{ref}} = h/32$. The slope of the line is 2.093- indicating second order convergence.

We now turn our attention to the proofs of the Lemmas that are crucial in the proof of Theorem 4.5.

4.2.2 Proof of Lemma 4.3

Recall, Lemma 4.3, requires proving three properties of the splitting solution: (4.14) is the uniform bound on the splitting solution in $\mathcal{H}$, (4.15) states the splitting solution preserves the trace, and (4.16) gives a lower bound on the local density that appears in the splitting integral solution (4.12). The lower bound in (4.16) ensures the existence and uniqueness of the splitting solution.

Given ϱ_s^k, we recall that one iteration of the splitting scheme reads

$$\varrho_s(t) = U(t/2)W(t)U(t/2)\varrho_s^k, \quad t \in [0, h],$$

where $U(t)\sigma = e^{-i\mathfrak{H}_0 t}\sigma e^{i\mathfrak{H}_0 t}$, and $\varrho_1(t) := W(t)\sigma$ is the solution to

$$\partial_t \varrho_1 = \varrho_{\text{e}}[\varrho_1] - \varrho_1. \tag{4.19}$$

We first address the *existence and uniqueness* of $\varrho_s(t)$. We prove this iteratively. First, if ϱ_s^0 is a density operator in $\mathcal{E}$, then so is $U(t/2)\varrho_s^0$ for all $t \geq 0$ since $U(t)$ preserves self-adjointness and positivity, and

$$\left\|U(t)\varrho_s^0\right\|_{\mathcal{E}} = \|\varrho_s(0)\|_{\mathcal{E}}.$$

Let $\sigma := U(h/2)\varrho_s^0$ and consider the collision subproblem $\varrho_1(t) = W(t)\sigma$. Recall that the collsion subproblem preserves the local density, which allows us to treat (4.19) as locally linear and admits a solution

$$\varrho_1(t) = (1 - e^{-t})\varrho_{\mathrm{e}}[\sigma] + e^{-t}\sigma, \tag{4.20}$$

provided $\varrho_{\mathrm{e}}[\sigma]$ exists and is unique. In [49] the question of uniqueness is addressed: when $\sigma \in \mathcal{E}$, and when $n[\sigma] > 0$ for all $x \in [0, 1]$, the corresponding equilibrium operator $\varrho_{\mathrm{e}}[\sigma] \in \mathcal{E}_+$ is unique. This result is stated as Theorem 2.1 in [49]. We know that $\sigma \in \mathcal{E}_+$ from the previous step, and need to prove the lower bound on the local density. Following the assumptions of Theorem 4.2, for any $t \geq 0$,

$$n[U(t)\varrho_s^0] = n[f(\mathcal{H}_0)] + n[U(t)\delta\varrho] \geq \underline{n} + n[U(t)\delta\varrho],$$

where we used the fact that $e^{it\mathcal{H}_0}$ commutes with $f(\mathcal{H}_0)$. Again, under the assumptions of Theorem 4.2, we have

$$\|n[U(t)\delta\varrho]\|_{L^\infty} \leq \|n[U(t)\delta\varrho]\|_{W^{1,1}} \leq 2\|U(t)\delta\varrho\|_{\mathcal{E}} = 2\|\delta\varrho\|_{\mathcal{E}} \leq \underline{n}/2.$$

This shows that $n[U(t)\varrho_s^0] > \underline{n}/2$ for all t, and therefore $\varrho_{\mathrm{e}}[\sigma]$ exists in $\mathcal{E}_+$ and is unique. Hence, ϱ_1 is well-defined, and as a consequence so is $\varrho_s^1 = \varrho_s(h)$ in $\mathcal{E}_+$. We now iterate over k. Since $\varrho_{\mathrm{e}}[U(t)\rho_s^0]$ is nonnegative, we have from (4.20), for all $\tau \geq 0$,

$$n[U(\tau)\varrho_s^1] \geq e^{-h} n[U(\tau + h)\varrho_s^0] \geq e^{-h}\underline{n}/2,$$

which allows us to construct $\varrho_{\mathrm{e}}[U(h/2)\varrho_s^1] \in \mathcal{E}_+$, and therefore ϱ_s^2. Iterating this process, we find $\varrho_s^k \in \mathcal{E}$ and, from the version of (4.20) at step k,

$$n[U(\tau)\varrho_s^k] \geq e^{-kh} n[U(\tau+h)\varrho_s^{k-1}] \geq e^{-kh} n[U(\tau+kh)\varrho_s^0] \geq e^{-kh}\underline{n}/2 \geq e^{-T}\underline{n}/2, \tag{4.21}$$

which proves the lower bound on $n[U(\tau)\varrho_s^k]$ for all k and all $\tau \geq 0$. We have therefore obtained a unique solution to the splitting scheme in $\mathcal{E}$ satisfying the state lower bound in Lemma 4.3.

Next we prove the *uniform bounds* on the splitting solution ϱ_s. We derive a bound in $\mathcal{H}$ uniform in k and h. For this, we first need uniform bounds in $\mathcal{J}_1$ and $\mathcal{E}$. The bound in $\mathcal{J}_1$ is immediate because $U(t)$ is an isometry in $\mathcal{J}_1$ and (4.19) preserves trace, therefore

$$\left\|\varrho_s^k\right\|_{\mathcal{J}_1} = \left\|\varrho_s^0\right\|_{\mathcal{J}_1}.$$

For the bound in $\mathcal{E}$, we remark that $U(t)$ is also an isometry in $\mathcal{E}$, and we have the following bound from Proposition 2.2 in [50]:

$$\|\varrho_{\mathrm{e}}[\sigma]\|_{\mathcal{E}} \leq C\left\|\sqrt{n[\sigma]}\right\|_{H^1}^2 \leq C + C\|\sigma\|_{\mathcal{E}},$$

where C is independent of σ. With the definition of ϱ_1 in (4.20), we have

$$\|\varrho_1(t)\|_{\mathcal{E}} \leq (1-e^{-t})\|\varrho_{\mathrm{e}}[\sigma]\|_{\mathcal{E}} + e^{-t}\|\sigma\|_{\mathcal{E}} \leq Ct(1+\|\sigma\|_{\mathcal{E}}) + e^{-t}\|\sigma\|_{\mathcal{E}},$$

since $1 - e^{-t} \leq t$ for $t \geq 0$. With this established bound on the solution to the collision part, we can obtain the following bound on the splitting solution ϱ_s:

$$\left\|\varrho_s^{k+1}\right\|_{\mathcal{E}} \leq Ch + Ch\left\|\varrho_s^k\right\|_{\mathcal{E}} + e^{-h}\left\|\varrho_s^k\right\|_{\mathcal{E}} \leq Ch + e^{Ch}\left\|\varrho_s^k\right\|_{\mathcal{E}}.$$

Iterating the above bound on ϱ_s^{k+1}, we find

$$\left\|\varrho_s^{N_T}\right\|_{\mathcal{E}} \leq Ch\sigma_{k=0}^{N_T-1} e^{Ckh} \left\|\varrho^0\right\|_{\mathcal{E}} \leq CTe^{CT} \left\|\varrho^0\right\|_{\mathcal{E}}, \tag{4.22}$$

which provides a uniform bound in $\mathcal{E}$ on the splitting solution.

We can now move on to the proof of the uniform bound in $\mathcal{H}$. We will need the following result from [50]: let $\sigma \in \mathcal{H}$, with $\|\sigma\|_{\mathcal{E}} \leq \alpha_0$ and $n[\sigma] \geq \alpha_1 > 0$. Then,

$$\|\varrho_{\mathrm{e}}[\sigma]\|_{\mathcal{H}} \leq C_{\alpha_0,\alpha_1} \|\sigma\|_{\mathcal{H}}. \tag{4.23}$$

We begin as we did with the $\mathcal{E}$ bound. The definition of $\varrho_1(t)$ in (4.20), yields the following bound

$$\|\varrho_1(t)\|_{\mathcal{H}} \leq (1 - e^{-t}) \|\varrho_{\mathrm{e}}[\sigma]\|_{\mathcal{H}} + e^{-t} \|\sigma\|_{\mathcal{H}} \leq Ct \|\sigma\|_{\mathcal{H}} + e^{-t} \|\sigma\|_{\mathcal{H}},$$

where the sublinear estimate in (4.23) was used in the second inequality. The constant C is independent of k and h because both the lower bound in (4.21) and $\mathcal{E}$ bound in (4.22) are uniform in h and k. Returning to the splitting solution ϱ_s, we obtain

$$\left\|\varrho_s^{k+1}\right\|_{\mathcal{H}} \leq Ch \left\|\varrho_s^k\right\|_{\mathcal{H}} + e^{-h} \left\|\varrho_s^k\right\|_{\mathcal{H}} \leq e^{Ch} \left\|\varrho_s^k\right\|_{\mathcal{H}}.$$

Iterating the above estimate, we find the required uniform bound in $\mathcal{H}$:

$$\left\|\varrho_s^k\right\|_{\mathcal{H}} \leq e^{Ckh} \left\|\varrho^0\right\|_{\mathcal{H}}.$$

This ends the proof.

4.2.3 Proof of Lemma 4.4

We prove the local error estimate which is crucial in establishing the global error result in Theorem 4.5. Before proceeding with the proof, the following generalized Gronwall Lemma will be useful. The proof of the general result can be found in [56].

Lemma 4.6 (generalized Gronwall, [56]). *Let $f : [0, T] \to \mathbb{R}$ be continuous and satisfy the inequality,*

$$f(t) \leq M + \int_0^t e^{-(t-s)}(f(s))^\gamma ds, \quad \gamma \in (0, 1),$$

where $M \geq 0$. Then, the follwing estimate holds

$$f(t) \leq \Phi^{-1}\left(\Phi(M) + 1 - e^{-t}\right),$$

where $\Phi(u) = \frac{1}{1-\gamma}u^{1-\gamma}$ and $\Phi^{-1}(w) = (1-\gamma)^{\frac{1}{1-\gamma}}w^{\frac{1}{1-\gamma}}$.

We will also need the following Lemma proved in [50] to establish the local error estimate.

Lemma 4.7 (Lemma 6.4 in [50]). *Let $\varrho \in \mathcal{H}$ be self-adjoint and nonnegative. Then,*

$$\|U(t)\varrho - \varrho\|_{\mathcal{J}_1} \leq Ct\|\varrho\|_{\mathcal{H}}, \text{ for all } t \geq 0.$$

We can now proceed with the proof. According to (4.12) and (4.13), the local error $e_k(t) = \varrho(t_k + t) - \varrho_s(t_k + t)$ for $t \in [0, h]$, with notation $e_k := e_k(0)$, we have

$$e_k(t) = e^{-t}U(t)(\varrho^k - \varrho_s^k) + \int_0^t e^{-(t-u)}\left(U(t-u)\varrho_{\mathrm{e}}[\varrho(t_k + u)] - U(t/2)\varrho_{\mathrm{e}}[U(t/2)\varrho_s^k]\right) du,$$

where $\varrho^k = \varrho(t_k)$ and $\varrho_s^k = \varrho_s(t_k)$. Taking the $\mathcal{J}_2$ norm of $e_k(t)$ and using the fact that $U(t)$ is an isometry on $\mathcal{J}_2$, we find for $t \in [0, h]$,

$$\begin{aligned}
\|e_k(t)\|_{\mathcal{J}_2} &\leq e^{-t}\left\|\varrho^k - \varrho_s^k\right\|_{\mathcal{J}_2} + \int_0^t e^{-(t-u)}\left\|U(t-u)\varrho_{\mathrm{e}}[\varrho(t_k+u)] - U(t/2)\varrho_{\mathrm{e}}[U(t/2)\varrho_s^k]\right\|_{\mathcal{J}_2} du \\
&\leq e^{-t}\|e_k\|_{\mathcal{J}_2} + \int_0^t e^{-(t-u)}\left\|U(t-u)\varrho_{\mathrm{e}}[\varrho(t_k+u)] - U(t-u)\varrho_{\mathrm{e}}[U(t/2)\varrho_s^k]\right\|_{\mathcal{J}_2} \\
&\quad + \int_0^t e^{-(t-u)}\left\|U(t-u)\varrho_{\mathrm{e}}[U(t/2)\varrho_s^k] - U(t/2)\varrho_{\mathrm{e}}[U(t/2)\varrho_s^k]\right\|_{\mathcal{J}_2} du \\
&:= e^{-t}\|e_k\|_{\mathcal{J}_2} + I_1(t) + I_2(t).
\end{aligned}$$

First, consider the integral given by I_2. Since $U(t)$ is an isometry on $\mathcal{J}_2$, we have:

$$\begin{aligned}
I_2(t) &= \int_0^t e^{-(t-u)}\left\|U(t/2-u)\varrho_{\mathrm{e}}[U(t/2)\varrho_s^k] - \varrho_{\mathrm{e}}[U(t/2)\varrho_s^k]\right\|_{\mathcal{J}_2} du \\
&\leq C\int e^{-(t-u)}|t/2-u|\left\|\varrho_{\mathrm{e}}[U(t/2)\varrho_s^k]\right\|_{\mathcal{H}} du \\
&\leq C\int_0^t e^{-(t-u)}|t/2-u|\left\|\varrho_s^k\right\|_{\mathcal{H}} du \\
&\leq Ct^2\left\|\varrho^0\right\|_{\mathcal{H}}.
\end{aligned}$$

The first inequality is thanks to Lemma 4.7 and the fact that $\mathcal{J}_{\in} \subset \mathcal{J}_1$. The second inequality is due to the sublinear estimate $\left\|\varrho_{\mathrm{e}}[U(t/2)\varrho_s^k]\right\|_{\mathcal{H}} \leq C\left\|U(t/2)\varrho_s^k\right\|_{\mathcal{H}}$ stated in (4.23), which holds provided $n[U(t/2)\varrho_s^k] \geq \alpha > 0$ and $U(t/2)\varrho_s^k$ is bounded uniformly in $\mathcal{E}$. These two facts are obtained in Lemma 4.3 as $\mathcal{H} \subset \mathcal{E}$. The last inequality is due to the estimate (4.14) in Lemma 4.3.

Next, consider the integral given by I_1. We apply Lemma 4.1 as both ϱ and $U(t/2)\varrho_s^k$ belong to $\mathcal{H}$ and their respective local densities are uniformly bounded from below according to Theorem

4.2 and Lemma 4.3. Then, with $\gamma = 1/8$, we have:

$$\begin{aligned} I_1(t) &= \int_0^t e^{-(t-u)} \big\| \varrho_{\mathrm{e}}[\varrho(t_k+u)] - \varrho_{\mathrm{e}}[U(t/2)\varrho_s^k] \big\|_{\mathcal{J}_2} \\ &\le C \int_0^t e^{-(t-u)} \big\| \varrho(t_k+u) - U(t/2)\varrho_s^k \big\|_{\mathcal{J}_2}^{\gamma} du \\ &\le C \int_0^t e^{-(t-u)} \| \varrho(t_k+u) - \varrho_s(t_k+u) \|_{\mathcal{J}_2}^{\gamma} du \\ &\quad + \int_0^t C e^{-(t-u)} \big\| \varrho_s(t_k+u) - U(t/2)\varrho_s^k \big\|_{\mathcal{J}_2}^{\gamma} du \\ &= T_1(t) + T_2(t). \end{aligned}$$

The term T_1 is handled by the Gronwall Lemma. For T_2, we remark that from (4.12) and Lemma 4.3, we have

$$\big\| \varrho_s(t_k+u) - U(u)\varrho_s^k \big\|_{\mathcal{J}_2} \le Ch, \quad \forall\, u \in [0,h].$$

Again, we have from Lemma 4.3 and Lemma 4.7, the following result: for $t \in [0,h]$,

$$\begin{aligned} T_2(t) &= \int_0^t C e^{-(t-u)} \big\| \varrho_s(t_k+u) - U(t/2)\varrho_s^k \big\|_{\mathcal{J}_2}^{\gamma} du \\ &\le Ch^{1+\gamma} + C \int_0^t e^{-(t-u)} \big\| \varrho_s^k - U(t/2-u)\varrho_s^k \big\|_{\mathcal{J}_2}^{\gamma} du \\ &\le Ch^{1+\gamma} + C \int_0^t e^{-(t-u)} |t/2-u|^{\gamma} \big\| \varrho_s^k \big\|_{\mathcal{H}}^{\gamma} du \\ &\le Ch^{1+\gamma}. \end{aligned}$$

Collecting all estimates, we have for $t \in [0,h]$,

$$\begin{aligned} \|e_k(t)\|_{\mathcal{J}_2} &\le e^{-h} \|e_k\|_{\mathcal{J}_2} + Ch^{1+\gamma} + Ch^2 + \int_0^t e^{-(t-u)} \|e_k(s)\|_{\mathcal{J}_2}^{\gamma} du \\ &:= M_{k,h} + \int_0^t e^{-(t-u)} \|e_k(s)\|_{\mathcal{J}_2}^{\gamma} du \end{aligned}$$

Finally, the using generalized Gronwall Lemma and the fact that $(x+y)^\beta \leq C_\beta(x^\beta + y^\beta)$ for $x, y \geq 0$ and $\beta \geq 1$, we find:

$$\begin{aligned}
\|e_k(t)\|_{\mathcal{J}_2} &\leq (1-\gamma)^{\frac{1}{1-\gamma}} \left(\frac{1}{1-\gamma} M_{k,h}^{1-\gamma} + 1 - e^{-t} \right)^{\frac{1}{1-\gamma}} \\
&\leq M_{k,h} + C h^{\frac{1}{1-\gamma}} = e^{-h} \|e_k\|_{\mathcal{J}_2} + C \left(h^{1+\gamma} + h^2 + h^{\frac{1}{1-\gamma}} \right) \\
&\leq \|e_k\|_{\mathcal{J}_2} + C \left(h^{1+\gamma} + h^2 + h^{\frac{1}{1-\gamma}} \right).
\end{aligned}$$

This ends the proof.

We now turn our attention to the description of the fully discrete Strang splitting scheme.

Chapter 5

Fully Discrete Numerical Scheme for Quantum Liouville Equation and Numerical Applications

In this chapter, we focus on the fully-discrete numerical scheme and applying the scheme in a numerical study of collision regimes. We begin discretizing in space the Strang splitting scheme described in Section 4.1. Thanks to the convergence result in Section 4.2 we know the splitting solution will provide us with a unique solution. After the description of the spatial discretization, we turn our attention to the quantum drift diffusion model, which is a collision-dominated model, and we review the scheme described in [46]. We will then use the Strang splitting scheme to study different collision regimes: ballistic transport, a mix of collision and transport, and collision-dominated.

5.1 Spatial Discretization of Splitting Scheme

The Strang splitting scheme for the QLE is discretized in space using the convention proposed in [46] for the quantum drift diffusion model (QDD). We choose this convention because the QDD is the model we use to represent a collision dominated regime in the numerical study of different collision regimes presented in Section 5.3. We begin by discretizing the (nondimensionalized) spatial domain $\Omega = [0, 1]$ with $N + 2$ points $x_p = p\Delta x$ for $p = 0, 1, N + 1$, and $\Delta x = 1/(N + 1)$. For a smooth function φ, integrating $\frac{1}{\Delta x}\mathcal{H}\varphi$ over the interval $[x_{p-\frac{1}{2}}, x_{p+\frac{1}{2}}]$ for $1 \leq p \leq N$ yields

$$
\begin{aligned}
&\frac{1}{\Delta x}\int_{x_{p-\frac{1}{2}}}^{x_{p+\frac{1}{2}}} \mathcal{H}\varphi(x)dx \\
&\quad = -\frac{\beta^2}{\Delta x}\left(\varphi'\left(x_{p+\frac{1}{2}}\right) - \varphi'\left(x_{p-\frac{1}{2}}\right)\right) - \frac{1}{\Delta x}\int_{x_{p-\frac{1}{2}}}^{x_{p+\frac{1}{2}}} (\mathcal{V} + \mathcal{V}^{\text{ext}})(x)\varphi(x)dx \\
&\quad = -\frac{\beta^2}{\Delta x}\left(\varphi(x_{p+1}) - 2\varphi(x_p) + \varphi(x_{p-1})\right) - (\mathcal{V} + \mathcal{V}^{\text{ext}})(x_p)\varphi(x_p) + O(\Delta x^2).
\end{aligned}
$$

The midpoint rule was used for the potential integral above. Note that the external potential $\mathcal{V}^{\text{ext}}$ is often chosen to represent a double potential barrier, which includes jumps at the barriers. This means we must be careful with discretizing $\mathcal{V}^{\text{ext}}$ and we must ensure that the jumps occur at the midpoints $x_{p+\frac{1}{2}}$ and not in the interior $(x_{p-\frac{1}{2}}, x_{p+\frac{1}{2}})$. We adopt a first order discretization of the Neumann boundary conditions, resulting in $\varphi(x_0) = \varphi(x_1)$ and $\varphi(x_N) = \varphi(x_{N+1})$. This yields the following discrete $N \times N$ Neumann Laplace operator

$$\Delta_{\text{Neu}} = \frac{1}{\Delta x^2} \begin{bmatrix} -1 & 1 & 0 & \cdots & 0 \\ 1 & -2 & 1 & \cdots & 0 \\ \vdots & \ddots & \ddots & & \vdots \\ 0 & \cdots & 1 & -2 & 1 \\ 0 & \cdots & \cdots & 1 & -1 \end{bmatrix}.$$

By using the first-order approximation at the boundaries, the overall order of the spatial scheme is only one. The discrete Dirichlet Laplace operator used in the calculation of the Poisson potential is given by:

$$\Delta_{\text{Dir}} = \frac{1}{\Delta x^2} \begin{bmatrix} -2 & 1 & 0 & \cdots & 0 \\ 1 & -2 & 1 & \cdots & 0 \\ \vdots & \ddots & \ddots & & \vdots \\ 0 & \cdots & 1 & -2 & 1 \\ 0 & \cdots & \cdots & 1 & -2 \end{bmatrix}.$$

As in [46], we approximate integrals over the interval $[0, 1]$ as follows:

$$\begin{aligned} \int_0^1 \varphi(x)dx &= \int_0^{x_{\frac{1}{2}}} \varphi(x)dx + \sum_{p=1}^{N} \int_{x_{p-\frac{1}{2}}}^{x_{p+\frac{1}{2}}} \varphi(x)dx + \int_{x_{N+\frac{1}{2}}}^{x_{N+1}} \varphi(x)dx \\ &= \int_0^{x_{\frac{1}{2}}} \varphi(x)dx + \Delta x \sum_{p=1}^{N} \varphi(x_p) + \int_{x_{N+\frac{1}{2}}}^{x_{N+1}} \varphi(x)dx + O(\Delta x^2) \\ &= \sum_{p=1}^{N} \varphi(x_p) + O(\Delta x). \end{aligned}$$

Above, the boundary integrals are discarded since we use the first-order approximation of the Neumann boundary conditions. Then the discrete inner product between $u, v \in \mathbb{C}^N$ is,

$$\langle u, v \rangle = \Delta x \sum_{p=1}^{N} \overline{u}_p v_p.$$

Now that we have defined the discrete Neumann Laplacian operator, we can define the different Hamiltonian operators:

$$H_0 = -\beta^2 \Delta_{\text{Neu}}, \quad H = H_0 - \text{diag}(V + V^{\text{ext}}), \quad H_A = H_0 + \text{diag}(A),$$

where $\text{diag}(W)$ for $W \in \mathbb{R}^N$ denotes the diagonal matrix with the vector w on the diagonal. For simplicity, we will just write $H_0 + W$ for $H_0 + \text{diag}(W)$. Above, V^{ext}, V, and A are the discrete counterparts to the external, Poisson, and chemical potentials, respectively.

The discrete density operator is given by a positive self-adjoint matrix ϱ and it is written as:

$$\varrho = \sum_{p=1}^{N} \rho_p \left|\phi_p\right\rangle \left\langle\phi_p\right|,$$

where the eigenvalues, ρ_p, are such that $\text{Tr}(\varrho) = \sum_{p=1}^{N} \rho_p = 1$, and the eigenvectors $\{\phi_p\}_{p=1}^{N}$ are such that $\langle \phi_p, \phi_q \rangle = \delta_{pq}$. This means we can represent the discrete local density as

$$n[\varrho] = n_\varrho = \sum_{p=1}^{N} \rho_p |\phi_p|^2 \ \in \mathbb{R}^N.$$

The discrete Poisson equation then becomes

$$\alpha^2 \Delta_{\text{Dir}} V = n_\varrho. \tag{5.1}$$

Next, we use the spatial discretizations discussed above to introduce the fully discrete subproblems. We begin with the collision subproblem and the associated free energy minimization problem.

5.1.1 Discrete Collision Subproblem

In this section, we detail the resolution of the collision subproblem (4.7). Recall, it is given by

$$\partial_t \varrho_1 = \frac{1}{\varepsilon^2}(\varrho_{\mathrm{e}}[\varrho_1^{(0)}] - \varrho_1), \quad \varrho_1(t=0) = \varrho_1^{(0)}$$

where

$$\varrho_1^{(0)} = \sum_{p=1}^{N} \sigma_p \left|\phi_p\right\rangle \left\langle\phi_p\right|,$$

is the initial condition. The matrix $\varrho_{\mathrm{e}}[\varrho_1^{(0)}]$ represents the discrete local equilibrium operator and it is the minimizer of the discrete free energy

$$F(\sigma) = \mathrm{Tr}(\sigma\log(\sigma) - \sigma) + \mathrm{Tr}(H_0\sigma),$$

over positive matrices σ such that $n_\sigma = n_\varrho$. Note that this definition of the free energy differs from (3.43) (aside from the fact it has been scaled). In the context of the numerical scheme, it is sufficient to consider $\mathrm{Tr}(H_0\sigma)$ rather than $\mathrm{Tr}(H\sigma)$ because

$$\mathrm{Tr}(H\sigma) = \mathrm{Tr}(H_0\sigma) - \langle V + V^{\mathrm{ext}}, n_\sigma\rangle,$$

and the last term is fixed because $n_\sigma = n_\varrho$, so the Poisson (and external) potential remains unchanged within the collision subproblem. Thus, we ignore this term with the potentials and only consider $\mathrm{Tr}(H_0\sigma)$ in the definition of the free energy.

As in Section 3.3.1, we recast the constrained minimization of $F(\sigma)$ into the equivalent unconstrained minimization problem using Lagrange multiplier theory. In practice, we minimize a

discrete version of the functional in (3.46), meaning

$$J(A) = \sum_{p=1}^{N} e^{-\lambda_p[A]} + \langle A, n_\varrho \rangle \,, \tag{5.2}$$

where $\{\lambda_p[A]\}_{p=1\ldots N}$ are the eigenvalues of the Hamiltonian $H_A = H_0 + A$. In [46], it is proved that the discrete functional $J(A)$ is strictly convex and admits a unique minimizer. The minimization procedure will be introduced in the next section.

For now, assume we have obtained the minimizer, denoted $A[\varrho_1^{(0)}] = A_0$. This allows us to compute the equilibrium operator as the matrix

$$\varrho_{\mathrm{e}}[\varrho_1^{(0)}] = \sum_{p=1}^{N} e^{-\lambda_p[A_0]} \, |\psi[A_0]\rangle \, \langle \psi[A_0]| \,,$$

where $\{\lambda_p[A_0], \psi_p[A_0]\}_{p=1,\ldots,N}$ are the spectral elements of the discrete Hamiltonian H_{A_0}. Then the solution to the discrete collision subproblem is given by

$$\varrho_1(t) = e^{-t/\varepsilon^2} \varrho_1^{(0)} + (1 - e^{-t/\varepsilon^2}) \varrho_{\mathrm{e}}[\varrho_1^{(0)}]. \tag{5.3}$$

For the addition of the two discrete density operators above, we project the matrix $\varrho_1^{(0)}$ onto the basis of $\varrho_{\mathrm{e}}[\varrho_1^{(0)}]$. The resolution of the collision subproblem comes down to the minimization of $J(A)$ to obtain the appropriate equilibrium operator in order to update the density operator via (5.3). Next we detail the minimization procedure used to compute the minimizer of $J(A)$.

5.1.2 Minimization Procedure for $J(A)$

The minimization of the functional $J(A)$ in (5.2) is essential to the resolution of the collision subproblem. We obtain the minimizer by sing the Polak-Ribière variant of the nonlinear conjugate gradient algorithm. For a given local density n_ϱ, the unique minimizer $A_\star$ is such that $n_{e^{-H_{A_\star}}} = n_\varrho$.

We begin with an initial guess $A^{(0)}$, and must find an initial search direction $s^{(0)}$ and step length $b^{(0)}$ to initialize the algorithm. We set $s^{(0)} = -\nabla_A J(A^{(0)}) \in \mathbb{R}^N$, with,

$$\nabla_A J(A) = n_\varrho - n_{e^{-H_A}} = n - \sum_{p=1}^{N} e^{-\lambda_p[A]} |\psi_p[A]|^2, \tag{5.4}$$

which is the discrete version of (3.47) [46]. Above, $\{\lambda_p[A_0], \psi_p[A_0]\}_{p=1,\dots,N}$ are the spectral elements of $H_A = H_0 + A$. We find an initial step length via a line search:

$$b^{(0)} = \text{argmin}_{b\in\mathbb{R}} J\left(A^{(0)} + bs^{(0)}\right).$$

The line search is performed via Newton's method, with the Hessian of $J(A)$ given explicitly, see [46] and [57],

$$\left(\nabla_A^2 J(A)\right)_{ij} = \sum_{p=1}^{N}\sum_{q=1}^{N} \omega_{pq} \Psi_{pq}^i \left(\Psi_{pq}^j\right)^*, \quad i,j = 1,\dots,N,$$

where

$$\omega_{pq} = \begin{cases} -\frac{e^{-\lambda_p[A]} - e^{-\lambda_q[A]}}{\lambda_p[A] - \lambda_q[A]}, & \text{if } p \neq q \\ e^{-\lambda_p[A]}, & \text{if } p = q \end{cases}, \quad \text{and } \Psi_{pq}^i = \psi_p^i \psi_q[A]^j[A],$$

for $\psi_p^i[A]$ the i-th component of the vector $\psi_p[A] \in \mathbb{C}^N$. The chemical potential is then updated as $A^{(1)} = A^{(0)} + b^{(0)}s^{(0)}$. We now have the proper quantities to initialize the nonlinear conjugate gradient.

The nonlinear conjugate gradient algorithm is then as follows:

While $\left\|dA^{(k)}\right\|_{\ell_1} >$ tolerance

- Compute the steepest descent direction, $dA^{(k)} = -\nabla_A J(A^{(k)})$,
- Compute $c = \max\{0, c_{PR}\}$, where $c_{PR} = \frac{\left\langle dA^{(k)},\, dA^{(k)} - dA^{(k-1)}\right\rangle}{\left\langle dA^{(k-1)},\, dA^{(k-1)}\right\rangle}$,
- Update the search direction $s^{(k)} = dA^{(k)} + cs^{(k-1)}$,

- Perform line search $b_k = \text{argmin}_{b\in\mathbb{R}} J(A^{(k)} + bs^{(k)})$,
- Update chemical potential $A^{(k+1)} = A^{(k)} + b^{(k)}s^{(k)}$.

This minimization procedure provides us with the appropriate chemical potential, A_{min}, such that the local density is conserved: $n[\varrho_{\text{e}}[\varrho_1^{(0)}]] = n[\exp(-(H_0 + A_{\text{min}}))] = n[\varrho_1^{(0)}]$.

In Section 5.3, we explain how this nonlinear conjugate gradient procedure can be accelerated by exploiting regimes when β is small. We will look at a semi-classical approximation to the problem and this will provide us with an excellent initial guess for the chemical potential $A^{(0)}$. Within the conjugate gradient method the line search step is the most expensive computationally and we can use a semi-classical approximation of $J(A)$ to speed up this step. For now, we finish detailing the discrete splitting scheme by introducing the discrete transport subproblem in the next section.

5.1.3 Discrete Transport Subproblem

The spatially discrete version of the Transport subproblem (4.9) is

$$i\varepsilon\partial_t\varrho_2 = \frac{1}{\sqrt{2}\beta}[H, \varrho_2], \quad \varrho_2(t=0) = \varrho_2^{(0)} = \sum_{p=1}^{N} \gamma_p \left|v_p^{(0)}\right\rangle \left\langle v_p^{(0)}\right|.$$

The Hamiltonian is $H = -\beta^2 H_0 - V^{\text{ext}} - V$, for $V = V[\varrho_2]$ is the Poisson potential from (5.1) and $\{\gamma_p, v_p\}$ are the spectral elements of $\varrho_2^{(0)}$. Let the solution to the above system be given by

$$\varrho_2(t) = \sum_{p=1}^{N} \gamma_p \left|v_p(t)\right\rangle \left\langle v_p(t)\right|,$$

where each eigenvector $v_p(t)$ is the solution to the Schrödinger equation

$$i\partial_t v_p(t) = \frac{1}{\sqrt{2}\beta\varepsilon} H v_p(t) = \frac{1}{\sqrt{2}\beta\varepsilon}(-\beta^2 H_0 - V^{\text{ext}}) - \frac{1}{\sqrt{2}\beta\varepsilon} V(t) v_p(t) \tag{5.5}$$

$$:= H_L v_p + B(t) v_p, \tag{5.6}$$

with initial condition $v_p(t=0) = v_p^{(0)}$. Thus, the resolution of the transport subproblem comes down to updating the eigenvectors of ϱ_2 according to the above Schrödinger equation. Note that the transport subproblem is nonlinear because of the Poisson potential depends on the solution at any given time $V(t) = V[\varrho_2(t)]$. However, if we apply a Strang splitting scheme to resolve the nonlinear Schrödinger equation (5.5), we can treat the Poisson potential as linear. The splitting scheme is defined by splitting the Hamiltonian H_L away from the nonlinear term $B(t)v_p$ to create two linear subproblems.

The approximate Strang solution $v_p^{(1)}$ for the nonlinear Schrödinger equation (5.5) at time $t = h$ is given by

$$v_p^{(1)} = e^{-ihH_L/2} S(h) e^{ihH_L/2} v_p^{(0)}.$$

Let $w_p(t) := e^{-ihH_L} w_p^{(0)}$, then $w_p(t)$ is the solution to the linear Schrödinger equation subproblem, which is given by

$$i\partial_t w_p = H_L w_p = \frac{1}{\sqrt{2}\beta\varepsilon}(-\beta^2 \Delta_{\text{Neu}} - V^{\text{ext}}) w_p, \quad \text{for } p = 1, \ldots, N, \tag{5.7}$$

with $w_p^{(0)} = w_p(t=0)$. The solution to the Poisson potential subproblem $z_p(t) := S(t) z_p^{(0)}$ is reduced to the following set of ODEs

$$i\partial_t z_p = -\frac{1}{\sqrt{2}\beta\varepsilon} V(t) z_p, \quad \text{for } p = 1, \ldots, N. \tag{5.8}$$

In terms of the density operator, ϱ_2, the transport subproblem splitting scheme yields the approximate solution at $t = h$:

$$\varrho_2^{(1)} = e^{-ihH_L/2} S(h) e^{-ihH_L/2} \varrho_2^{(0)} e^{ihH_L/2} S^*(h) e^{ihH_L/2}. \tag{5.9}$$

As mentioned, by introducing the secondary spitting scheme for the transport subproblem we can handle the Poisson potential nonlinearity as we dealt with the collision subproblem nonlinearity. The reason we can treat the Poisson potential linearly, is due to the fact (5.8) preserves $|z_p|$

because V is real-valued. This is helpful because, for a given density operator ϱ the local density is conserved under the Poisson equation, meaning

$$n[S(t)\varrho S^*(t)] = n[\varrho], \quad \forall\, t \geq 0.$$

This allows us to now treat the Poisson potential $V(t)$ in (5.8) as linear:

$$V(t) = V[S(t)e^{-ihH_L/2}\varrho_2^{(0)}e^{ihH_L/2}S^*(t)] = V[e^{-ihH_L/2}\varrho_2^{(0)}e^{ihH_L/2}] = V(0),$$

where $V(0)$ is obtained as the solution to the Poisson equation

$$\alpha^2\Delta_{\text{Dir}}V = n[e^{-ihH_L/2}\varrho_2^{(0)}e^{ihH_L/2}].$$

This makes the resolution of (5.8) straightforward.

Lastly, we need to resolve the linear Schrödinger subproblem given in (5.7). We use the standard Crank-Nicolson scheme to obtain approximate solutions for $w_p^{(1)}$ from $w_p^{(0)}$. The approximate solution to (5.7) at $t = h$ is then,

$$\left(i\mathbb{I} - \frac{h}{2}H_L\right)w_p^{(1)} = \left(i\mathbb{I} + \frac{h}{2}H_L\right)w_p^{(0)}, \tag{5.10}$$

where $\mathbb{I}$ denotes the N by N identity matrix.

We have now introduced the fully discrete Strang splitting scheme for the quantum Liouville-BGK equation. So far, we have seen that the scheme is indeed convergent and, numerically, we have confirmed the discrete scheme is second-order in time. As an application of the numerical scheme we perform a numerical study of different collision regimes in a resonant tunneling diode. The quantum Liouville-BGK equation is considered a “moderate" collision regime, in which collisions are present but do not dominate the dynamics. The ballistic-Liouville equation represents a collision-free regime and we use the quantum drift diffusion model to represent a collision-dominated regime. In the next section we introduce the quantum drift diffusion model.

5.2 Quantum Drift-Diffusion Model

The quantum drift-diffusion model is a so-called quantum diffusion model which is another example of a fluid (macroscopic) quantum model [43]. Formally, the QDD can be derived from the QLE as a diffusive limit (τ or ε approach 0) or the QDD can be derived from an entropy (free energy) minimization principle. The diffusive regime for the quantum Liouville equation occurs at times much larger than the relaxation time τ (or the scaled version ε). We are interested in the QDD because it represents a regime in which scattering dominates the dynamics. The material in this section is a review of the articles [43, 44, 46, 53]. In particular, we use the numerical method first described Gallego and Méhats in [46] to compute solutions to the QDD for the numerical study of collision regimes.

The dimensional quantities in QDD are scaled in the same way as the QLE. In addition to the scaling relationships defined in (3.48), an additional reference is needed for the current, $\bar{j} = \frac{\mu k_B T_0 \bar{n}}{Le}$, and we set $j' = j/\bar{j}$ [44]. Using these conventions, the scaled QDD model is obtained as follows (omitting the primes on the dimensionless variables):

$$\frac{\partial n}{\partial t} + \nabla \cdot (n \nabla (\mathcal{A} + \mathcal{V} + \mathcal{V}^{\text{ext}})) = 0 \tag{5.11}$$

$$\alpha^2 \Delta \mathcal{V} = n, \quad \mathcal{V}(0) = \mathcal{V}(1) = 0, \tag{5.12}$$

$$n = n_{\varrho_e[\mathcal{A}]} = \sum_{p \in \mathbb{N}} e^{-\lambda_p[\mathcal{A}]} |\phi_p[\mathcal{A}]|^2, \tag{5.13}$$

where $(\lambda_p[\mathcal{A}], \phi_p[\mathcal{A}])_{p \in \mathbb{N}}$ are the spectral elements of the Hamiltonian $\mathcal{H}_{\mathcal{A}} = -\beta^2 \Delta + \mathcal{A} = \mathcal{H}_0 + \mathcal{A}$. As with the QLE, the Hamiltonian is equipped with Neumann boundary conditions. Finally, insulating boundary conditions are specified for the electrochemical potential, i.e.

$$\frac{d}{dx}(\mathcal{A} + \mathcal{V} + \mathcal{V}^{ext})|_{x=0, x=L} = 0.$$

With such a condition, the total number of particles is preserved in the domain and there is no current at the boundary, as for the QLE. The dimensionless constants α and β are still given by the

relationship in (3.50). Maybe counterintuitively, the QDD is probably best seen as an evolution equation on the chemical potential $\mathcal{A}$ and the Poisson potential $\mathcal{V}$ rather than on the density n. Once the chemical potential is known, the density n can be obtained from the third equation in (5.13), which is the same as the local density of the associated equilibrium operator $\varrho_{\mathrm{e}}[\mathcal{A}] = \exp(-\mathcal{H}_{\mathcal{A}})$. The mathematical analysis of (5.11) is quite difficult, and an existence result in a one-dimensional periodic domain is obtained in [58].

The chemical potential $\mathcal{A}$ is found by minimizing the free energy. To see why, we seek an equilibrium density operator $\varrho_e(t) = \exp(-(\mathcal{H} + \mathcal{A}))$ that minimizes the free energy under the constraint of local density, as is done in the QLE. The equilibrium density operator is obtained by minimizing the free energy (3.43) under a local density constraint, which can be written as

$$\mathcal{F}(\varrho) = \mathrm{Tr}(\varrho \log \varrho - \varrho) + \mathrm{Tr}(\varrho \mathcal{H}_0) + \mathrm{Tr}(\mathcal{V}^{\text{ext}} \varrho) + \frac{\alpha^2}{2} \|\nabla \mathcal{V}\|_{L^2}^2.$$

Using the fact that density operator ϱ associated with the QDD solution is a quantum Maxwellian, $\varrho = \varrho_e = \exp(-(\mathcal{H} + \mathcal{A}))$, and substitute this into $\mathcal{F}$, we obtain an equivalent formulation of the free energy that is a function of $\mathcal{A}$ and $\mathcal{V}$

$$\mathcal{S}(\mathcal{A}, \mathcal{V}) = \mathcal{F}(\varrho_e) = -\int n(\mathcal{A} + 1 + \mathcal{V}^{\text{ext}}) dx + \frac{\alpha^2}{2} \int |\nabla \mathcal{V}|^2 dx. \tag{5.14}$$

It is shown in ([46], Theorem 3.1) that a semi-discrete in time version of $\mathcal{S}(\mathcal{A}, \mathcal{V})$ is strictly convex and coercive, and hence it admits a unique minimizer. In [46], Gallego and Méhats derive a numerical scheme for the QDD based on the minimization of (5.14). Before introducing the discretization of QDD in Section 5.2.2, we briefly review the formal derivation of the QDD as a diffusive limit of the QLE. This is outlined in the next section.

5.2.1 Formal Derivation from the Quantum Liouville Equation

The quantum drift-diffusion equation is a macroscopic model that can be obtained from the quantum Liouville equation. The following formal derivation follows the derivation given in [44].

An alternate derivation of the QDD using the entropy minimization principle can be found in [40]. To obtain the QDD from the QLE, it is necessary to perform a so-called diffusive limit, in which we scale time by the small parameter ε and look at the limit as ε goes to zero. The following calculations are formal. The starting point is the scaled QLE (3.49),

$$i\varepsilon\partial_t \varrho^\varepsilon = \frac{1}{\sqrt{2}\beta}[\mathcal{H}, \varrho^\varepsilon] + \frac{i}{\varepsilon}(\varrho_{\mathrm{e}}[\varrho^\varepsilon] - \varrho^\varepsilon), \quad x \in \Omega \subset \mathbb{R}. \tag{5.15}$$

The unitless parameter ε is the scaled mean free path, for which a typical value is about 0.5 at $T \approx 300K$. As temperature decreases the value of ε decreases, so considering the formal limit as ε approaches 0 is reasonable. We suppose now that ϱ depends on ε in some way and set $\varrho = \varrho^\varepsilon$ and it is assumed that in the limit $\varepsilon \to 0$ that $\varrho^\varepsilon \to \varrho^0$. If one multiplies through the scaled QLE by ε and takes the formal limit as ε approaches zero, this gives us

$$0 = i(\varrho_{\mathrm{e}}[\varrho^0] - \varrho^0).$$

Meaning, the limiting density operator is in the kernel of the collision operator, i.e. $\mathcal{Q}(\varrho^0) = 0$, which tells us that ϱ^0 is a minimizer of the quantum free energy and has the form of a quantum Maxwellian,

$$\varrho^0 = e^{-(\mathcal{H}_0 + \mathcal{A}(t,x))},$$

where the chemical potential $\mathcal{A}$ is found by minimizing the functional $\mathcal{J}(\mathcal{A})$ in (3.46). Denote the Hamiltonian in the limiting quantum Maxwellian by $\mathcal{H}[\mathcal{A}] = \mathcal{H}_0 + \mathcal{A}$.

In the spirit of the classical case, in which a Chapman-Enskog expansion is used to derive hydrodynamic equations from the Boltzmann equation, we assume that ϱ^ε will have the form of a first-order Chapman-Enskog expansion, i.e.

$$\varrho^\varepsilon = \varrho_{\mathrm{e}}[\varrho^\varepsilon] + \varepsilon\varrho_1^\varepsilon. \tag{5.16}$$

From (5.16), we can conclude that

$$\frac{1}{\varepsilon}(\varrho_{\mathrm{e}}[\varrho^{\varepsilon}] - \varrho^{\varepsilon}) = -\varrho_1^{\varepsilon},$$

and substituting this into the scaled QLE with $\varrho = \varrho^{\varepsilon}$ we find

$$i\varepsilon\partial_t\varrho^{\varepsilon} = \frac{1}{\sqrt{2}\beta}[\mathcal{H}, \varrho^{\varepsilon}] - i\varrho_1^{\varepsilon}. \tag{5.17}$$

Then taking the formal limit $\varepsilon \to 0$, we find that

$$\varrho_1^0 = -\frac{i}{\sqrt{2}\beta}[\mathcal{H}, \varrho^0]. \tag{5.18}$$

To finish the formal derivation of the QDD from the QLE, we turn to a weak formulation of the QLE obtained by multiplying (5.15) on the right by a smooth test function φ and taking the trace of the result.

$$\mathrm{Tr}(i\partial_t\varrho^{\varepsilon}\varphi) = \frac{1}{\sqrt{2}\beta\varepsilon}\,\mathrm{Tr}([\mathcal{H}, \varrho^{\varepsilon}]\varphi), \tag{5.19}$$

where the term $\mathrm{Tr}((\varrho_{\mathrm{e}}[\varrho^{\varepsilon}] - \varrho^{\varepsilon})\varphi) = 0$. To see why, the local density $n[\varrho]$ can be defined weakly by $\int_\Omega n[\varrho]\varphi dx = \mathrm{Tr}(\varrho\varphi)$ and the quantum Maxwellian is such that $n_{\varrho_{\mathrm{e}}[\varrho^{\varepsilon}]} = n_{\varrho^{\varepsilon}}$. Next, we substitute the Chapman-Enskog expansion for ϱ^{ε} into the above equation. First, notice that $\mathcal{H} = \mathcal{H}_0 + \mathcal{A}^{\varepsilon} - (\mathcal{A}^{\varepsilon} - \mathcal{V}) = \mathcal{H}[\mathcal{A}^{\varepsilon}] - (\mathcal{A}^{\varepsilon} - \mathcal{V})$ where $\mathcal{A}^{\varepsilon}$ is the chemical potential associated with ϱ^{ε}. Thus the term that is the trace of the commutator can be simplified using

$$\mathrm{Tr}([\mathcal{H}, \varrho_{\mathrm{e}}[\varrho^{\varepsilon}]]\varphi) = \mathrm{Tr}([\mathcal{H}[\mathcal{A}^{\varepsilon}], \varrho_{\mathrm{e}}[\varrho^{\varepsilon}]]\varphi) - \mathrm{Tr}([\mathcal{A}^{\varepsilon} - \mathcal{V}, \varrho_{\mathrm{e}}[\varrho^{\varepsilon}]]\varphi) = 0.$$

Above the first commutator is equal to zero because these two operators commute due to the fact that $\varrho_{\mathrm{e}}[\varrho^{\varepsilon}]$ is a function of the Hamiltonian $\mathcal{H}[\mathcal{A}^{\varepsilon}]$. The second commutator is equal to zero thanks to the cyclicity of the trace, i.e. $\mathrm{Tr}([a, b]c) = \mathrm{Tr}(a[b, c]) = \mathrm{Tr}([c, a]b)$ and using the fact that

$[\mathcal{A} - \mathcal{V}, \varphi] = 0$. With this simplification of the commutator, (5.19) becomes

$$\mathrm{Tr}(i\partial_t \varrho^\varepsilon \varphi) = \frac{1}{\sqrt{2}\beta} \mathrm{Tr}([\mathcal{H}, \varrho_1^\varepsilon]),$$

where the only dependence on ε is in the Chapman-Enskog expansion of ϱ^ε. Taking the limit of the above result and substituting (5.18) yields

$$\mathrm{Tr}(i\partial_t \varrho^\varepsilon \varphi) = \frac{1}{2\beta^2} \mathrm{Tr}\big(i[\mathcal{H}, [\mathcal{H}, \varrho^0]]\varphi\big).$$

As before, we write $\mathcal{H} = \mathcal{H}[\mathcal{A}] - (\mathcal{A} - \mathcal{V})$, then use the fact that ϱ^0 must be a quantum Maxwellian to conclude the term commutator of ϱ^0 with the appropriate Hamiltonian is zero. Thus the inner commutator can be simplified to

$$[\mathcal{H}, \varrho^0] = -[\mathcal{A} - \mathcal{V}, \varrho^0].$$

Using this and the cyclicity of trace once again, the trace of the double commutator can be written as $\mathrm{Tr}([\mathcal{H}, [\mathcal{A} - \mathcal{V}, \varrho^0]]\varphi) = \mathrm{Tr}([-\beta^2\Delta, [A - V, \varrho^0]]\varphi)$. We now have,

$$\mathrm{Tr}(i\partial_t \varrho^\varepsilon \varphi) = \frac{1}{2\beta^2} \mathrm{Tr}\big(i[-\beta^2\Delta, [\mathcal{A} - \mathcal{V}, \varrho]]\phi\big). \tag{5.20}$$

Using the cyclicity of trace and direct computation of the resulting double commutator gives

$$\mathrm{Tr}\big(i[-\beta^2\Delta, [\mathcal{A} - \mathcal{V}, \varrho]]\phi\big) = i2\beta^2 \mathrm{Tr}\big(\varrho^0 \nabla\varphi \cdot \nabla(\mathcal{A} - \mathcal{V})\big). \tag{5.21}$$

Substituting this into (5.20) yields

$$\mathrm{Tr}(i\partial_t \varrho^\varepsilon \varphi) = i2\beta^2 \mathrm{Tr}\big(\varrho^0 \nabla\varphi \cdot \nabla(\mathcal{A} - \mathcal{V})\big).$$

Using the weak formulation of the local density, $\forall\phi \int_\omega n\phi dx = \mathrm{Tr}(\varrho\phi)$, we can rewrite the above equation as a weak formulation of the quantum drift-diffusion equation, i.e.,

$$\int_\Omega \partial_t n_{\varrho^0}\varphi dx = \int_\Omega n_{\varrho^0}\nabla(\mathcal{A}-\mathcal{V})\varphi dx, \forall\varphi. \tag{5.22}$$

We have shown that (formally) the quantum-drift diffusion equation can be derived from the quantum Liouville equation as a diffusive limit. As a result, it is expected that the solution to the quantum Liouville equation approaches the solution to the quantum drift-diffusion equation in the long-time limit. This is confirmed with a numerical example in Section 5.3.

In the next section, we review the numerical scheme for the quantum drift-diffusion model introduced by Gallego and Méhats in [46].

5.2.2 Quantum Drift-Diffusion Numerical Scheme

For completeness, we include the following results on the numerical method for the quantum drift-diffusion model. This numerical method was originally described in [46] and [57] and all relevant details can be found in those sources. As with the QLE, the semi-discrete QDD is the starting point, which is already discretized temporally. Following [46], let $t_k = k\Delta t$, then we have

$$\begin{aligned}
\frac{n^{k+1}-n^k}{h} + \nabla\cdot(n^k\nabla(A^{k+1}+V^{k+1}+V^{\text{ext}}) &= 0,\\
\alpha^2\Delta V^{k+1} &= n^{k+1},\\
n^{k+1} &= \sum_{p=1}^{\infty} e^{-\lambda_p[A^{k+1}]}\left|\phi_p[A^{k+1}]\right|^2,
\end{aligned}$$

with the boundary conditions $V^{k+1}(0) = V^{k+1}(L) = 0$ and $\partial_\nu(A^{k+1}+V^{k+1}+V^{\text{ext}}) = 0$. The unknowns are A^{k+1}, V^{k+1}, and n^{k+1}. But, once A^{k+1} is known, the value of n^{k+1} can be computed using the spectral decomposition of the local density. The “real" unknowns are A^{k+1} and V^{k+1} and

they can be found by minimizing the functional,

$$\mathcal{G}(A,V)=\frac{h}{2}\int n^k|\nabla(A-V)|^2dx+\frac{\alpha^2}{2}\int|\nabla V|^2dx+\int n^k(A-V)dx+\sum_{p=1}^{\infty}e^{-\lambda_p[A]}, \quad (5.23)$$

for n^k given and $V\in H_0^1(\Omega)$, $A\in H^1(\Omega)$ where $\Omega=[0,1]$.

The spatial grid is identical to that of the QLE. The fully discrete scheme of [46] is first-order in time and space, implicit, and reads

$$\begin{cases}\frac{n^{k+1}-n^k}{h}+\frac{1}{2}\widetilde{D}_-(n^kD_+(A^{k+1}+W^{k+1}))+\frac{1}{2}\widetilde{D}_+(n^kD_-(A^{k+1}+W^{k+1}))=0\\ \alpha^2\Delta_{\text{Dir}}V^{k+1}=n^{k+1},\quad W^k=V^k+V^{\text{ext}}\\ n^{k+1}=\sum_{p=1}^{N}e^{-\lambda_p[A^{k+1}]}\big|\psi_p[A^{k+1}]\big|^2,\end{cases} \quad (5.24)$$

where $\{\lambda[A^k],\psi_p[A^{k+1}]\}$ are the eigenvalues and eigenvectors of H_0+A^k. The $N\times N$ matrices $D_+,\ \widetilde{D}_+,\ D_-,\ \widetilde{D}_-$ are given by

$$D_+=\frac{1}{\Delta x}\begin{bmatrix}-1&1&0&\cdots&0\\0&-1&1&\cdots&0\\\vdots&\ddots&\ddots&&\vdots\\0&\cdots&0&-1&1\\0&\cdots&\cdots&0&0\end{bmatrix},\qquad \widetilde{D}_+=\frac{1}{\Delta x}\begin{bmatrix}-1&1&0&\cdots&0\\0&-1&1&\cdots&0\\\vdots&\ddots&\ddots&&\vdots\\0&\cdots&0&-1&1\\0&\cdots&\cdots&0&-1\end{bmatrix},$$

and

$$D_-=\frac{1}{\Delta x}\begin{bmatrix}0&0&0&\cdots&0\\-1&1&0&\cdots&0\\\vdots&\ddots&\ddots&&\vdots\\0&\cdots&\cdots&1&0\\0&\cdots&\cdots&-1&1\end{bmatrix},\qquad \widetilde{D}_-=\frac{1}{\Delta x}\begin{bmatrix}1&0&0&\cdots&0\\-1&1&0&\cdots&0\\\vdots&\ddots&\ddots&&\vdots\\0&\cdots&\cdots&1&0\\0&\cdots&\cdots&-1&1\end{bmatrix}.$$

The Neumann boundary conditions are accounted for in the definition of the above matrices, as $\Delta_{\text{Neu}} = \widetilde{D}_- D_+ = \widetilde{D}_+ D_-$. In (5.24), for simplicity of notation, we let UV denote the Hadamard prodcut of $U,\ V \in \mathbb{R}^N$, i.e. $UV = U \odot V$. The idea of for the QDD scheme in [46] is the following: Given n^k, the solution (A^{k+1}, V^{k+1}) to the implicit relation (5.24) is obtained as the unique minimizer of the strictly convex functional

$$\begin{aligned} G(A,V) = \frac{h\Delta x}{4}\sum_{i=1}^{N} n_i^k (D_+(A+V+V^{\text{ext}})_i^2 + \frac{h\Delta x}{4}\sum_{i=1}^{N} n_i^k (D_-(A+V+V^{\text{ext}})_i^2 \\ + \sum_{i=1}^{N} e^{-\lambda_i[A]} + \frac{\alpha^2\Delta x}{2}\sum_{i=1}^{N}(D_+V)_i^2 + \frac{\alpha^2}{2\Delta x}(V_1^2 + V_N^2) \\ + \Delta x \sum_{i=1}^{N} n_i^k (A_i + V_i + V_i^{\text{ext}}). \end{aligned}$$

Thus, quantum drift-diffusion numerical scheme reduces to a repeated application of the minimization of the functional $G(A,V)$, which is equivalent to the quantum free energy in the case that $\varrho = \exp(-(\mathcal{H}+\mathcal{A}))$. In practice, the minimization of the functional $G(A,V)$ is accomplished in the same manner as the minimization of the collision step of the QLE.

As mentioned before, the QDD represents a collision dominated regime in the hierarchy of quantum fluid models. In the next section, we are applying the splitting scheme for the QLE in a numerical study of collision regimes. We use the minimization scheme for the QDD from [46] introduced in this section to compute solutions to the QDD for this numerical study. We present the results of the collision regime study next.

5.3 A Numerical Study of Collision Regimes

In this section a numerical study of the effects of collision in electron transport is presented. The three models used in this numerical study are the ballistic quantum Liouville equation (3.3), the quantum Liouville-BGK equation (3.1), and the quantum drift-diffusion model (5.12). The models represent a transport dominated regime, an intermediate regime, and a collision dominated regime, respectively. Recall, the QDD model can be derived from the QLE in the limit as ε ap-

proaches zero. Thus, the smaller the value of ε in the QLE, the stronger the effects of collision are on the dynamics. Further, since the QDD can be viewed as a long-time limit of the QLE, the two models approach the same global equilibrium which is the form of a quantum Maxwellian. We are considering these three models in three scenarios for the external potential: free space, a single potential barrier, and a double potential barrier. The last case is considered a simplified 1-dimensional Resonant Tunneling Diode (RTD) model, which is an example of a quantum heterostructure, and has been studied in [43,44,46,47,59], for example. The RTD is a device that has non-linear current-voltage characteristics which allow for applications in electronics logic [35]. The RTD is composed of two semiconductor crystals – typically Gallium Arsenide (GaAs) and two small strips of Aluminum Gallium Arsenide (AlGaAs). The small strips of the second crystal create a double potential barrier due to the conduction band gap between the two materials. Inside the barriers, there are several resonant energies, and if an electron has an energy sufficiently close to one of the resonant energies, it can penetrate the potential barriers. This is thanks to the physical phenomena of quantum tunneling. For the purpose of our study of collision regimes, we will represent an RTD with the external potential, V^{ext}, as a double barrier:

$$V^{\text{ext}}(x) = \begin{cases} V_0, & x^1 \leq x \leq x^2, \text{ and } x^3 \leq x \leq x^4, \\ 0, & \text{otherwise} \end{cases},$$

where $0 < x^1 < x^2 < x^3 < x^4 < 1$ and $V_0 < 0$. As noted in the spatial discretization section, we need to ensure that the jump locations (i.e. $x = x^1, x^2, x^3,$ and x^4) land at a midpoint of the discretization scheme, say $x_{p+\frac{1}{2}}$ for some p. The potential barrier width $x^2 - x^1$ and $x^4 - x^3$ are typically very small, on the order of about 5 nanometers. Figure 5.1 shows a schematic representation of an RTD device comprised of layered materials and the one-dimensional potential profile model we use to represent the dynamics orthogonal to the layers in the RTD.

In the QLE, we take $\varepsilon = 0.5$ and $\varepsilon = 0.1$, to represent a transport regime with moderate collision effects and we expect to begin to see the effects of the collision operator after enough

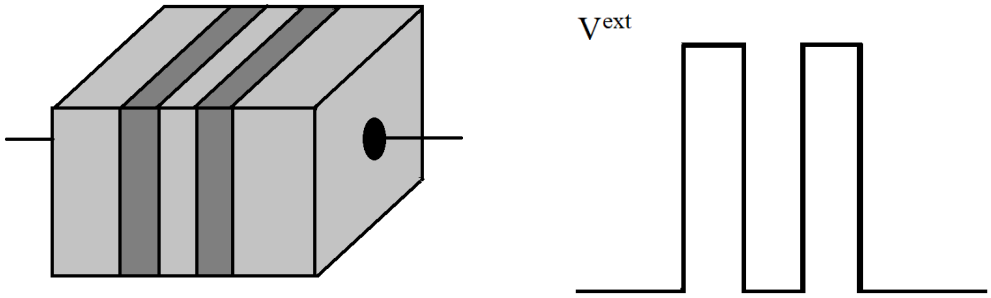

(a) The structure of a RTD formed by layers of different semiconductor materials.

(b) The one dimensional potential profile of the RTD.

Figure 5.1: A schematic representation of a Resonant Tunneling Diode with the simplified one-dimensional potential barrier structure used in simulations.

time has passed, about $t \approx \varepsilon$. The *Ballistic quantum Liouville* equation is given by

$$i\varepsilon\partial_t \varrho = \frac{1}{\sqrt{2}\beta}[H, \varrho], \quad \varrho(t=0) = \varrho^0, \tag{5.25}$$

is used as the collision-free model. As in the QLE, ϱ is a density matrix, the Hamiltonian $H = -\beta^2\Delta_{\text{Neu}} - (V + V^{\text{ext}})$, and V is the Poisson potential that solves

$$\alpha^2\Delta_{\text{Dir}}V = n[\varrho].$$

Equation (5.25) is non-dimensionalized and it is obtained by scaling (3.3) using the scaling in (3.48), which is the same scaling used for the QLE. The constants α, β, and ε are defined in (3.50). The ballistic model is simply the transport subproblem of the QLE and we resolve this equation using the splitting scheme outlined in Section 5.1.3. The quantum drift-diffusion equation is resolved with the numerical scheme introduced in [46], which was recalled in Section 5.2.

We will take an initial condition for the QLE as a superposition of wave packets of the form

$$\varrho^0 = \frac{\chi\gamma_0\chi}{\text{Tr}(\chi\gamma_0\chi)}. \tag{5.26}$$

The function $\chi(x)$ is a Gaussian $\chi(x; x_0, \sigma) = e^{-(x-x_0)/\sigma^2}$, and γ_0 is the density operator

$$\gamma_0 = \sum_{p=1}^{N_I} e^{-\lambda_p} |\psi_p\rangle \langle\psi_p| ,$$

where $\lambda_p = (\beta\pi p)^2$ and $\psi_p(x) = e^{i3\pi px}$. The initial data for the QLE (and ballistic Liouville) is the matrix ϱ^0, and the corresponding local density $n^0 = n[\varrho^0]$ is the initial data for the QDD. The local density of the initial condition is computed after diagonalizing the matrix ϱ^0. We now turn our attention to the initialization of the chemical potential.

5.3.1 Initialization of the Minimization Algorithms

The nonlinear conjugate gradient methods require a good initial guess for $A^{(0)}$ for fast convergence. This is true for both $J(A)$ in the QLE and for $G(A, V)$ for the QDD. Let $\varrho_{e,0} = \exp(-(H_0 + A^0))$ denote the equilibrium operator associated with $n^0 = n[\varrho^0]$, i.e. $n[\varrho_{e,0}] = n^0$. For the initial chemical potential guess, we seek an approximation of the desired chemical potential A^0. In the configuration for our numerical results, the parameter $\beta = 0.01$ to allow for a sufficient number of modes in the density operators. Since we desire small β in our application, we can utilize this to approximate $\varrho_{e,0} = \exp(-(H_0 + A^0))$ using semi-classical analysis. For the continuous problem, it is shown in [53] that, for x away from the boundaries,

$$n[e^{-(\mathcal{H}_0+\mathcal{A})}](x) = \frac{1}{2\sqrt{\pi}\beta} e^{-\mathcal{A}(x)} + o(1), \tag{5.27}$$

where $o(1)$ refers to a term that is small in an appropriate sense when $\beta \ll 1$. If we then use the fact that $n^0 \approx \frac{1}{2\sqrt{\pi}\beta} e^{-\mathcal{A}(x)}$, and solve for $\mathcal{A}$, we set as an initial guess for the discrete problem

$$A_{\text{guess}} = -\log\big(2\sqrt{\pi}\beta n^0\big).$$

This initial guess for the chemical potential provides a good approximation of the exact solution A^0 for x away from the boundaries, see Figure 5.2. For the QDD minimization, we also need a

good guess for the initial Poisson potential, and this can be obtained simply by solving the Poisson equation with the initial local density n^0. The minimization of the functional $J(A)$ is dependent on satisfying the local density constraint in the underlying constrained free energy minimization, $n_0 = n_{\text{min}}$ and Figure 5.3 shows this is satisfied with our implementation minimization. Note $n_{\text{min}} = n[e^{-(H_0+A_{\text{min}})}]$ where A_{min} is the minimizer of $J(A)$ found using nonlinear conjugate gradient described in Section 5.1.2.

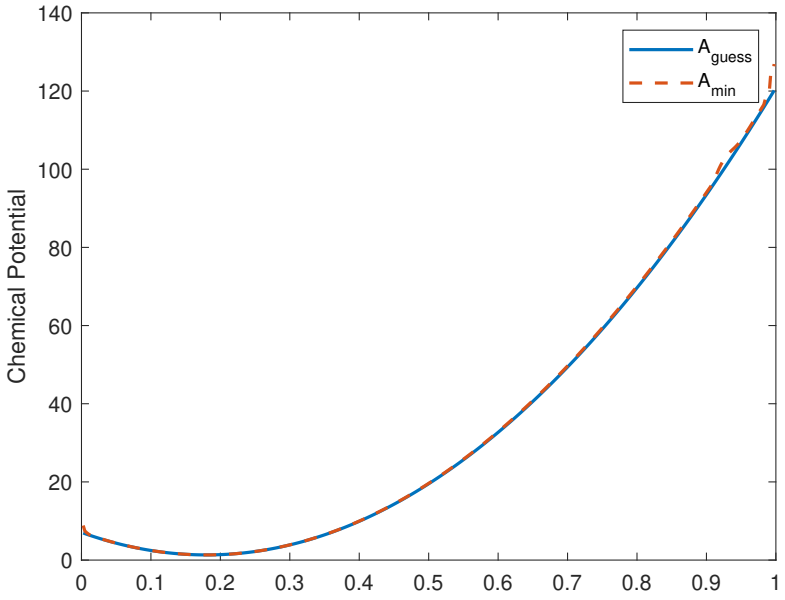

Figure 5.2: A comparison of the A_{guess} used to initialize the minimzation and the resulting minimizer, A_{min}.

The most expensive step of the minimization of $J(A)$ is the line search step because it requires repeated diagonalization of the matrices $H_0 + A$. We can use the semi-classical approximation of the local density (5.27) to obtain an approximate expression of $J(A)$. Again, this relies on the fact that β is small and a different approach must be used for larger values of β. Recall, the line search involves minimizing $G(b) = J(A + bs)$ over $b \in \mathbb{R}$, and we can approximate this as:

$$G_{\text{approx}}(b) = J_{\text{approx}}(A + bs) = \frac{\Delta x}{2\sqrt{\pi}\beta} \sum_{i=1}^{N} e^{-(A_i + bs_i)} + \langle n, A + bs \rangle \,.$$

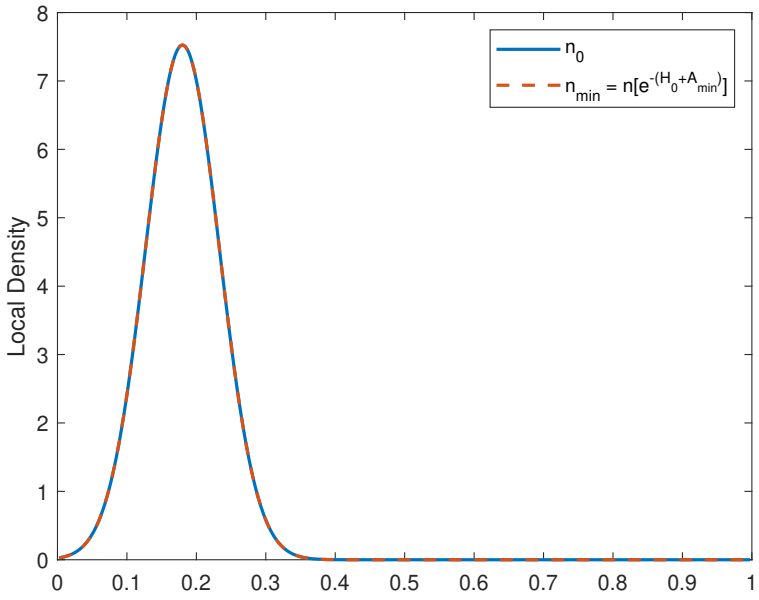

Figure 5.3: A comparison of the local density produced by the minimization of $J(A)$ in the QLE numerical scheme. The minimization routine is such that the local density is conserved.

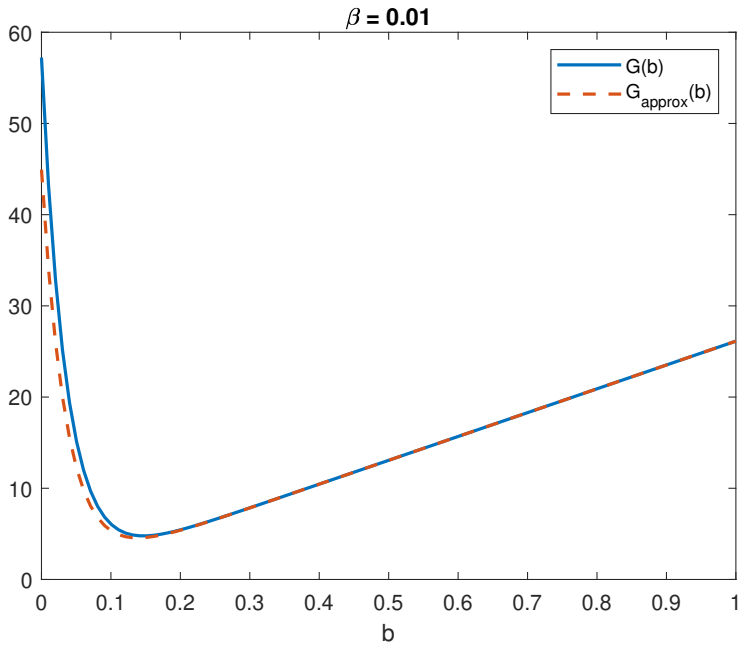

Figure 5.4: A comparison of $G(b) = J(A + bs)$ and the semi-classical approximation $G_{\text{approx}}(b)$ for n given by the Gaussian packet initial condition, $A = A_{\text{guess}}$, and $s = -\nabla J(A_{\text{guess}})$.

A straightforward Newton's method is used to find the $G_{\text{approx}}(b)$. The function $G_{\text{approx}}(b)$ is not accurate for all values of b, it provides an excellent approximation of the minimizer of $G(b) = J(A + bs)$. This approximation allows us to obtain an excellent guess of the line search parameter b without diagonalizing $H_0 + A$ and this greatly reduces the computational cost of the line search step. Figure 5.4 shows a comparison of $G(b)$ with $G_{\text{approx}}(b)$ for the initial step of the minimization procedure where n is the initial wave packet density, $A = A_{\text{guess}}$, and $s = -\nabla J(A_{\text{guess}})$.

Next, we present the numerical results of the study of different collision regimes.

5.3.2 Numerical Results

We now turn our attention to the results of the numerical study of different collision regimes and its effect on electron transport. Here we are considering the effects of collision on the dynamics of a Gaussian wave packet in the domain $[-0.5, 1.5]$ (nondimensional units). Note, we are interested in the dynamics on $[0, 1]$ with the particular external potentials chosen, but we compute the solutions on an extended domain to reduce the boundary effects seen in the ballistic model due to the choice of Neumann boundary conditions. Let the initial local density be given by $n[\varrho_0] = \sum_{p=1}^{M} \rho_p |\psi_p|^2$, where the spectral elements correspond to the diagonalized Gaussian wave packet (5.26). The Gaussian wave packet is centered at $x = 0.18$ which situates the initial density to the left of the considered potential barriers and away from the boundaries of the domain. In Figure 5.5 the quantity $\rho_p |\psi_p|^2$ is shown for the first five modes which have a statistical weight, ρ_p, of 0.1642, 0.1382, 0.1162, 0.0976, and 0.0820, respectively. In the numerical comparison, we take $V^{\text{ext}} = 0$ to assess the free-space dynamics, then we take V^{ext} to be a single potential barrier centered at $x = 0.5$, and finally, we take V^{ext} to be the double potential barrier with the potential well centered at $x = 0.5$. In the single and double barrier case the potential barriers are taken to have a height of -3 and a width of 0.076 (in nondimensional units). The spacing between the two potential barriers that forms a quantum well is also 0.076 units wide. The last case with the double potential barrier is representative of a simplified resonant tunneling diode which requires modeling the effects of quantum tunneling through the barriers. Figure 5.6 shows the single potential barrier and the

double potential barriers with the initial local density formed by the Gaussian wave packet. In the free-space case we still use the same initial condition as in the potential barrier cases. In the following results we used $\alpha = 1.7061$, $\beta = 0.01$, and $\varepsilon = 0.5$ or 0.1. Since we use $N_I = 50$ modes in the initial condition ρ_0, this yields a smallest wavelength of $d_{\text{min}} = 2/N_I = 1/25$ and the largest energy $\lambda_{N_I} = 4\pi^2 N_I^2 \beta^2 = 14.22$. Thus, we take $\Delta x \approx d_{\text{min}}/10$ and $\Delta t \approx 2\pi\sqrt{2}\beta\varepsilon/(10\lambda_{N_I})$ to ensure sufficient resolution of the high frequency oscillations.

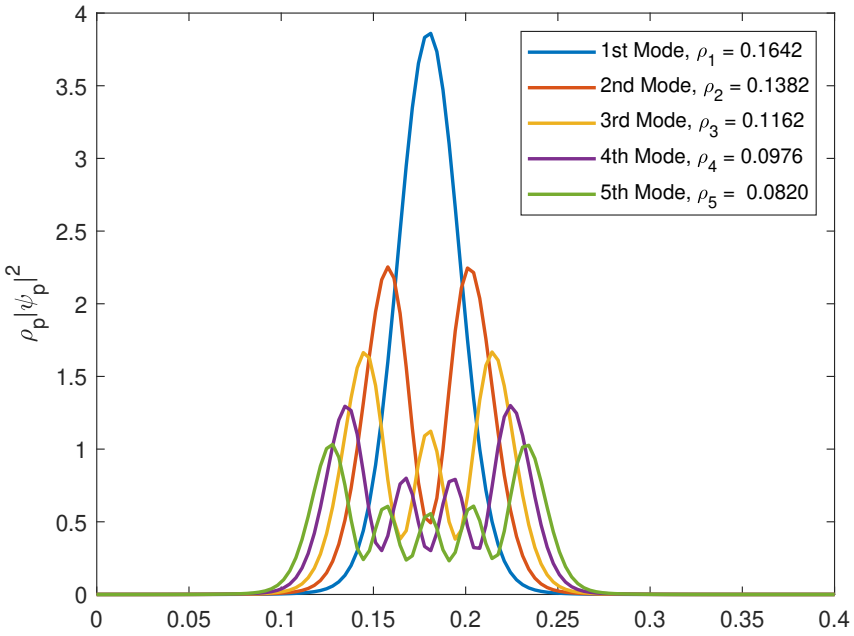

Figure 5.5: A plot of $\rho_p|\psi_p|^2$ for the first five modes of the Gaussian wavepacket initial condition.

In the free-space dynamics ($V^{\text{ext}} = 0$) case, we can see that the QLE and the ballistic cases show the wavefront transporting to the right through the domain, while the QDD immediately begins widening without any transport. Snapshots of the local density for QLE, ballistic QLE, and QDD when $\varepsilon = 0.5$ is shown in Figure 5.7, and when $\varepsilon = 0.1$ in Figure 5.8. In the ballistic case, the wavefront hits the boundary of the domain at $x = 1.5$ and the wave bounces and reflects back through the domain and, over time, the interference of the traveling and reflected waves results in noise dominating the dynamics of the ballistic case. Note that the oscillatory behavior of the

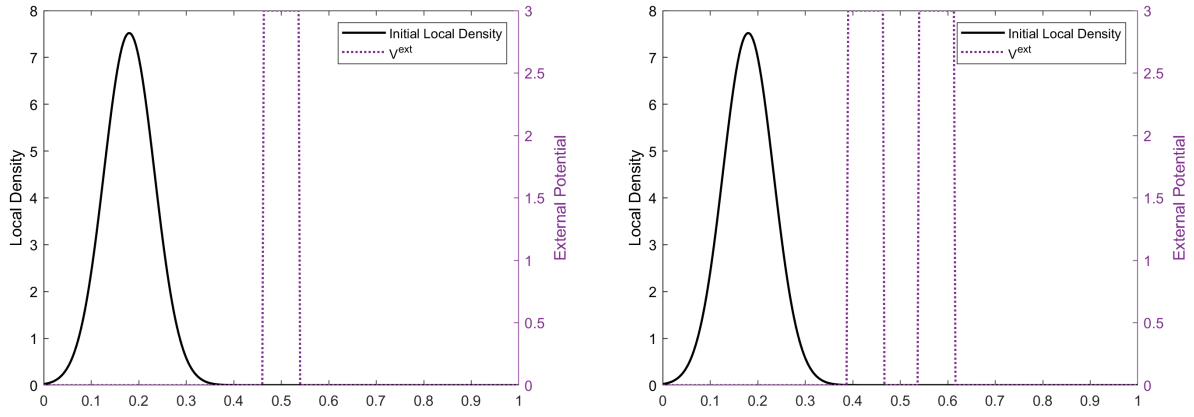

(a) Single potential barrier and initial local density. **(b)** Double potential barrier and initial local density

Figure 5.6: The initial density with the single potential barrier and the double potential barriers used in the numerical study.

ballistic Liouville equation is in part due to the choice of Neumann boundary conditions and can be mitigated through the choice of open or transparent boundary conditions. However, recall that Neumann boundary conditions are chosen as they guarantee the local density is positive for all time which is an important assumption in the convergence result for the QLE given in Theorem 4.2. In the QLE case, the wavefront is still transported to the right through the domain and exhibits reflection off the right boundary of the domain. However, after about $t \approx \varepsilon$ time has elapsed the effects of collision begin to appear in the dynamics. By definition, the collision operator relaxes ϱ towards the equilibrium and, over long times the collision phenomena drive the QLE dynamics to the global equilibrium. For $\varepsilon = 0.1$ the dynamics of the ballistic model are dominated by noise by $t = 0.2$, which is why Figure 5.8 only shows the local density comparison up to time $t = 0.15$. On the other hand, with the QDD model, the Gaussian wave packet initial density widens throughout the domain as the solution exponentially approaches the global equilibrium [60]. However, in the long-time limit of the QLE and QDD, we see that the both of the models are approaching the same global equilibrium, which is to be expected.

In the case of a single potential barrier, we largely see similar themes in the differences of the three electron transport models: QDD quickly approaches global equilibrium, the ballistic model is eventually dominated by noise from the interference of transported and reflected waves, and

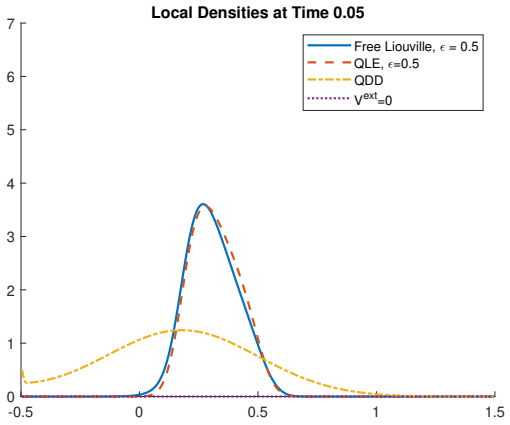

(a) Local density comparison $\epsilon = 0.5$ at time 0.05

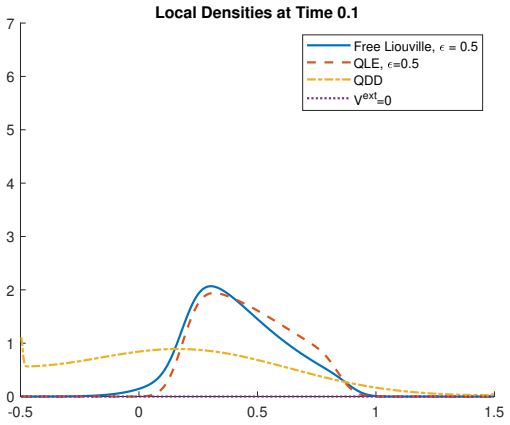

(b) Local density comparison $\epsilon = 0.5$ at time 0.1

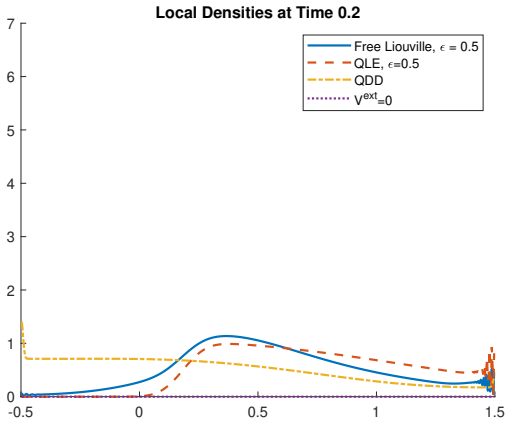

(c) Local density comparison $\epsilon = 0.5$ at time 0.2

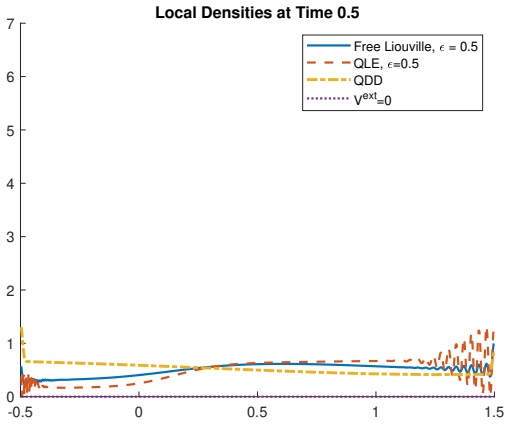

(d) Local density comparison $\epsilon = 0.5$ at time 0.5

Figure 5.7: A comparison of the local densities of QLE, free Liouville, and QDD over time in free space, $V^{\text{ext}} = 0$, when $\varepsilon = 0.5$.

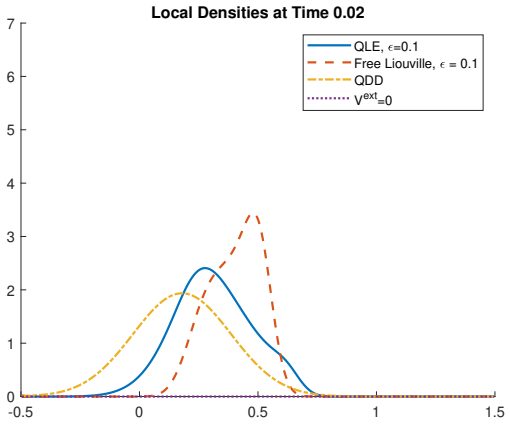

(a) Local density comparison $\epsilon = 0.1$ at time 0.02

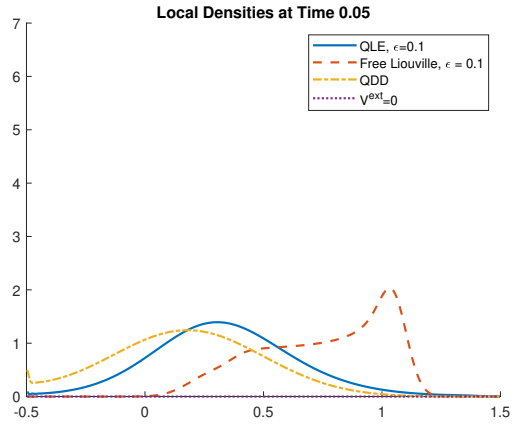

(b) Local density comparison $\epsilon = 0.1$ at time 0.05

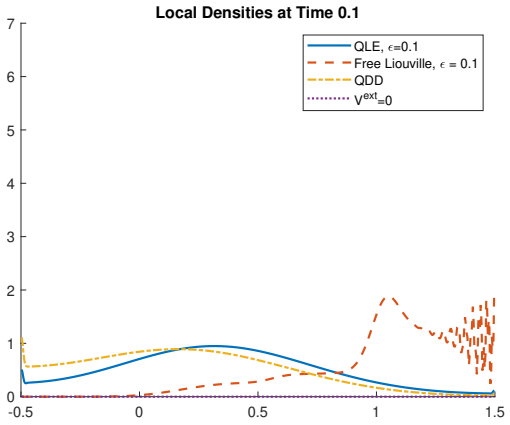

(c) Local density comparison $\epsilon = 0.1$ at time 0.1

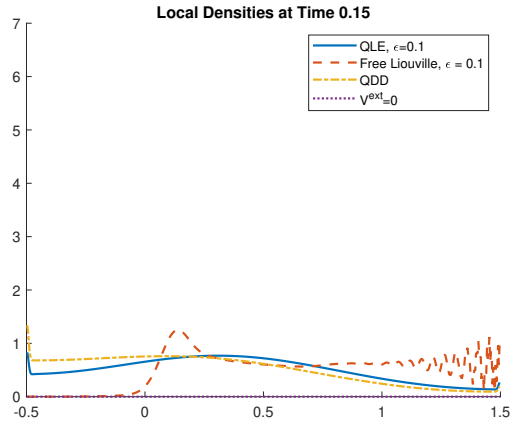

(d) Local density comparison $\epsilon = 0.1$ at time 0.15

Figure 5.8: A comparison of the local densities of QLE, free Liouville, and QDD over time in free space, $V^{\text{ext}} = 0$, when $\varepsilon = 0.1$.

the QLE exhibits transport dynamics for early times and eventually approaches global equilibrium. However, in the presence of a potential barrier we now observe the phenomena of *quantum tunneling*. Figures 5.9 and 5.10 show the local density for each model at different times as the wavepacket interacts with a single potential barrier. In both the QLE and ballistic QLE cases, the wavefront hits the potential barrier and only the particles that have an energy sufficiently close to the resonant energies of the barrier can tunnel through to the other side. The particles that do not tunnel through the potential barrier are reflected off of the barrier and travel back towards $x = 0$, while the particles that penetrate form a wavefront that continues to travel towards $x = 1.5$. In the ballistic case, the wavefront that penetrated the potential barrier is reflected at $x = 1.5$. On the other hand, the particles that did not penetrate the barrier continue to reflect between the barrier and the boundary at $x = -0.5$, which results in the dynamics being dominated by noise for times greater than $t \approx \varepsilon$. In the case of the QLE, after the wavefront initially hits the potential barrier the reflected wave off the barrier is smaller compared to the ballistic case and it is diminished as the collision effects take hold. Particles continue to penetrate the barrier via collision effects after about $t \approx \varepsilon$ time has elapsed and the reflected wavefronts are dampened due to the relaxation towards the local equilibrium. In the case of the QDD, the initial local density broadens until the particles reach the potential barrier and the effects of collision allow for particles to penetrate the barrier. The QDD dynamics do not exhibit any reflections of the wave off the boundaries or the potential barrier, only penetration of the barrier via collisions. Notably, the transport effects in the QLE and ballistic model allow a greater amount of particles to penetrate the potential barrier at an earlier time when compared to the QDD dynamics. Again, as in the free-space case, in the long time limit the QLE-BGK local density begins to approach the global equilibrium.

The double barrier case exhibits much of the same observations seen in the single potential barrier case. In particular: the ballistic model is eventually dominated by interference of the wavefront reflecting off the potential barriers and the boundaries, the QDD approaches global equilibrium without any wave interference, and the QLE shows penetration of the barrier via both transport and collision phenomena. However, in the double barrier case, the presence of the quantum po-

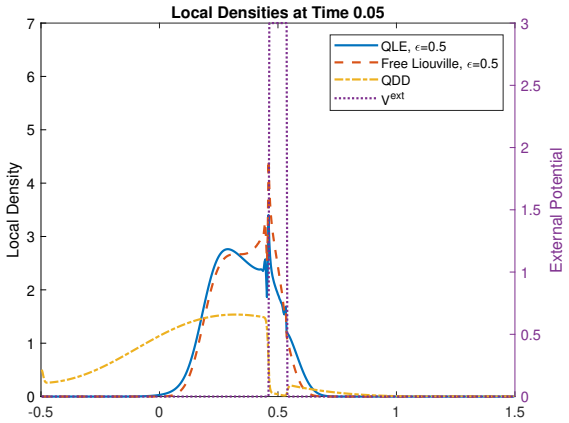

(a) Local density comparison $\epsilon = 0.5$ at time 0.05

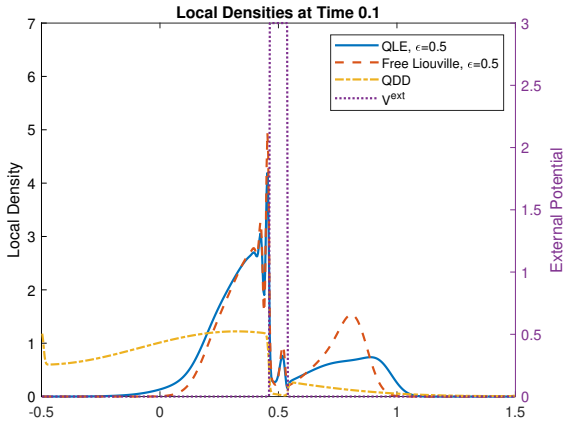

(b) Local density comparison $\epsilon = 0.5$ at time 0.1

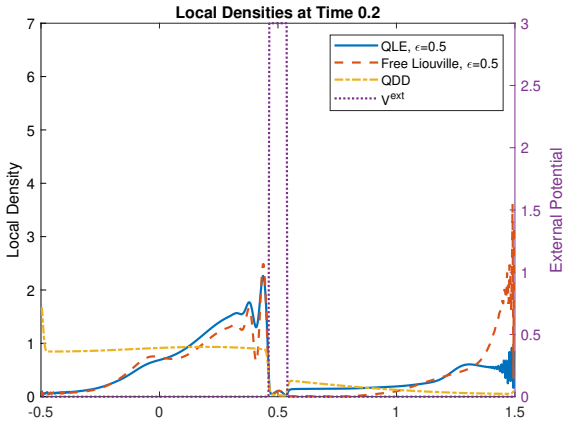

(c) Local density comparison $\epsilon = 0.5$ at time 0.2

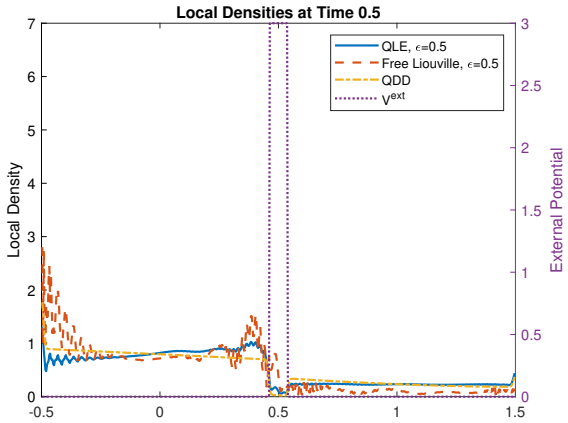

(d) Local density comparison $\epsilon = 0.5$ at time 0.5

Figure 5.9: A comparison of the local densities of QLE, free Liouville, and QDD over time in the presence of a single potential barrier when $\varepsilon = 0.5$.

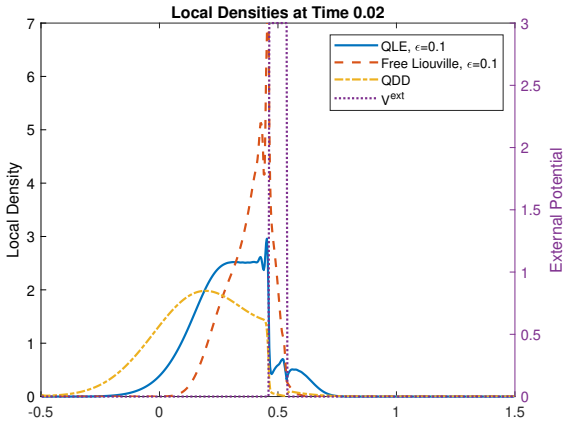

(a) Local density comparison $\epsilon = 0.1$ at time 0.02

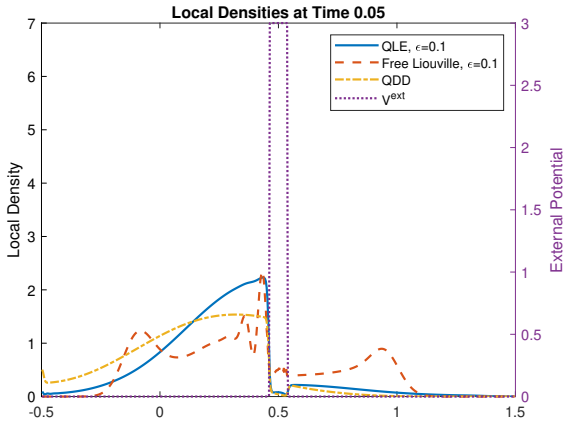

(b) Local density comparison $\epsilon = 0.1$ at time 0.05

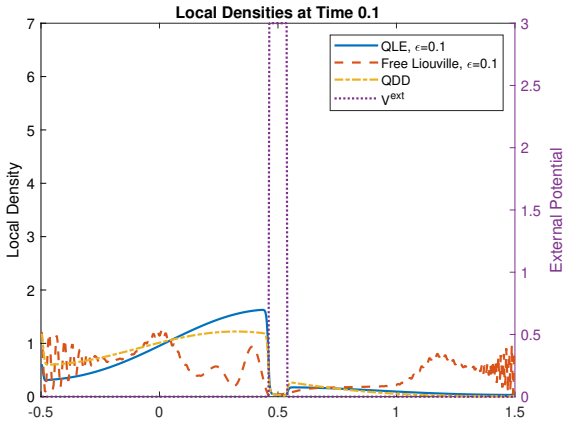

(c) Local density comparison $\epsilon = 0.1$ at time 0.1

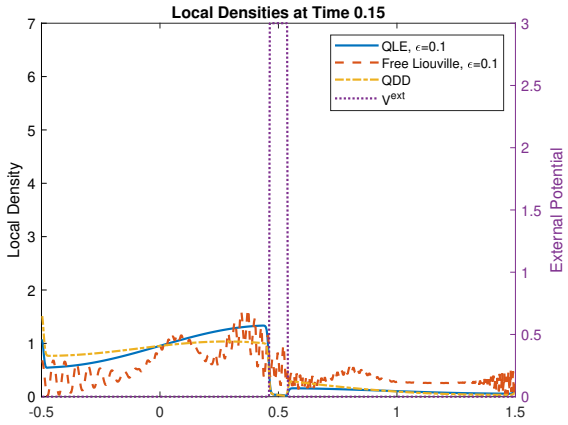

(d) Local density comparison $\epsilon = 0.1$ at time 0.15

Figure 5.10: A comparison of the local densities of QLE, free Liouville, and QDD over time in the presence of a single potential barrier when $\varepsilon = 0.1$.

tential well between the barriers creates some differences in the dynamics observed. In the QLE and the ballistic case after the wavefront has passed through both potential barriers (at $t \approx \varepsilon/2$) there is a larger quantity of particles on the right side of the barriers when compared to QDD, see Figures 5.11 and 5.12. Alternately, we see for both QLE and QDD that particles begin to accumulate in the potential well while the collision process continues to allow particles to penetrate both barriers and occupy the region to the right of the barriers. While in the ballistic case, the particles in the well eventually penetrate back through the left barrier or out through the right barrier and the wavefront continues to reflect off the boundaries and the barriers.

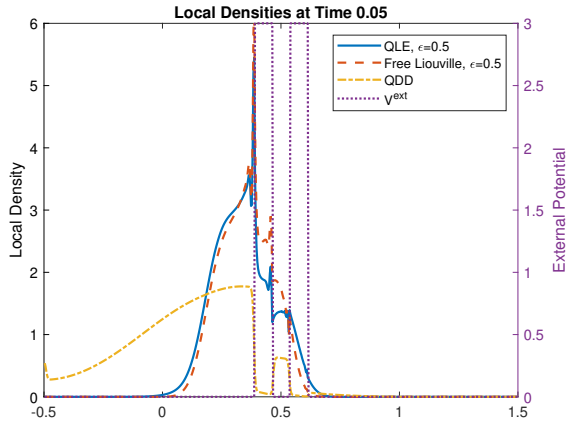

(a) Local density comparison $\epsilon = 0.5$ at time 0.05

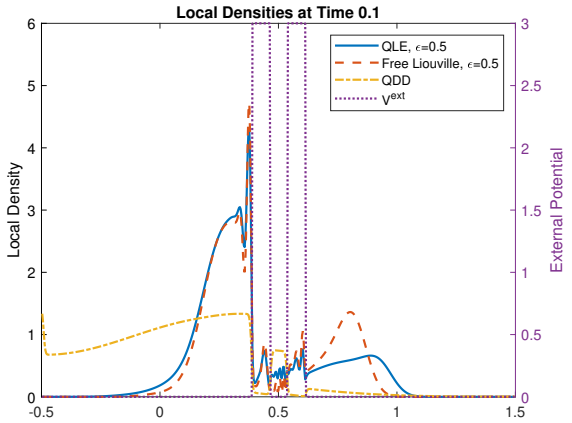

(b) Local density comparison $\epsilon = 0.5$ at time 0.1

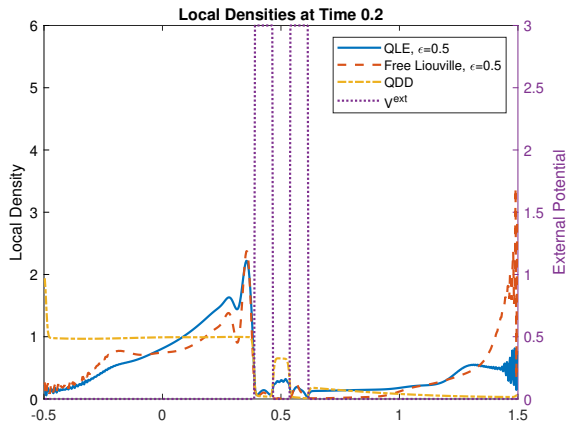

(c) Local density comparison $\epsilon = 0.5$ at time 0.2

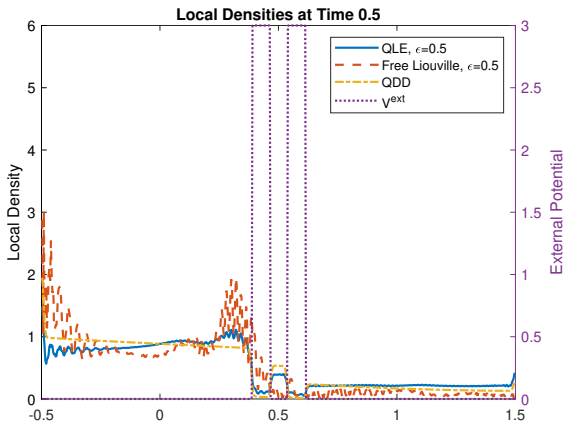

(d) Local density comparison $\epsilon = 0.5$ at time 0.5

Figure 5.11: A comparison of the local densities of QLE, free Liouville, and QDD over time in the presence of a double potential barrier when $\varepsilon = 0.5$.

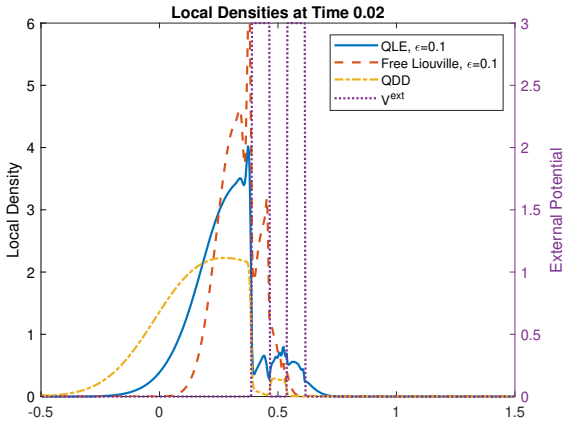

(a) Local density comparison $\epsilon = 0.1$ at time 0.02

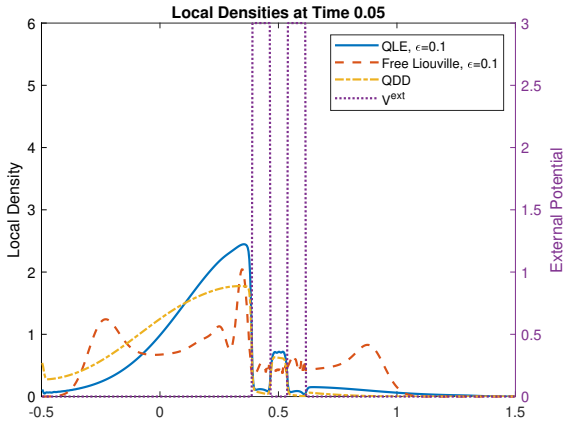

(b) Local density comparison $\epsilon = 0.1$ at time 0.05

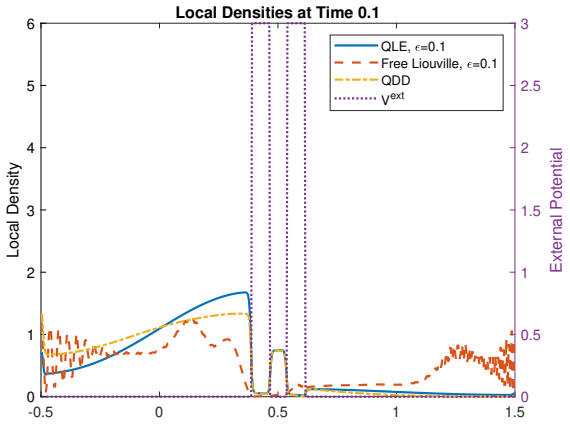

(c) Local density comparison $\epsilon = 0.1$ at time 0.1

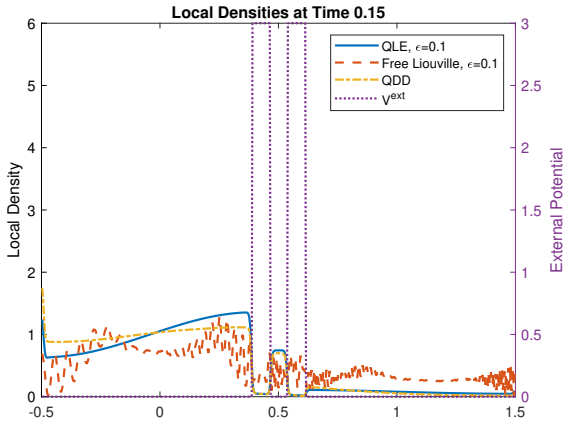

(d) Local density comparison $\epsilon = 0.1$ at time 0.15

Figure 5.12: A comparison of the local densities of QLE, free Liouville, and QDD over time in the presence of a double potential barrier when $\varepsilon = 0.1$.

Lastly, we compare the global equilibrium between the QLE for $\varepsilon = 0.1$ and the QDD in the free-space case. Figure 5.13(a) shows a comparison between the local density of the QLE and the QDD. The relative error between the local densities measured in the discrete L^1-norm is 0.0134. Figure 5.13(b) shows a comparison between the chemical potential of the QLE and QDD where the relative error measured in discrete L^1-norm is 0.009. Recall, the QLE chemical potential is the minimizer of the functional $J(A)$ (5.2) while the QDD chemical potential is obtained from minimizing $G(A, V)$ (5.23). Thus, as $t \to \infty$, the solution of the QLE, $\varrho = \sum_p \rho_p \left|\psi_p\right\rangle \left\langle\psi_p\right| \approx e^{-(H_0+A)}$ because the density matrix associated with the QDD solution is a quantum Maxwellian for all time. Figure 5.13(c) shows the first five modes of the QLE solution with the first four modes of the QDD solution at time 0.6. The relative error between the first four modes is 0.0029, 0.0150, 0.0856, and 0.1816, respectively. Recall, the QDD model can be derived from the QLE via a diffusive limit (Section 5.2.1) and, thus, it is expected that the QLE solution begins to approach the QDD solution for large times.

In summary, we have seen that for short times $t < \varepsilon$ the QLE dynamics closely resemble the dynamics of the ballistic case. And beginning around $t \approx \varepsilon$ we see the scattering begins to drive the QLE dynamics towards the global equilibrium. The ballistic case exhibits quantum tunneling at earlier times but the wavefront is eventually dominated by noise due to the interference of the reflecting waves. In the pure-transport model the particles continue to be transmitted through the potential barriers and eventually the particles within the barriers is negligible. Notably, in the double barrier case, the effects of collision allow for particles to accumulate within the potential well, as seen in both QLE and QDD. The quantum drift-diffusion model quickly approaches the global equilibrium and in the long-time limit the QLE solution converges to the QDD solution.

The collisional models are more favorable in this numerical set-up to model the dynamics of RTDs. This is because a desirable feature of RTDs is the accumulation of particles in the well, which is exhibited in both the QLE and QDD local densities [59, 61]. Ballistic transport assumes that the mean-free-path of the electron is large compared to the length of the device. However, with the small-scale of quantum semiconductor devices the effects of scattering and collisions cannot be

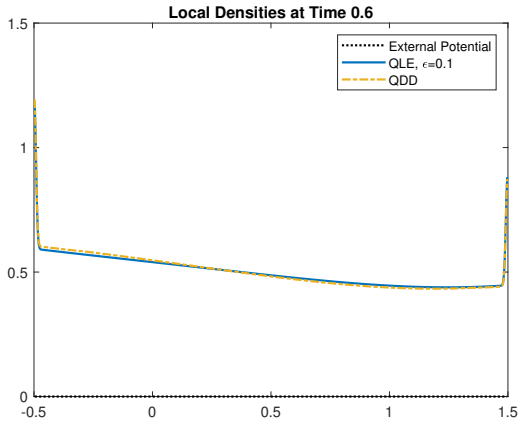

(a) Local density comparison $\epsilon = 0.1$ at time 0.6

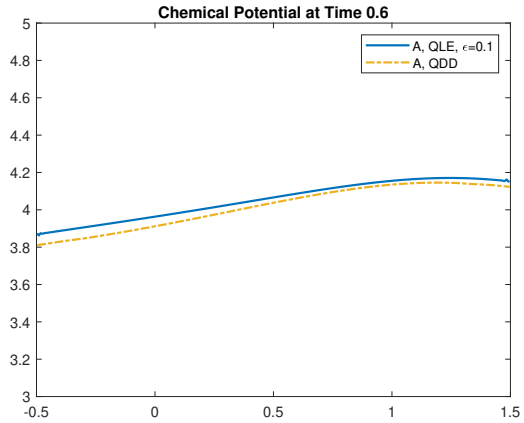

(b) Chemical potential comparison at time 0.6

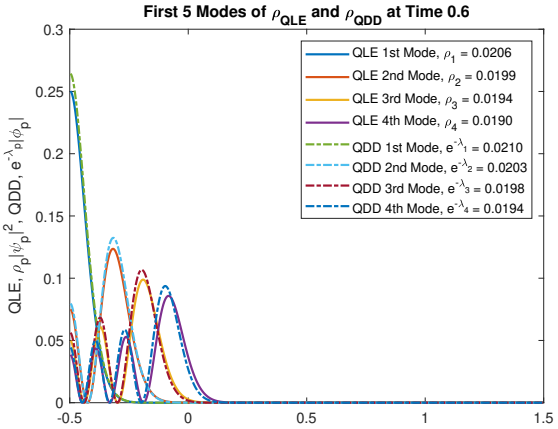

(c) A comparison of the first 5 modes of the solution to QLE ϱ and the solution to QDD at time 0.6

Figure 5.13: The QLE and QDD solutions agree in the long-time limit as the global equilibrium is approached by each model. This is shown by comparing the local densities in (a), the chemical potentials in (b), and the first four modes of the respective solutions in (c).

neglected [36, 61]. Thus, the quantum Liouville-BGK equation is a better description for electron transport, compared to the ballistic Liouville, in small devices as collisions form an important part of the dynamics. Compared to the quantum drift-diffusion model, the solutions to the quantum Liouville equation capture both the transport and scattering of particles which is present in short-time scales in these quantum devices. On the other hand, if the steady-state or global equilibrium dynamics are of concern then the QDD is the better model as it converges quickly to the global equilibrium.

5.4 Conclusion

This project introduced and analyzed a numerical scheme for the quantum Liouville-BGK equation. The numerical resolution of the QLE is a nontrivial task due the presence of the nonlinear equilibrium operator in the collision operator. However, we showed that through the use of a splitting scheme in which we treat the two physical phenomena separately the difficulty with the nonlinear equilibrium operator can be circumvented. The collision subproblem of the splitting scheme is based on the minimization of the free energy under a local density constraint to obtain the equilibrium operator. While the transport subproblem of the splitting scheme employed the use of a secondary splitting scheme to handle the nonlinearity present in the Poisson potential term. In Chapter 4, we proved the splitting scheme for the QLE is well defined and convergent, yielding a unique numerical solution. Numerically, we have shown the Strang splitting scheme is indeed second-order in time. The convergence result in Theorem 4.5 only gives $o(h)$ convergence, which is due to the fact the mapping $\varrho \mapsto \varrho_{\mathrm{e}}[\varrho]$ is Hölder continuous and not Lipshitz continuous. Thus we consider the convergence result in Theorem 4.5 to be non-optimal. As a consequence of the fact the splitting scheme is convergent compared to the exact solution of the QLE, we were able to show the continuous solution is unique, as well. We concluded with a numerical study of the effect of the collision process on electron transport. We compared three models representing three different collision regimes: ballistic quantum Liouville equation, the quantum Liouville-BGK equation, and the quantum drift-diffusion model. We found that the effects of ballistic transport increase

the transmission of particles through potential barriers at earlier times compared to the quantum drift-diffusion model, which is collision dominated. The ballistic transport of particles creates interference between the wavefront as particles continue to reflect off the boundaries and the potential barriers. Theoretically, the QLE should approach the solution to the QDD in the long-time limit since the QDD can be derived via a diffusive limit of the QLE. We have confirmed numerically in free-space propagation that the QLE does indeed approach the QDD solution after $t >> \varepsilon$. In particular, we have seen that in the long-time limit the solution to the QLE $\varrho(t)$ is approximately a quantum Maxwellian, $\varrho(t) \approx \exp(-(H_0 + A))$ where A can be approximated by the quantum drift-diffusion solution. A future direction for this work would be to implement an asymptotic preserving scheme to ensure the scheme is still convergent and well-defined in the limit as ε approaches zero.

Chapter 6

Conclusion

This dissertation introduced two projects connected with a common theme of wave propagation. In the first portion, a new approximation method for laser propagation in the atmosphere called the variational scaling law was introduced. The variational scaling law approximates the solution to the stochastic paraxial Helmholtz equation, which is a partial differential equation model that is commonly used to model atmospheric propagation of a laser beam. The variational scaling law assumes the laser beam maintains a Gaussian form yet we have shown that this method well-approximates the beam propagation compared to the paraxial Helmholtz equation.

In the second portion, a numerical scheme for the quantum Liouville-BGK equation is presented. The quantum Liouville-BGK equation is nonlinear due to the inclusion scattering or collisions in the model using the BGK-collision operator and the electrostatic potential by coupling with the Poisson equation. The numerical scheme for the QLE is based on a Strang splitting scheme which allows us to separate the two physical phenomena of transport and collisions of particles. By doing so, we are able to greatly simplify the resolution of the QLE since we can locally treat the collision operator and Poisson potential as linear within the respective subproblems. In the semi-discrete setting, we showed the numerical scheme is well-defined and convergent. As an application of the numerical scheme, we numerically studied the effects of different collision regimes on electron transport.

Bibliography

[1] P. Degond and C. Ringhofer. Quantum moment hydrodynamics and the entropy principle. *Journal of Statistical Physics*, 112(3):587,628, 2003-08.

[2] S.P. Bragdon, D. Cargill, and J. Grosek. Variational scaling law for atmospheric propagation. *submitted*.

[3] S.P. Bragdon, D. Cargill, and J. Grosek. Lagrangian scaling law for atmospheric propagation. In *Optical Sensors and Sensing Congress*, page PM2D.4. Optical Society of America, 2020.

[4] L. C. Andrews and R. L. Phillips. *Laser Beam Propagation Through Random Media*, volume 152. SPIE Press, Bellingham, WA, 2005.

[5] G. Perram, M. Marciniak, and M. Goda. High-enery laser weapons: technology overview. In *Laser Technologies for Defense and Security*. International Society for Optics and Photonics.

[6] J. W. Goodman. *Coherence of optical waves. Statistical Optics*, pages 157–236, 1985.

[7] U. Frisch. *Turbulence: The legacy of A. N. Kolmogorov*. Cambridge University Press, 1995.

[8] F. Wang, X. Liu, and Y. Cai. *Propagation of partially coherent beam in turbulent atmosphere: a review. Progress in Electromagnetics Research*, 150:123–143, 2015.

[9] J. Isaacs and P. Spangle. *The effect of laser noise on the propagation of laser radiation in dispersive and nonlinear media.* In *Laser Communication and Propagation through the Atmosphere and Oceans VII*, volume 10770, page 107700B. International Society for Optics and Photonics, 2018.

[10] R. Noriega-Manez and J. Gutierrez-Vega. *Rytov theory for Helmholtz-Gauss beams in turbulent atmosphere. Optics Express*, 15(25):16328–16341, 2007.

[11] H. T. Yura. *Atmospheric turbulence induced laser beam spread. Applied Optics*, 10(12), 1971.

[12] M. Whiteley and E. Magee. *Scaling for High Energy Laser and Relay Engagement (SHaRE) A toolbox for Propagation and Beam Control Effects Modeling User's Guide Version 2010a.957.* Technical report, MZA Associates Corporation, 2010. Not publicly released.

[13] V. Kitsios, J. Frederiksen, and M. Zidikheri. *Subgrid model with scaling laws for atmospheric simulations. Journal of the Atmospheric Sciences*, 69(4), 2012.

[14] N. Van Zandt, S. Fiorino, and K. Keefer. *Enhanced, fast-running scaling law model of thermal blooming and turbulence effects on high energy laser propagation. Optics Express*, 21(12):14789–14798, 2013.

[15] S. Shakir, T. Dolash, M. Spencer, R. Berdine, D. Cargill, and R. Carreras. *General wave optics propagation scaling law. JOSA A*, 33(12):2477–2484, 2016.

[16] C. Fox. *An Introduction to the Calculus of Variations*. Dover Publications Inc., New York, 1987.

[17] S. Nagaraj, J. Grosek, S. Petrides, L. Demkowicz, and J. Mora. *A 3D DPG Maxwell Approach to Nonlinear Raman Gain in Fiber Laser Amplifiers. Journal of Computational Physics: X*, 2:100002, 2019.

[18] A. Ishimaru. *Wave Propagation and Scattering in Random Media*. Academic Press, 1977.

[19] B. Nair and B.S. White. High-frequency wave propagation in random media– a unified approach. *SIAM J. Appl. Math.*, 51(2):374–411, 1991.

[20] F. Bailly, J.F. Clouet, and J.P. Fouque. Parabolic and gaussian white noise approximation for wave propagation in random media. *SIAM J. of Appl. Math.*, 56(5):1445–1470, 1996.

[21] J.P. Fouque, J. Garnier, G. Papanicolaou, and K. Sølna. *Wave Propagation and Time Reversal in Randomly Layered Media*, volume 56 of *Stochastic Modelling and Applied Probability*. Springer New York, 2007.

[22] V.I. Tatarski. *Wave Propagation in a Turbulent Medium*. Dover, 1961.

[23] L. C. Andrews, M. A. Al-Habash, C. Y. Hopen, and R. L. Phillips. *Theory of optical scintillation: Gaussian-beam wave model. Waves in Random Media*, 11(3):271–291, 2001.

[24] A. Hemming, N. Simakov, J. Haub, and A. Carter. *A review of recent progress in holmium-doped silica fibre sources. Optical Fiber Technology*, 20(6):621–630, 2014.

[25] D. Sliney and M. Wolbarsht. *Safety with Lasers and Other Optical Sources*, chapter 13: Atmospheric Propagation of Laser Beams. Springer, 1980.

[26] D. Anderson. *Variational approach to nonlinear pulse propagation in optical fibers. Physical review A*, 27(6):3135, 1983.

[27] D. Anderson, M. Lisak, and T. Reichel. *Approximate analytical approaches to nonlinear pulse propagation in optical fibers: A comparison. Physical Review A*, 38(3):1618, 1988.

[28] D. Anderson and M. Lisak. *A variational approach to the nonlinear Schrödinger equation. Physica Scripta*, 1996(T63):69, 1996.

[29] D. Anderson and M. Bonnedal. Variational approach to nonlinear self-focusing of gaussian laser beams. *Physics of Fluids*, 22(1):105–109, 1979.

[30] G. Pichot. Algorithms for gaussian random field generation. *Technical Report*, 2017.

[31] G. Strang. *On the Construction and Comparison of Difference Schemes. SIAM Journal of Numerical Analysis*, 5(3):506–517, 1968.

[32] S. MacNamara and G. Strang. *Operator Splitting*. In R. Glowinski, S.J. Stanley, and W. Yin, editors, *Splitting Methods in Communications, Imaging, Science, and Engineering*. Springer International Publishing, 2016.

[33] M. Roggemann, B. Welsh, D. Montera, and T. Rhoadarmer. Method for simulating atmospheric turbulence phase effects for multiple time slices and anisoplanatic conditions. *OSA Applied Optics*, 34(20):4037–4051, 1991.

[34] J.D. Schmidt. *Numerical Simulation of Optical Wave Propagation.* SPIE, 2010.

[35] L.L. Chang, L. Esaki, and R. Tsu. Resonant tunneling in semiconductor double barriers. *Applied Physics Letters*, 24:593–595, 1974.

[36] C. Jacoboni. *Theory of Electron Transport in Semiconductors: A Pathway from Elementary Physics to Nonequilibrium Green Functions*. Springer, 2010.

[37] A. Jüngel and D. Matthes. A derivation of the isothermal quantum hydrodynamic equations using entropy minimization. *ZAMM - Journal of Applied Mathematics and Mechanics / Zeitschrift für Angewandte Mathematik und Mechanik*, 85(11):806,814, 2005-11-02.

[38] Ansgar Jungel, Daniel Matthes, and Josipa Pina Milis Ic. Derivation of new quantum hydrodynamic equations using entropy minimization. *SIAM Journal on Applied Mathematics*, 67(1):46–68, 2006.

[39] A. Jüngel. *Quasi-hydrodynamic semiconductor equations*. Progress in Nonlinear Differential Equations and their Applications. Birkhäuser Verlag, 2001.

[40] P. Degond, S. Gallego, and F. Mehats. On quantum hydrodynamic and quantum energy transport models. *Commun. Math. Sci.*, 5(4):887–908, 2007.

[41] C. Levermore. Moment closure hierarchies for kinetic theories. *Journal of Statistical Physics*, 83(5-6):1021,1065, 1996-06.

[42] P. L. Bhatnagar, E. P. Gross, and M. Krook. A model for collision processes in gases. i. small amplitude processes in charged and neutral one-component systems. *Physical Review*, 94(3):511–525, 1954-05.

[43] P. Degond, S. Gallego, F. Méhats, and C. Ringhofer. Quantum hydrodynamic and diffusion models derived from the entropy principle. In *Quantum Transport*. Springer, 2008.

[44] P. Degond, S. Gallego, and F. Méhats. An entropic quantum drift-diffusion model for electron transport in resonant tunneling diodes. *Journal of Computational Physics*, 221(1):226–249, 2007.

[45] S.P. Bragdon and O. Pinaud. A splitting scheme for the quantum liouville-BGK equation. *submitted*.

[46] S Gallego and F Méhats. Entropic discretization of a quantum drift-diffusion model. *SIAM Journal on Numerical Analysis*, 43(5):1828–1849, 2005.

[47] O. Pinaud. Transient simulations of a resonant tunneling diode. *Journal of Applied Physics*, 92(4):1987–1994, 2002.

[48] A. Arnold. Numerical absorbing boundary conditions for quantum evolution. *VLSI Design*, (6):313–328, 1998.

[49] F. Méhats and O. Pinaud. An inverse problem in quantum statistical physics. *Journal of Statistical Physics*, 140(3):565–602, 2010.

[50] F. Méhats and O. Pinaud. The quantum Liouville–BGK equation and the moment problem. *Journal of Differential Equations*, 263(7):3737–3787, 2017.

[51] M. Reed and B. Simon. *Methods of Modern Mathematical Physics Vol 1: Functional Analysis*. Academic Press, 1972.

[52] P. Degond, S. Gallego, and F. Mehats. Isothermal quantum hydrodynamics: Derivation, asymptotic analysis, and simulation. *Multiscale Modeling and Simulation*, 6(1):246–272, 2007.

[53] P. Degond, F. Méhats, and C. Ringhofer. Quantum energy-transport and drift-diffusion models. *Journal of Statistical Physics*, 118(3-4):625–667, 2005.

[54] B. Besse, C. Bidégaray and S. Descombes. Order estimates in time of splitting methods for the nonlinear Schrödinger equation. *SIAM Journal of Numerical Analysis*, 40(1):26–40, 2002.

[55] C. Lubich. On splitting methods for Schrödinger-poisson and cubic nonlinear Schrödinger equations. *Mathematics of Computation*, 77(264):2141–2153, 2008.

[56] I. Bihari. A generalization of a lemma of Bellman and its application to uniqueness problems of differential equations. *Acta Math. Acad. Sci. Hungarica*, 7:81–94, 1956.

[57] S. Gallego. Étude théorique et numérique du modèle de dérive-diffusion quantique. *rapport de stage de DEA*, 2004.

[58] O. Pinaud. The quantum drift-diffusion model: existence and exponential convergence to the equilibrium. *Annales de l'Institut Henri Poincaré C, Analyse non linéaire*, 36(3):811–836, 2019.

[59] N.C. Kluksdahl, A.M. Kriman, D.K Ferry, and C. Ringhofer. Self-consistent study of the resonant tunneling diode. *Physical Review B*, 39(11), 1989.

[60] O. Pinaud. The quantum drift-diffusion model: Existence and exponential convergence to the equilibrium. *Annales de l'Institut Henri Poincaré / Analyse non linéaire*, 36(3):811,836, 2019-05.

[61] B. Ricco and M. Ya. Azbel. Physics of resonant tunneling. the one-dimensional double-barrier case. *Physical Review B*, 29(4), 1984.